DEVELOPMENT AND APPLICATIONS OF NANOSCALE SCANNING ELECTROCHEMICAL MICROSCOPY

by

Jiyeon Kim

BS, Ewha Womans University, 1999

MS, Ewha Womans University, 2001

Submitted to the Graduate Faculty of

the Kenneth P. Dietrich school of Arts and Sciences in partial fulfillment

of the requirements for the degree of

Doctor of Philosophy

University of Pittsburgh

2012

UNIVERSITY OF PITTSBURGH

DIETRICH SCHOOL OF ARTS AND SCIENCES

This dissertation was presented

by

Jiyeon Kim

It was defended on

Nov 15, 2012

and approved by

Stephen G. Weber, Professor, Department of Chemistry

Adrian C. Michael, Professor, Department of Chemistry

Minhee Yun, Associate Professor, Department of Electrical & Computer Engineering

Dissertation Advisor: Shigeru Amemiya, Associate Professor, Department of Chemistry

DEVELOPEMENT AND APPLICATIONS OF NANOSCALE SCANNING ELECTROCHEMICAL MICROSCOPY

Jiyeon Kim, PhD

University of Pittsburgh, 2012

After more than 20 years of basic nanoscience research, advances in nanotechnology have opened up unprecedented possibilities and opportunities in electrochemistry. Especially, fabrication, characterization, modification and the understanding of various electrochemical interfaces or electrochemical processes at the nanoscale have led to applications of electrochemical methods to novel technologies. Nanoscale characterization and theoretical analysis of electrochemical interfaces and reactions can lead to the understanding of these complicated chemical systems at the molecular level. This is not only scientifically interesting, but also crucial for the controlled applications of electrochemistry in nanotechnology.

A theme of my PhD work is to seek the better understanding of important nanosystems such as single walled carbon nanotube (SWNT) and nanopores in biological as well as artificial nanoporous membrane. The understanding of the electrochemistry of carbon nanotubes as an attractive electrode material for electroanalysis and electrocatalysis is fundamentally and practically important. Also, the greater understanding of nucleocytoplasmic transport through the nuclear pores in nuclear envelope is highly significant because of its critical roles as a regulator of gene expression, a gateway for gene delivery, and a model of biomimetic transport systems. In addition, the quantitative understanding of membrane permeability at a single nanopore level is a prerequisite for the development and the application of nanoporous membrane for nanofiltration, biomedical devices, nano fluidics, and biomimetic membrane transport. To achieve these goals, I

developed scanning electrochemical microscopy (SECM) as a powerful nanoscale tool and applied this technology to the kinetic study and high-resolution imaging of heterogeneous reactions at various interfaces. Therefore, this thesis is based on two sections. In the first section, I summarize the application of nanoscale SECM to the study of a few different nanostructures and the substantial findings. The second section is concerned about the development of nanoscale SECM. Based on these achievements, the capacity of nanoscale SECM will be greatly increased to characterize and understand various nanomaterials and interfaces at the nanoscale.

Table of Contents

List of Tables

List of Figures

List of Schemes

ACKNOWLEDGEMENTS

First of all, I would like to express my sincere gratitude to Professor Shigeru Amemiya for his guidance, support and encouragement throughout my graduate research. I have been deeply inspired by his knowledge and enthusiasm toward scientific research and education. I believe that the experience in his group will be invaluable in my career as a professional scientist.

I would like to thank Professors Stephen Weber, Adrian Michael and Minhee Yun for serving on my committee and for their advice towards my education.

I want to thank Dr. Eunkyoung Kim for helpful discussions, support, and his invaluable friendship. I would also like to acknowledge all current and former members of Amemiya group for their supports: Benjamin Kabagambe, Hui Xiong, Nikoloz Nioradze, Patrick Rodgers, Ran Chen, Yushin Kim, Dr. Anahita Izadyar, Dr. Jing Ping, Dr. Mei Shen, Dr. Padmanabhan Santhosh, and Dr. Ryoichi Ishimatsu.

Also, I want to thank the following groups and individuals for their help with different instruments and samples for my research: Mr. Tom Gasmire and Mr. Jeff Sicher (Machine shop), Kong group at MIT (samples of carbon nanotube), Mr. Albert Stewart (SEM), Asher group (Raman microscopy) and Mr. Mike Mcdonald (NFCF).

Lastly, I would like to thank my family and Arong for their trust and the endless love.

1. Introduction

A theme of my PhD work is to seek the better understanding of important nanosystems such as single walled carbon nanotube (SWNT) and nanopores in biological as well as artificial nanoporous membrane. The understanding of the electrochemistry of carbon nanotubes as an attractive electrode material for electroanalysis and electrocatalysis is fundamentally and practically important. Also, the greater understanding of nucleocytoplasmic transport through the nuclear pores in nuclear envelope is highly significant because of its critical roles as a regulator of gene expression, a gateway for gene delivery, and a model of biomimetic transport systems. In addition, the quantitative understanding of membrane permeability at a single nanopore level is a prerequisite for the development and the application of nanoporous membrane for nanofiltration, biomedical devices, nano fluidics, and biomimetic membrane transport. To achieve these goals, I developed scanning electrochemical microscopy (SECM) as a powerful nanoscale tool and applied this technology to the kinetic study and high-resolution imaging of heterogeneous reactions at various interfaces. Therefore, this thesis is based on two sections. In the first section, I summarize the application of nanoscale SECM to the study of a few different nanostructures and the substantial findings. The second section is concerned about the development of nanoscale SECM.

In the first section, I will discuss the nanoscale SECM study of nanopores including the biological as well as the artificial nanoporous membrane and the single walled carbon nanotubes (SWNT). In Chapter 2, nanopores at the intact nuclear envelope (NE) are studied by nanogap based SECM, which allows for the quantitative measurement of the high permeability and the corresponding nanodimensions of transport routes in NE. The reliable and accurate measurement

of high permeability is attributed to the stable nanogap between nanofabricated SECM tip and the stabilized nuclear envelope by nanofabricated immobilization, which provides a deeper understanding of the molecular transport pathway in NE. In Chapter 3, SWNTs are detected by screening the electrochemical reactivity of individual nanotubes by SECM. In this project, I discovered that the sidewall of SWNT is highly active for electron transfer. Chapter 4 highlights the high resolution and quantitative SECM imaging of ion transport at the single nanopores using nanopipet tips under the isothermal conditions.

In the second section, I invented or introduced several key technologies to develop nanoscale SECM. Nanoscale SECM is featured by a nanometer-sized tip, a nanogap between the tip and the substrate, and a nanostructured substrate. Nanometer sized tips are advantageous for the various SECM application such as the fast kinetic measurement, high spatial resolution imaging and the study of biological systems owing to the highly enhanced mass transfer rate, small dimension, and negligible effect of charging current and resistive potential drop in solution due to the small current level, respectively. To achieve nanometer sized tips as a probe for SECM, I introduced focused ion beam (FIB) milling. The utilization of FIB milling provides well characterized tips showing the consistent electrochemical behavior with its scanning electron microscopic image. Such tips have not only the small size but also closer approach capability up to nanometer distance from the substrate, thus it can be applicable to the accurate and quantitative analysis for the fast kinetic study in SECM as well as the high spatial resolution imaging. In fact, these tips were used for high spatial resolution imaging and the fast kinetic measurement by several members of our group. The outcomes of these collaborative projects published in 5 papers,[2,5,6,7,9] which are not included in this thesis (see References). Further, we plan to commercialize the FIB milled tips for its wide application, thus we envision that our

reliable and reproducible tip fabrication by FIB milling will be sustainable with broad impacts in the various study field.

In addition, I invented an isothermal condition to obtain a stable nanogap between a tip and a substrate surface (Chapter 5). An isothermal condition is constructed to suppress the thermal drift, which results in stabilizing nanometer scale tip to substrate gaps in SECM. Such a nanogap is essential for nanoscale SECM study such as nanoscale imaging or the fast kinetic measurement. My contributions in Chapters 6 include the theoretical simulation and its experimental validation for the SECM study of one dimensional nanostructures. Significantly, the theoretical simulation was extended to the three dimensional space. These achievements enabled me to successfully apply nanoscale SECM to the characterization of several important nanosystems. Based on these achievements, the capacity of nanoscale SECM will be greatly increased to characterize and understand various nanomaterials and interfaces at the nanoscale.

References

(1) J. Kim, A. Izadyar, N. Nioradze, S. Amemiya, Nanoscale Mechanism of Molecular Transport through the Nuclear Pore Complex as Studied by Scanning Electrochemical Microscopy, submitted to *J. Am. Chem. Soc.*, 2012

(2) A. Izadyar, J. Kim, S. Amemiya, Selective Modulation of Nuclear Pore Permeability Barrier by Lipophilic Ion, In preparation.

(3) M. Shen, R. Ishimatsu, J. Kim, S. Amemiya, Quantitative Imaging of Ion Transport at Single Nanopores by High-Resolution Scanning Electrochemical Microscopy, *J. Am. Chem. Soc.*, **2012**,134, 9856-9859.

(4) J. Kim, M. Shen, N. Nioradze, S. Amemiya, Stabilizing Nanometer Scale Tip-to-Substrate Gaps in Scanning Electrochemical Microscopy Using an Isothermal Chamber for Thermal Drift Suppression, *Anal. Chem.*, **2012**,84, 3489-3492.

(5) R. Ishimatsu, A. Izadyar, B. Kabagambe, Y. Kim, J. Kim, S. Amemiya, Electrochemical Mechanism of Ion–Ionophore Recognition at Plasticized Polymer Membrane/Water Interfaces, *J. Am. Chem. Soc*, **2011,** 133, 16300-16308

(6) N. Nioradze, J. Kim, S. Amemiya, Quasi-Steady-State Voltammetry of Rapid Electron Transfer Reactions at the Macroscopic Substrate of the Scanning Electrochemical Microscope, *Anal. Chem.*, **2011,** 83, 828-835.

(7) R. Ishimatsu, J. Kim, P. Jing, C. C. Striemer, D. Z. Fang, P. M. Fauchet, J. L. McGrath, and S. Amemiya, Ion-Selective Permeability of Ultrathin Nanoporous Silicon Membrane as Probed by Scanning Electrochemical Microscopy Using Micropipet-supported ITIES Tips, *Anal. Chem.*, **2010,** *82*, 7127-7134.

(8) J. Kim, H. Xiong, M. Hofmann, J. Kong, and S. Amemiya, Scanning Electrochemical Microscopy of Individual Single-Walled Carbon Nanotube, *Anal. Chem.*, **2010,** *82,* 1605-1607.

(9) Y. Wang, J. Velmurugan, and M. V. Mirkin, P. J. Rodgers, J. Kim, and S. Amemiya, Kinetic Study of Rapid Transfer of Tetraethylammonium at the 1,2-Dichloroethane/ Water Interface by Nanopipet Voltammetry of Common Ions, *Anal. Chem*., **2010**, *82*, 77-83.

(10) E. Kim, J. Kim, and S. Amemiya, Spatially Resolved Detection of a Nanometer-Scale Gap by Scanning Electrochemical Microscopy, *Anal. Chem.*, **2009**, *81*, 4788-4791.

(11) H. Xiong, J. Kim, E. Kim, and S. Amemiya, Scanning Electrochemical Microscopy of One-Dimensional Nanostructure: Effects of Nanostructure Dimensions on the Tip Feedback Current under Unbiased Conditions, *J. Electroanal. Chem.*, **2009**, *629*, 78-86.

A. Application of Nanoscale Scanning Electrochemical Microscopy

2. Nanoscale Mechanism of Molecular Transport through the Nuclear Pore Complex as Studied by Scanning Electrochemical Microscopy

This work has been submitted as J. Kim, A. Izadyar, N. Nioradze, S. Amemiya, Nanoscale Mechanism of Molecular Transport through the Nuclear Pore Complex as Studied by Scanning Electrochemical Microscopy, *J. Am. Chem. Soc.*, 2012

.

2.1 Introduction

The nuclear pore complex (NPC) is the proteinaceous nanopore that solely mediates molecular transport across the nuclear envelope between the nucleus and cytoplasm of a eukaryotic cell. Small molecules (<40 kDa) diffuse through the large pore of this multiprotein complex. The passively impermeable macromolecule tagged with a signal peptide is chaperoned through the nanopore by nuclear transport receptors (e.g., importins) owing to their interactions with barrier-forming proteins. Presently, this bimodal transport mechanism is not well understood and is described by controversial models. Herein, we report on a dynamic and spatially resolved mechanism for NPC-mediated molecular transport through nanoscale central and peripheral routes with distinct permeabilities. Specifically, we developed the nanogap-based approach of scanning electrochemical microscopy to precisely measure the extremely high permeability of the nuclear envelope to a small probe molecule, (ferrocenylmethyl)trimethylammonium. Effective medium theories indicate that the passive permeability of 5.9×10^{-2} cm/s corresponds to the free diffusion of the probe molecule through ~23 nanopores with a radius of 25 nm and a length of 35 nm. The peripheral routes were blocked by wheat germ agglutinin to yield two-fold lower permeability for 17 nm-radius central routes. This lectin was also used in fluorescence assays to find that importins facilitate the

transport of signal-tagged albumin not through the sufficiently large central route but through the impermeably thin peripheral route. We propose that this spatial selectivity is regulated by the conformational changes of barrier-forming proteins that transiently and locally expand the peripheral route while blocking the central route.

The nuclear pore complex (NPC) solely mediates the nucleocytoplasmic transport of both small molecules and macromolecules to play pivotal roles in gene expression[1] and delivery[2] as well as a model of biomimetic nanotransport systems.[3] The NPC is composed of ~30 distinct proteins called nucleoporins (nups) with a total mass of ~120 MDa. This multiprotein complex perforates the double-membraned nuclear envelope (NE) that separates the nuclear and cytoplasmic compartments of a eukaryotic cell.[4] The molecules that are smaller than 40 kDa diffuse through the large nanopore with a diameter of ~50 nm and a length of ~35 nm in the part spanning the NE (Figure 2-1A).[5] The interior of the NPC is nanostructured by transport barriers to block the passive transport of larger molecules into and out of the nucleus. Barrier-forming nups are rich in hydrophobic phenylalanine-glycine (FG) repeats and are highly conserved from yeast to metazoans both in structure and sequence. Interestingly, the passively impermeable macromolecule tagged with a nuclear localization signal (NLS) peptide can be chaperoned through the nanopore by nuclear transport receptors (e.g., importins) as an even larger receptor complex.[6] The signal- and importin-dependent transport is somehow facilitated by interactions between importins and FG domains.

Presently, the mechanism of the bimodal molecular transport through the NPC is not well understood despite its broad significance in biology, medicine, and nanoscience. Available transport data are controversial and do not unambiguously decide whether pathways for passive and facilitated transport are spatially distinct, partially shared, or entirely overlapping.[7] Subsequently, both spatial distribution and permeability of transport barriers in the nanopore are inconsistent among representative models (Figure 2-1B–D).[7f,8] For instance, the "forest" model was recently proposed for the yeast NPC to hypothesize that the nanopore is concentrically divided into central and peripheral zones by intrinsically disordered FG

domains (Figure 2-1B).[8a] Cohesive FG domains collapse and cluster through the central zone and also cover the pore wall. The coils of non-cohesive FG domains serve as springs to separate the aqueous peripheral zone from the hydrophobic central zone. This model predicts that the transiently expandable peripheral route mediates the importin-facilitated transport of an NLS-tagged cargo while both routes are permeable to passive transport. In contrast, the "oily-spaghetti" model hypothesizes the transport of importin–cargo complexes through the central aqueous channel surrounded by the coils or brushes of FG domains as the entropic barriers extended from the pore wall (Figure 2-1C).[8b] A similar concentric architecture was also considered in the reduction of dimensionality model[8c] and the self-regulated viscous channel model.[7f] These models, however, hypothesize that hydrophobic FG domains in the peripheral route are permeable to importin-cargo complexes while the aqueous central channel mediates passive transport. On the other hand, the selective phase/hydrogel model uniquely hypothesizes the homogeneous distribution of FG-rich nups in the nanopore (Figure 2-1D).[8d] Thus, the mesh or hydrogel of hydrophobic FG domains in the entire nanopore is permeable to both passive and facilitated transport.

In this work, we studied the distinct permeabilities and nanoscale dimensions of central and peripheral routes through the NPCs to reveal a dynamic and spatially resolved mechanism for this highly elaborate transport system. Significantly, this new set of information allows us to fully assess the representative transport models (Figure 2-1B–D) and also to propose the spatial distribution and permeability of transport barriers at the nucleoporin level. Specifically, we investigated the passive transport of a small probe molecule, (ferrocenylmethyl)trimethylammonium ($FcTMA^+$), through the NPCs by scanning electrochemical microscopy[9] (SECM) as described below. Molecular transport through central and peripheral routes was resolved by selectively blocking the latter route with wheat germ agglutinin (WGA; lectin from *Triticum vulgaris*).[10] With the aid of effective medium theories,[11] the nanoscale dimensions of central and peripheral routes were determined from the SECM permeability data in the presence and absence of WGA. On the other hand, we performed fluorescence transport assays to demonstrate that NLS-tagged bovine serum albumin (BSA) was chaperoned by importins only through

the peripheral route and was completely blocked by WGA. The dimensions of the transport routes were compared with those of importins and BSA to propose that the thin peripheral route expands transiently and locally to accommodate the large importin–BSA complex selectively. At the same time, the large central route blocks the protein complex. Interestingly, each of these unique requirements for the proposed transport mechanism can be satisfied with specific FG-rich nups.

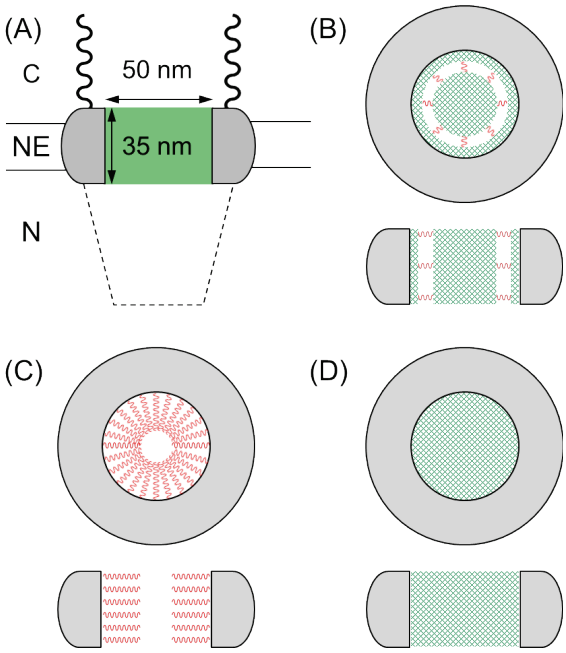

Figure 2-1. (A) NPC with a barrier region (green), cytoplasmic filaments (wavy line), and a nuclear basket (dotted line) embedded in the NE. C and N represent cytoplasmic and nucleus sides, respectively. (B–D) Top and side views of the barrier region with cohesive (green meshes) and non-cohesive (red wavy lines) FG domains (see the main text for the corresponding models).

Importantly, we developed the nanogap-based approach of SECM[12] to precisely measure the extremely high permeability of the NE to the small probe molecule, $FcTMA^+$, thereby yielding the

reliable dimensions of the transport routes. The formation of a nanometer-wide gap between an SECM tip and the NE was required to achieve high mass transport conditions[13] and also to reduce uncertainties in gap width and, subsequently, permeability.[11d] Nevertheless, the application of the powerful nanogap-based SECM approach for the measurement of fast interfacial kinetics has been limited to non-biological systems[12a-g] with the exception of the passive transport of lipophilic molecules across cell membranes.[12h] We enabled this challenging nanoscale measurement at the soft NE by developing a small and sharp Pt tip[12e] and a new SECM cell. With this setup, the local permeability of the NE under the tip was reliably measured in the SECM-induced transfer mode[11c,11d,13-14] (Figure 2-2). The functional dimensions of the transport routes thus determined from the SECM transport data confirmed their structural dimensions as measured by cryo-electron tomography[5] and super-resolution fluorescence microscopy.[10b] Advantageously, SECM allows for the transport study of an intact NE in an aqueous solution,[13] where the large nucleus is readily isolated from a *Xenopus laevis* oocyte. In contrast, the NE of this widely used nucleus sample has been fixed or dried in the structural studies of the NPCs by various microscopy techniques.[5,10,15] This study confirms the relevance of the high-resolution structures of the pretreated NPCs to the transport properties of the untreated NPCs as studied by SECM under more physiological conditions.

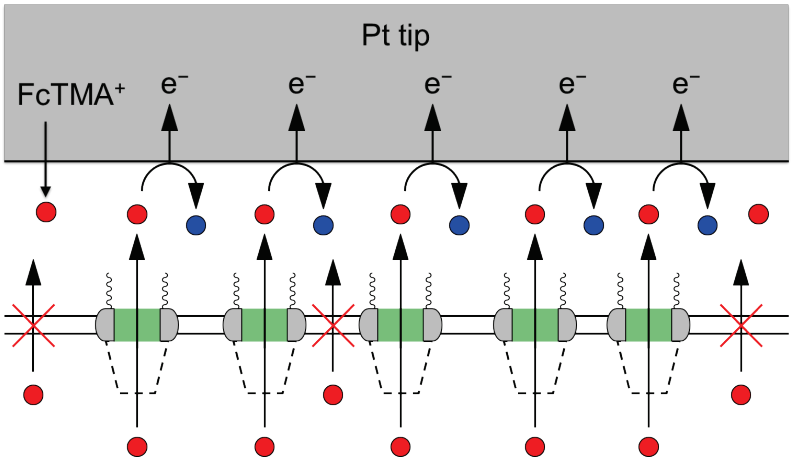

Figure 2-2. SECM-induced transfer mode for the measurement of the passive NE permeability to $FcTMA^+$. The blue circles represent the oxidized form of $FcTMA^+$.

2.2 Experimental Section

2.2.1 Chemicals. Poly(vinyl pyrrolidone) (PVP; average molecular weight, 40 kDa) was obtained from Sigma-Aldrich (St. Louis, MO). The hexafluorophosphate salt of $FcTMA^+$ was prepared by the metathesis of its iodide salt (Strem Chemicals, Newburyport, MA) and ammonium hexafluorophosphate (Strem Chemicals). Other reagents were used as received. All aqueous solutions were prepared with 18.3 $M\Omega \cdot cm^{-1}$ deionized water (Nanopure, Barnstead, Dubuque, IA).

2.2.2 Nucleus Isolation. A large nucleus (~380 µm in diameter; Figure S-1A) was isolated from the stage VI oocyte of a *Xenopus laevis* frog in the isotonic solution of mock intracellular buffer (MIB) at pH 7.4.[13] The isotonic MIB solution contained 15 g/L PVP in addition to 90 mM KCl, 10 mM NaCl, 2 mM $MgCl_2$, 1.1 mM EGTA, 0.15 mM $CaCl_2$, and 10 mM HEPES. Oocytes were extracted from the ovary cluster of an adult female frog[16] (NASCO, Fort Atkinson, WI) and stored at 18 ºC for less than three days prior to use.

2.2.3 Nucleus in the SECM Cell. The intact nucleus isolated from a *Xenopus* oocyte (Figure S-1A) was swollen in a newly developed SECM cell (Figure 2-3A) to smoothen the wrinkled and rough NE. The fabrication of the SECM cell based on three Si frames and the preparation of the NE sample in the cell are detailed in Supporting Information. Briefly, the isolated nucleus was swollen in the SECM cell filled with the hypotonic MIB solution of 5.5 g/L PVP to expand and smoothen the NE, which was detached from the nucleoplasm (Figure S-1B). In this cell, only a small patch of the self-standing NE was exposed to the tip through the 10 μm × 10 μm opening at the 1 μm-thick Si_3N_4 membrane of the top Si frame. The small opening was milled by using focused ion beam (FIB) technology (SMI3050SE FIB-SEM, Seiko Instruments, Chiba, Japan) without breaking the thin Si_3N_4 membrane (Figure S-2). The expanded NE made contact with the top Si_3N_4 membrane to stabilize the NE patch. A high-resolution digital video microscope (VZ-400, CALTEX Scientific, Irvine, CA) was used to confirm the contact (Figure 3B). Preliminary SECM experiments demonstrated that a tip approached closer to the NE exposed from a smaller square opening with edges of 10 μm, than of 25 μm. In addition, the edges of the 500 μm × 500 μm aperture of the middle Si frame supported the self-standing NE (Figure 2-3A).

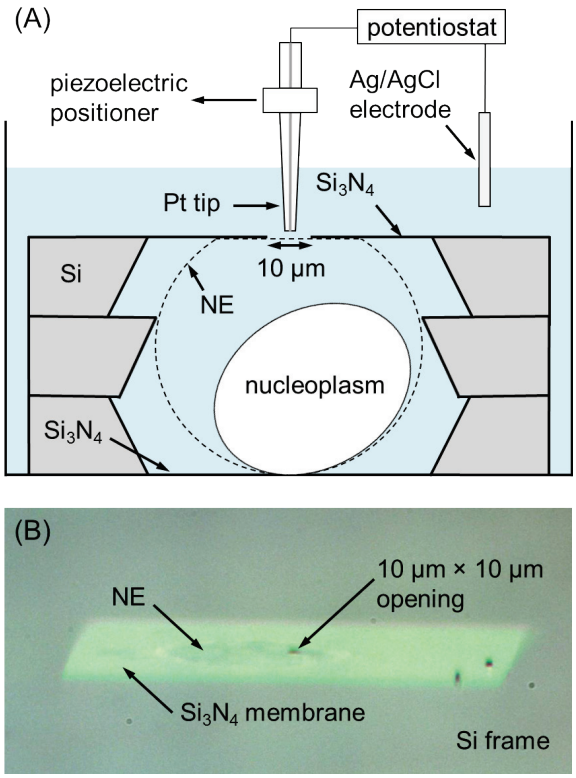

Figure 2-3. (A) SECM cell with a swollen nucleus. (B) Video microscopic image of the NE in contact with the top Si_3N_4 membrane of the cell.

2.2.4 Fabrication and Characterization of SECM Tip. A small and sharp Pt tip with a radius of ~0.5 µm and an outer glass radius of ~1 µm was fabricated as reported elsewhere.[12e] Each tip was milled by FIB and characterized by FIB, SEM, and cyclic voltammetry (Figure S-3).

2.2.5 SECM Approach Curve Measurement. An SECM instrument with closed-loop piezoelectric positioners (CHI 910B, CH Instruments, Austin, TX) was used for approach curve measurements. The microscope was placed on a vibration isolation platform (model 63-533, TMC, Peabody, MA). A two-electrode setup was employed with an FIB-milled Pt tip and a 1 mm-diameter AgCl-coated Ag wire as a reference/counter electrode. The SECM cell (Figure 2-3A) was filled with the hypotonic MIB solution of 0.3 mM $FcTMA^+$, where 1.0 g/L WGA was also added when its blocking

effect on the NE permeability was studied. Before the tip approached to the NE, the tip end was positioned above the center of the 10 μm × 10 μm opening of the top Si_3N_4 membrane as confirmed using a pair of the high-resolution video microscopes from *x* and *y* directions. The tip end was positioned just above the center of the square opening when a grid line on the monitor connects the tip end with its reflection through the center of the front edge of the square opening in each direction (see Figure 2-4A for the *x* direction). All SECM measurements were performed at room temperature.

2.2.6 Fluorescence Transport Assay. General procedures for the fluorescence microscopy assay of the NE permeability to BSA were reported elsewhere.[13] A transport medium was based on the hypotonic MIB solution of 0.5 μM sulforhodamine-labeled and NLS-tagged BSA (Sigma-Aldrich) with or without 0.5 μM importin α_2 (Novus Biological, Littleton, CO), 0.5 μM importin β_1 (Sigma-Aldrich), and energy mix (2 mM ATP, 25 mM phosphocreatine, 30 units/mL creatine phosphokinase, 200 μM GTP). The nucleus was swollen in the hypotonic MIB solution for 35 min, transferred and incubated in the transport medium with or without 0.3 mM $FcTMA^+$ for 10 min, rinsed with a small volume of the hypotonic MIB solution, and then imaged in a microchamber filled with the hypotonic MIB solution. The importin-facilitated transport of NLS-attached BSA was also studied using the swollen nucleus that was incubated in the hypotonic MIB solution containing 1.0 g/L WGA (Sigma-Aldrich) for 25 min.

2.3 Result and Discussions

2.3.1 SECM Approach Curves at the NE. SECM approach curves were measured at the large NE of an isolated *Xenopus* oocyte nucleus to characterize its passive permeability to $FcTMA^+$. The isolated nucleus was swollen in the SECM cell (Figure 2-3A) to expose only the patch of the expanded and self-standing NE through the 10 μm × 10 μm opening of the cell. The resultant smooth and stable NE allowed for the formation of a nanometer-wide gap under a small and sharp Pt tip with a radius, *a*, of ~0.5 μm as surrounded by a thin glass sheath with an outer radius, r_g, of ~1 μm. The tip surface was milled by using FIB technology to be smoothened and perpendicular to the length of the tip body[12e] (Figure S-3A

and B). This nanofabricated SECM tip with high quality can approach to ~25 nm from a flat SiO_2 substrate without contact (Figure S-4). When the tip was positioned far from the NE, the stable amperometric current based on the diffusion-limited oxidation of $FcTMA^+$ was obtained as given by

$$i_{T,\infty} = 4xnFD_w c^* a \quad (1)$$

where x is a function of RG (= r_g/a),[17] n is the number of transferred electrons (= 1) in the tip reaction, and D_w (=5.4 × 10^{-6} cm^2/s) and c^* (= 0.3 mM) are the diffusion coefficient and concentration of $FcTMA^+$ in the hypotonic MIB solution, respectively. The tip radius was determined from $i_{T,\infty}$ using the r_g value in the FIB image of each milled tip (Figure S-3B).

A well-defined approach curve was obtained during the tip approach to the NE in the absence of WGA. The tip was positioned at ~25 μm above the center of the opening (Figure 2-4A) and moved toward the NE to move through the opening, contact the NE, and then push it (Figure 2-4B). The amperometric tip current, i_T, decreased significantly at tip displacements of >24 μm, where the ~0.5 μm-radius tip approached within ~1 μm from the NE (red line in Figure 2-4C). The tip current decreased because the diffusional flux of $FcTMA^+$ induced by its oxidation at the tip was mediated only through the NPCs and was blocked by the reminder of the NE (Figure 2-2). This decrease in the tip current is not due to a negative feedback effect from an insulating edge of the 10 μm × 10 μm opening (Figure 2-3A) because the edges were far from the tip that moved through the center of the opening. When the tip end moved within a feedback distance (<1 μm) from an edge of the opening, the edge made contact with the tapered glass sheath surrounding the tip to disrupt the tip current. Eventually, the tip–NE contact was made at a tip displacement of 25.26 μm, which corresponds to a very short tip–NE distance of ~130 nm as confirmed theoretically (see below). The further tip movement lowered the tip current because the diffusion of $FcTMA^+$ to the tip was hindered more by the tighter coverage of the tip with the NE. Afterward, the tip current was nearly unchanged until the tip stopped. This result indicates that the tip

pushed the NE rather than penetrated through the NE, where the tip should have been exposed to the fresh MIB solution of $FcTMA^+$ in the nucleus to recover $i_{T,\infty}$.[18]

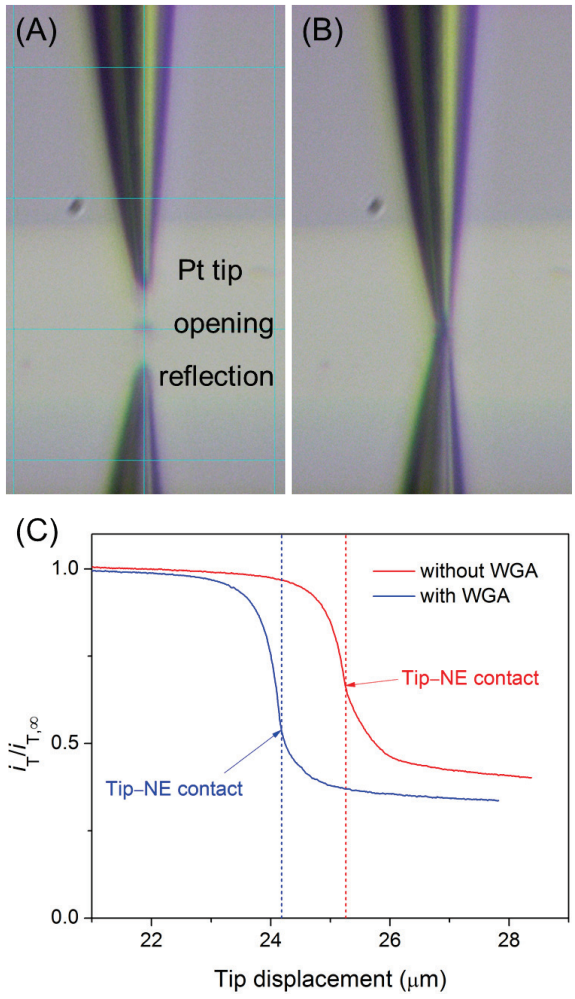

Figure 2-4. Video microscopic images of a FIB-milled Pt tip positioned (A) above and (B) in the 10 μm × 10 μm opening of the SECM cell. (C) Approach curves at the NE in the hypotonic MIB solution of 0.3 mM $FcTMA^+$ with and without 1.0 g/L WGA. Tip potential, 0.55 V vs. Ag/AgCl. Tip approach rate, 0.30 μm/s.

An approach curve was also measured at the NE in the presence of 1.0 g/L WGA as a blocker of the periphery of the NPC nanopore[10] (blue line in Figure 2-4C). In comparison to the WGA-free condition,

the tip current dropped more quickly near the WGA-bound NPCs and reached a lower level after the tip–NE contact, where the tip was covered with the less permeable NE. The theoretical analysis of the approach curves in the presence and absence of WGA also clarifies that the WGA-bound NPC was partially blocked and less permeable to $FcTMA^+$ than the WGA-free NPC (see below). Noticeably, tip displacements at the tip–NE contact were different only by ~1 μm for the two independent approach curves. This result indicates that the initial tip positions were precisely controlled within ~1 μm by using the high-resolution video microscopes. With this high precision, the tip was positioned over the center of the 10 μm × 10 μm opening (Figure 2-4A) to avoid a negative feedback effect from its edges.

2.3.2 Determination of the NE Permeability to $FcTMA^+$ by Finite Element Simulation. The extremely high permeability of the NE to $FcTMA^+$ with and without 1.0 g/L WGA was determined by fitting experimental approach curves to theoretical curves. The theoretical curves were obtained by the finite element simulation of a 2-phase SECM diffusion problem[13,14b] (see Supporting Information). In this work, 3D simulation was required for defining the square opening through the top Si_3N_4 membrane in the SECM cell. The tip current was calculated from the simulated concentration profile of $FcTMA^+$ at various tip–NE distances, d (Figure 2-5A). In this simulation, the NE was treated as a laterally homogeneous membrane with unique permeability, k_{NE}, as given by (see also eq 6),[11c,11d,13]

$$\text{FcTMA (outer solution)} \underset{k_{NE}}{\overset{k_{NE}}{\rightleftharpoons}} \text{FcTMA (nucleus)} \qquad (2)$$

where the same permeability for the passive import and export of $FcTMA^+$ corresponds to the equal bulk concentration of $FcTMA^+$ in the outer MIB solution and the nucleus swollen with the outer solution. Since $FcTMA^+$ freely diffuses through the NPCs (see below), a kinetic effect on an approach curve is

exerted from the impermeable region of the NE (Figure 2-2A). This kinetic effect is seen as the locally discontinuous profile of the $FcTMA^+$ concentration across the NE under the tip (Figure 2-5A). This simulation result also shows that the concentration profile was not affected by the edges of the opening of the top Si_3N_4 membrane because the edges were far from the tip. In fact, the negative approach curve simulated for an impermeable membrane in place of the NE agreed well with the theoretical approach curve based on the negative feedback effect from a flat insulating substrate[17] (Figure 2-5B).

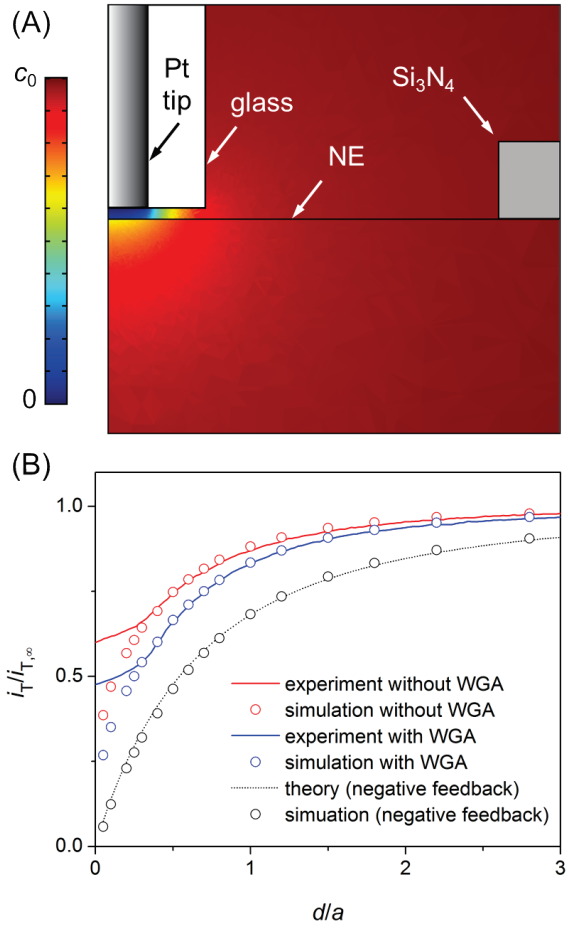

Figure 2-5. (A) Cross section of the concentration profile of $FcTMA^+$ around the tip–NE nanogap as simulated by the finite element method with $d/a = 0.3$ in Figure S-5A. (B) Experimental and simulated approach curves at the NE with and without 1.0 g/L WGA. The respective simulation curves employed a

= 0.44 μm and 0.42 μm with RG = 2.5. The theoretical negative approach curve was calculated for RG = 2.5.[17]

Experimental approach curves in the absence and presence of WGA agreed very well with simulated approach curves (Figure 2-5B) to yield the passive NE permeability, k_{NE}, of 5.9×10^{-2} and 3.1×10^{-2} cm/s, respectively. The lower permeability in the presence of WGA is still high and is due to the partial blockage of the NPC nanopore by the binding of WGA to the pore periphery.[10] The numerical analysis also shows that the contact of the tip with the NE occurred at nanoscale separations of ~130 nm. Importantly, these nanoscale tip-NE distances were required to resolve the approach curves as obtained in the presence and absence of WGA. In this distance range, the tip current decreased more rapidly when the tip approached WGA-bound NPCs. In addition, a mass transfer coefficient, D_w/d, of 4.5×10^{-1} cm/s across the nanoscale tip-NE gap is several times higher than the k_{NE} values, thereby confirming the reliability of these high permeability values. In our previous study,[13] such nanoscale tip–NE distances were not achievable by approaching larger SECM tips (2–10 μm) with a thick glass sheath (RG = 10) to the wrinkled and rough NE of the *Xenopus* oocyte nucleus isolated in the isotonic MIB solution (Figure S-1A). Subsequently, not only approach curves were limited by the diffusion of probe molecules but also the NE permeability was overestimated (>0.69 cm/s for $FcTMA^+$) because of a significant uncertainty in the tip–NE distance.[11d] In fact, the NE permeability determined by nanogap-based SECM in this work is much lower and is consistent with the expected size and density of the NPC (see below).

2.3.3 Nanoscale Dimensions of Central and Peripheral Zones. The permeabilities of the NE to $FcTMA^+$ as measured by nanogap-based SECM were related to the nanoscale dimensions of central and peripheral routes through the NPC nanopore (Table 1). A theoretical relationship between the passive permeability and structural properties of a nanoporous membrane is given by effective medium theories as[11d]

$$k_{NE} = \frac{2ND_w r}{2l/\pi r + 1} \quad (3)$$

where a planar membrane is randomly perforated by cylindrical nanopores with a radius of r and a depth of l at a density of N. Eq 3 is based on the assumption that the passive permeability is controlled by 3 diffusion steps at a pore (Figure 2-6A). These steps are the diffusion of a transported molecule (i) from the solution to the pore orifice, (ii) through the pore, and (iii) from the opposite pore orifice to the adjacent solution. In addition, it is assumed that the diffusing molecule does not interact with any NPC component, which includes cytoplasmic filaments, nucleoplasmic baskets, pore wall, and transport barriers in the pore. This assumption leads to the same diffusion coefficient of $FcTMA^+$ in the nanopore and MIB. The validity of the equal diffusion coefficient is discussed in the following section.

Eq 3 gives a good agreement between the k_{NE} value in the absence of WGA and the structural properties of the NPC determined by high-resolution microscopy techniques. The high NE permeability of 5.9×10^{-2} cm/s to $FcTMA^+$ in the absence of WGA corresponds to N = 42 NPCs/μm^2 in eq 3 with r = 25 nm and l = 35 nm for the NE-spanning part of the NPCs (Table 1). These r and l values were measured by cryo-electron tomography of the nucleus isolated from a mature *Xenopus* oocyte.[5] Moreover, the NPC density is consistent with a typical density of ~46 NPCs/μm^2 for a *Xenopus* oocyte nucleus as determined by AFM.[19] This result also indicates that ~23 NPCs with an external diameter of ~140 nm are closely packed under the 0.42 μm-radius Pt tip during the approach curve measurement. In fact, the NE permeability of a mature *Xenopus* oocyte nucleus is extremely high because of its exceptionally high NPC density.[19]

Table 2-1. Passive Permeability of the NE to $FcTMA^+$ without and with WGA and the corresponding dimensions and density of the NPC.

WGA	k_{NE}, cm/s	D_w/D_{NPC}	r, nm	l, nm	N, μm^{-2}
–	0.059[a]	1	25	35	42
+	0.032[a]	1	17	35	42
–	0.031[b]	3	25	35	42
+	0.012[b]	3	17	35	42

[a] Determined from experimental approach curves at the NE and related to r, l, and N values using eq 3. [b] Calculated using eq 10 with the assumption of a 3 times smaller diffusion coefficient of $FcTMA^+$ in the NPC nanopore, D_{NPC}, than in the hypotonic MIB solution.

The nanoscale dimensions of central and peripheral routes in the NPC were determined from the NE permeability to $FcTMA^+$ in the presence of WGA. Since peripheral routes are blocked by WGA,[10] the resulting lower permeability of 3.1×10^{-2} cm/s is due to the passive transport of $FcTMA^+$ through central routes (Figure 6B). This permeability value corresponds to a radius of 17 nm for the central route in eq 3 when the density and length of the NPC nanopore are unchanged by the binding of WGA to the peripheral

zone. The difference between the radii of the entire nanopore and central route gives a thickness of 8 nm for the peripheral route.

Remarkably, the dimensions of central and peripheral routes thus determined from the SECM permeability data agree very well with those determined by super-resolution fluorescence microscopy of single NPCs.[10b] In the super-resolution images, fluorescence-labeled WGA was positioned at ~20 nm from the center of the NPC of a *Xenopus* oocyte nucleus. Therefore, a radius of 17.5 nm is estimated for the WGA-free central zone when the position and radius (2.5 nm[20]) of WGA are considered. The peripheral route with a thickness of 7.5 nm is left in the range of 17.5–25 nm from the pore center.

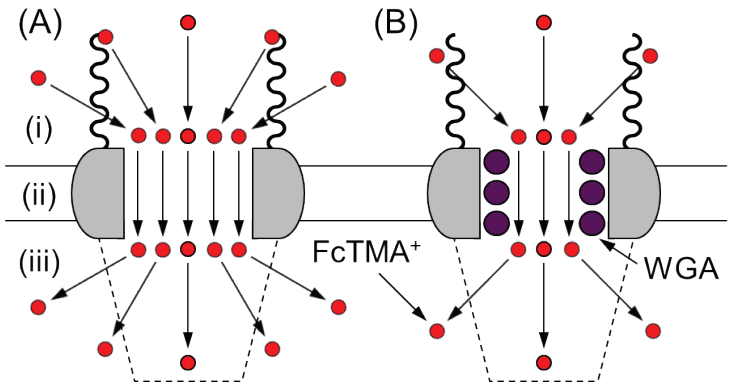

Figure 2-6. Three-step diffusion of $FcTMA^+$ through the NPC in the (A) absence and (B) presence of WGA. Each step is explained in the text.

2.3.4 Free Diffusion of $FcTMA^+$ through the Entire Nanopore. Our SECM data indicates that $FcTMA^+$ diffuses through the entire region of the NPC nanopore as freely as in the aqueous solution. The lower, but significantly high permeability of the WGA-bound NE to $FcTMA^+$ (Figure 2-5B) demonstrates that both central and peripheral routes mediate this passive transport. Additionally, a good agreement between the SECM permeability data and the structural data validates an assumption for eq 3, i.e.,

$FcTMA^+$ freely diffuses through the entire nanopore without significant interactions with any component of the NPC including transport barriers. In fact, a Stokes radius of 0.43 nm for $FcTMA^+$ is much smaller than a passive limit of ~2.6 nm Stokes radius for the NPC.[7c] Moreover, the charged regions of FG-rich nups[8a] are screened by the pore-filling MIB solution with a high ionic strength of ~0.11 M, thereby exerting a negligible electrostatic effect on $FcTMA^+$.

The free diffusion of $FcTMA^+$ through the entire NPC nanopore apparently contradicts the slow passive transport localized through the central zone as observed by single-molecule fluorescence microscopy.[7f] For instance, the passive transport of single fluorescein molecules with a radius of 0.7 nm was localized around the central zone and was ~3 times slower than expected from their diffusion coefficient in the aqueous solution. Significantly lower k_{NE} values, however, are expected for $FcTMA^+$ when its diffusion coefficient in the nanopore is 3 times smaller than that in the hypotonic MIB solution (Table 1; see Supporting Information for the calculation of the lower k_{NE} values). Moreover, an even lower k_{NE} value and no effect of WGA on k_{NE} are expected if the passive transport of $FcTMA^+$ is localized around the central zone. We speculate that the slow and localized passive transport of single fluorescein molecules is due to their adsorption to FG-rich nups in the central zone. This adsorption effect is enhanced when all adsorption sites are free and available for a single molecule in the absence of already adsorbed molecules.[21] In contrast, these adsorption sites may be saturated with $FcTMA^+$ at the concentration of 0.3 mM used in our SECM experiments.

2.3.5 Facilitated Transport of BSA through the Peripheral Route. We also performed fluorescence transport assays to demonstrate that the signal- and importin-dependent transport of BSA is solely mediated through the peripheral route. The NE of a swollen nucleus was incubated with rhodamine-labeled and NLS-tagged BSA and investigated by fluorescence microscopy. No fluorescence was seen in the nucleus incubated in the BSA solution containing no importin (Figure 2-7A) because BSA (~67 kDa) is larger than the passive limit of the NPC. This result also confirms that the self-standing NE detached from the nucleoplasm of a swollen nucleus (Figure 2-9B) is intact and is not leaky. In

contrast, NLS-tagged BSA was transported into a swollen nucleus in the presence of importin α_2 and importin β_1 (Figure 2-7B). In this case, the former served as an adaptor, binding to both the latter and to the NLS peptide of BSA to form an NPC-permeable complex.[6] The signal- and importin-dependent transport as expected for the physiological NPC was also observed in the presence of $FcTMA^+$ (Figure 2-9C and D).

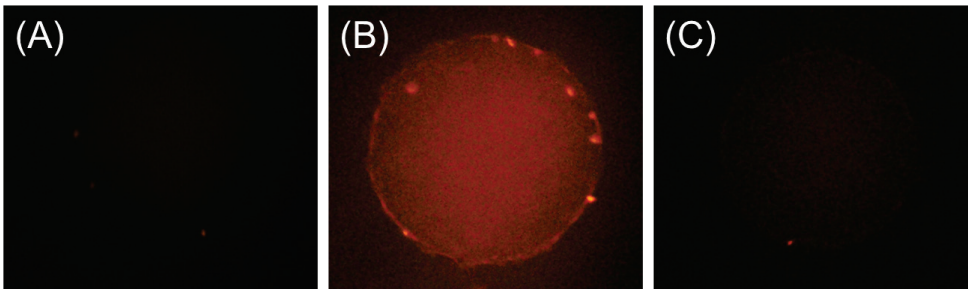

Figure 2-7. Fluorescence microscopic images of swollen nuclei in the hypotonic MIB solution of rhodamine-labeled and NLS-tagged BSA (A) without and (B and C) with importins and energy mix. In part (C), the nucleus was incubated with 1.0 g/L WGA before the fluorescence transport assay.

Importantly, the facilitated import of NLS-tagged BSA was completely blocked by WGA to yield no fluorescence in the nucleus (Figure 2-7C). This result indicates that an importin–BSA complex is transported only through the peripheral route, which is selectively blocked by the binding of WGA to the periphery of the NPC nanopore.[10] Noticeably, a recent single-molecule microscopy study spatially resolved the peripheral route as the dominant pathway for facilitated transport in the absence of WGA.[7f] This dynamic transport study, however, does not show whether the central route is impermeable to facilitated transport or only less permeable than the peripheral route. In contrast, our equilibrium fluorescence transport assay provides the unambiguous evidence that the WGA-free central route is impermeable to an importin–BSA complex.

2.3.6 Assessment of Controversial Models Based on Spatial Distribution of Passive and Facilitated Transport. Our SECM and fluorescence studies revealed the spatial distribution of both passive and facilitated transport through the NPC to support the forest model[8a] (Figure 2-1B) among the controversial transport models. As confirmed experimentally, the forest model hypothesizes that passive and facilitated transport shares the peripheral route while the central route is permeable only to passive transport. In contrast, other models are not fully supported by our results. The peripheral route is dominant for facilitated transport in the self-regulated viscous channel model[7f] and the reduction of dimensionality model.[8c] These models, however, hypothesize that passive transport is localized through the central route, which contradicts to the results of our SECM study. On the other hand, the hypotheses of facilitated transport through the central route and both routes in the "oily-spaghetti" model[8b] (Figure 1C) and the selective phase/hydrogel model[8d] (Figure 2-1D), respectively, are rejected by the results of our fluorescence transport assays.

2.3.7 A Dynamic Mechanism for Importin-Facilitated Transport. With the aid of the forest model,[8a] we propose a dynamic transport mechanism at the nucleoporin level to explain how importins chaperon a passively impermeable macromolecule through the thin peripheral route not through the large central route (Figure 2-8A). In this mechanism, we considered the central transport barrier composed of the FG-rich nups of the *Xenopus* NPC (Figure 2-8B) while the forest model was originally proposed for the yeast NPC (see ref. 8a for the forest model based on specific yeast nups). The dynamic transport mechanism was revealed by comparing the dimensions of the transport routes with those of BSA and importins as discussed below. Approximately, BSA is an oblate ellipsoid with dimensions of 14 nm × 4.2 nm × 4.2 nm[22] while the heterodimer of importin α (62 kDa) and importin β (98 kDa) possesses the maximum dimension of 19 nm and a radius of gyration of 5.7 nm.[23] Noticeably, the transport of a passively impermeable macromolecule through the 8 nm-thick peripheral route is blocked by both central and peripheral FG domains in our model.

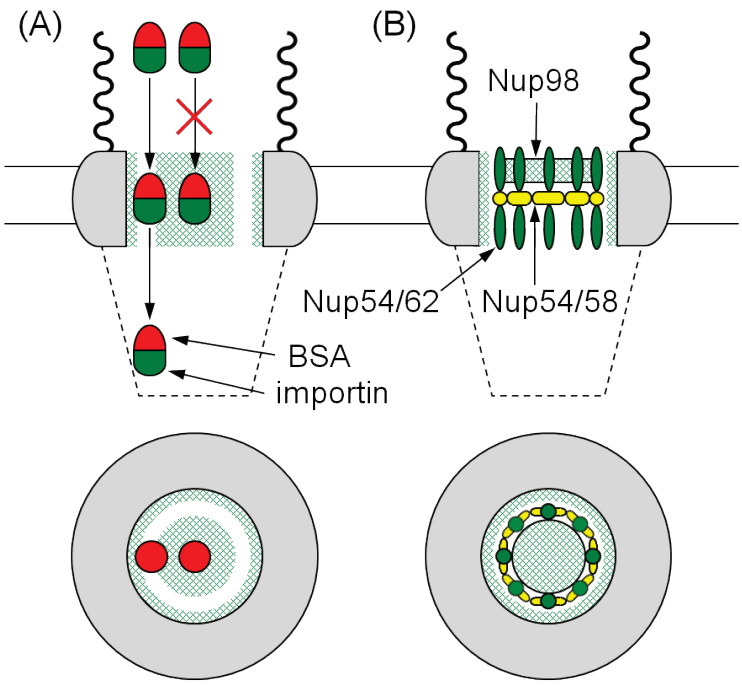

Figure 2-8. Side and top views of the barrier region of the NPC based on the forest model. Green meshes represent cohesive FG domains. In part (B), transport barriers in the central route are formed by the FG-rich nups of the *Xenopus* NPC. Nup 98 is anchored to the pore wall through Nup214 (not shown).[25]

In the proposed mechanism, the 8 nm-thick peripheral route is transiently and locally expanded during the translocation of a large importin–BSA complex by the conformational changes of Nup54 and Nup58. The analysis of their crystal structures predicted that their oligomers form a flexible ring at the pore midplane (Figure 8B) and dynamically change their conformations to fluctuate the ring radius between ~10 nm and ~20 nm.[24] With the internal pore radius of 25 nm, the respective ring radii corresponds to thicknesses of ~15 nm and ~5 nm for the peripheral route. The thickness of the expanded peripheral route is comparable even to the largest dimensions of BSA and the dimer of importin α and importin β (see above). In addition, it was proposed that this structural change is modulated by the

interactions of importins with the helices of Nup54 and Nup62 projected up and down from either side of the midplane ring (Figure 2-8B).[24]

Specifically, we propose that a part of the midplane ring formed by the oligomers of Nup54 and Nup58 contracts upon interactions with the importin of its BSA complex to locally open the adjacent region of the peripheral route and, subsequently, mediate the translocation of the complex (Figure 2-8B). In this model, the peripheral route can be also blocked by the binding of WGA to the *N*-acetylglucosamine groups of Nup62,[10c] which forms the periphery of the central barriers. Moreover, the most stable radius of ~18 nm as estimated for the midplane ring[24] is consistent with a radius of ~17 nm for the central route as determined from the SECM permeability data. In fact, the importin-driven change of the ring diameter was originally proposed for the gating of the central route.[24] This route, however, is impermeable to an importin–BSA complex.

We also propose that the facilitated transport of BSA through the large central route is blocked by Nup 98. This FG-rich nup is attached to Nup 62 at the cytoplasmic side and located above the midplane ring of the *Xenopus* NPC[25] (Figure 2-8B). Recently, the impermeability of Nup 98 to BSA was also demonstrated using the solid-state nanopore modified with Nup98 while this biomimetic NPC was permeable to importin β_1.[3b] We speculate that the FG domains of Nup98 are impermeable to the importin–BSA complex because the energy gained by the interactions of importin β_1 with the FG domains is not enough to compensate the energy required to break the cohesive domains for BSA and carry this aqueous protein through the hydrophobic domains (Figure 2-8A). In contrast, the expanded peripheral route provides a more aqueous pathway, where the hydrated protein complex is less exposed to hydrophobic FG domains during its translocation (Figure 2-8A). Noticeably, Nup98 of the natural NPC may be impermeable even to importin α and importin β because their transport is completely blocked by WGA.[26]

2.4 Conclusions

In this study, we obtained a new and comprehensive set of transport data to reveal a dynamic and spatially resolved mechanism for bimodal molecular transport through the NPC. The greater mechanistic understanding of this pivotal transport system at the nucleoporin level is broadly significant. Specifically, the 34 nm-diameter and 8 nm-thickness of central and peripheral routes, respectively, were determined by employing the nanogap-based approach of SECM with the FIB-fabricated tip and cell. In addition, we performed fluorescence assays to demonstrate the dominance of the peripheral route for the importin-facilitated transport of NLS-tagged BSA. All together, we propose the central transport barriers nanostructured by the FG-rich nups that are structurally flexible and are impermeable to an importin–BSA complex. The dynamic structure of the central barriers is required for expanding the thin peripheral route to facilitate the transport of the large protein complex through the resultant aqueous pathway. Apparently, this requirement is satisfied with the flexible ring formed by the oligomers of Nup54 and Nup58 in the midplane of the *Xenopus* NPC. This midplane ring is as large as the central route and is located under Nup98. Subsequently, the cohesive and hydrophobic FG domains of Nup98 block the transport of the aqueous protein complex through the large midplane ring. In contrast, the analysis of the SECM permeability data by effective medium theories indicates that $FcTMA^+$ freely diffuses through the central FG domains without significant steric or electrostatic interactions. The further application of the nanogap-based SECM approach to the probe molecules of various charges, sizes, and hydrophobicities[11d] will reveal the corresponding chemical natures of the FG-based transport barriers.

2.5 Supporting Information

2.5.1 Microscopic Characterization of the Isolated Nucleus. The nucleus was isolated from a *Xenopus laevis* oocyte and characterized microscopically. The large nucleus (~380 μm in diameter) isolated in the isotonic MIB solution had the wrinkled and rough NE (Figure 2-9A). The swelling of the isolated nucleus in the hypotonic MIB solution of 5.5 g/L PVP expanded and smoothened the NE (~580

μm in diameter), which was detached from the white nucleoplasm (Figure 2-9B). Noticeably, the self-standing NE of a swollen nucleus can selectively mediate the importin-facilitated transport of NLS-tagged BSA in the presence of 0.3 mM $FcTMA^+$ (Figure 2-9C and D).

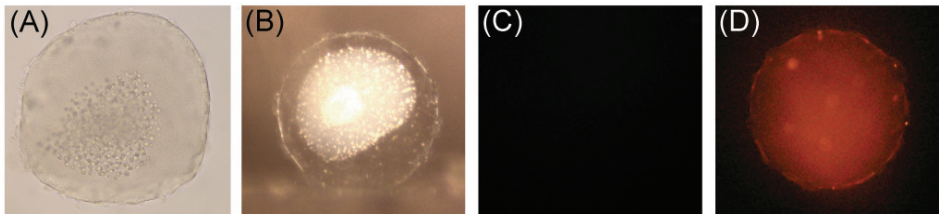

Figure 2-9. Optical and video microscopic images of the nuclei isolated from *Xenopus laevis* oocytes in the (A) isotonic and (B) hypotonic MIB solutions, respectively. Fluorescence microscopic images of swollen nuclei in the hypotonic MIB solution of rhodamine-labeled and NLS-tagged BSA and 0.3 mM $FcTMA^+$ in the (C) absence and (D) presence of importins and energy mix.

2.5.2 Fabrication of the SECM Cell. The SECM cell (Figure 3A) was fabricated by sandwiching a 3 mm-diameter Si disk frame with a 0.5 mm × 0.5 mm aperture (frame thickness, 0.2 mm; Ted Pella, Redding, CA) between a pair of 5 mm × 5 mm Si frames with a 1.0 μm-thick Si_3N_4 membrane (frame thickness, 0.2 mm; membrane size, 0.5 mm × 0.5 mm; Norcada, Edmonton, Canada). The middle frame was glued to the bottom frame by applying M-Bond 610 adhesive (Ted Pella) and polished to reduce the thickness of the frame composite to 380 ± 5 μm as measured by a micrometer. A 10 μm × 10 μm opening was milled through the center of the Si_3N_4 membrane of the top Si frame by FIB and characterized by SEM (Figure 2-10) using a dual-beam instrument (SMI3050SE FIB-SEM, Seiko Instruments, Chiba, Japan).

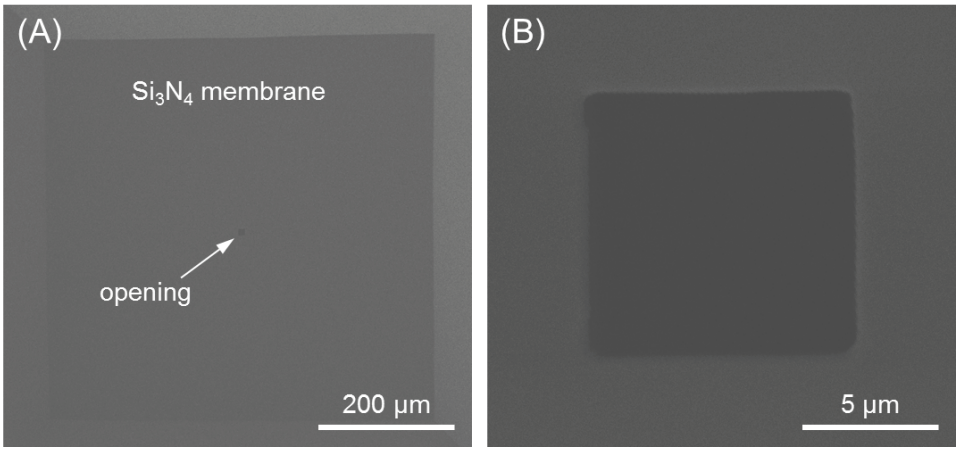

Figure 2-10. SEM images of the 10 μm× 10μm opening milled through the center of the Si_3N_4 membrane of the top Si frame by FIB.

2.5.3 Preparation of the Nucleus Sample in the SECM Cell. The isolated nucleus was transferred to the center of the cavity of the middle and bottom Si frames in the SECM cell (Figure 2-3A) filled with the isotonic MIB solution containing 15 g/L PVP and 0.3 mM $FcTMA^+$. The bottom frame was placed on the Plexiglass plate pretreated with 10 g/L of BSA (Sigma-Aldrich) at the 19 mm × 19 mm bottom part of a 12 mm-height Plexiglass cell. The two-thirds of the isotonic MIB solution was replaced with the MIB solution of 4.0 g/L PVP and 0.3 mM $FcTMA^+$ twice consecutively to dilute the PVP concentration to 5.5 g/L. The nucleus was swollen in the hypotonic MIB solution for 45 min. Then, the top Si frame with a 10 μm× 10 μm opening was dropped on the top of the middle Si frame pretreated with 2 μL Cell-Tak (BD Biosciences, Bedford, MA) as a biological adhesive. The nucleus was swollen further for 15 min until the NE detached from the nucleoplasm and made contact with the Si_3N_4 membrane (Figure 2-3B). For the SECM experiment with a blocker, WGA, the isolated nucleus was swollen in WGA free hypotonic solution for 45min as mentioned above. Subsequently, the two–third of the hypotonic MIB solution was replaced with a MIB of 4.7 g/L PVP containing 1.0 g/L WGA and 0.3mM $FcTMA^+$ three times consecutively to make the final concentration of WGA almost 1.0 g/L. Then,

the top Si frame was dropped above the nucleus as mentioned and the nucleus was swollen further for 20 min until the NE contacted the top Si_3N_4 membrane.

2.5.4 Fabrication and Characterization of the SECM Tip. A ~0.5 μm-radius Pt tip surrounded by a ~0.5 μm-thick glass sheath was fabricated and characterized as reported elsewhere.[27] Briefly, a mechanically pulled Pt tip [28] was heat-annealed to thin the surrounding glass sheath and was milled by FIB to smoothen and flatten the tip end as confirmed by SEM and FIB imaging (Figure 2-11A and 2-3B, respectively). In this work, a borosilicate glass capillary (1.0 mm outer diameter, 0.2 mm inner diameter, 200 mm length, Drummond Scientific Company, Broomall, PA) was used instead of a Pb-doped glass capillary to minimize the mechanical damage of the tip due to FIB milling. The FIB-milled tip gave a sigmoidal and nearly retraceable steady-state cyclic voltammogram of $FcTMA^+$ with a small capacitive current in the hypotonic MIB solution (Figure 2-11C).

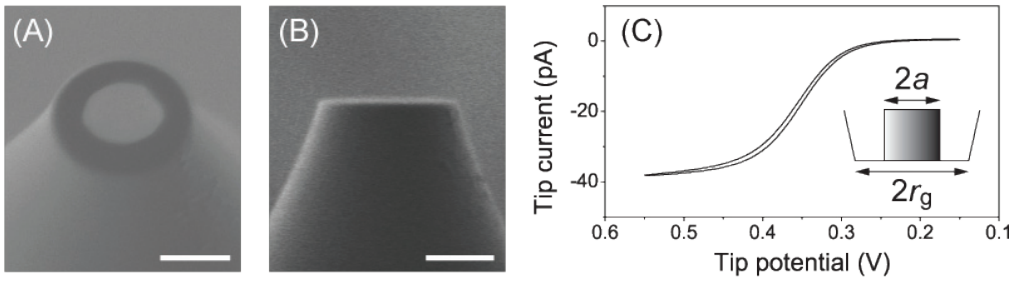

Figure 2-11. (A) SEM and (B) FIB images of a FIB-milled Pt tip. Scale bars, 1 μm. (C) Cyclic voltammogram of 0.3 mM $FcTMA^+$ in the hypotonic MIB solution at a scan rate of 20 mV/s. The tip potential was defined against an Ag/AgCl reference electrode.

Remarkably, the small and sharp SECM tip was able to approach to a distance of ~25 nm from the flat SiO_2 substrate without the tip-substrate contact. This short distance was determined by fitting an experimental curve at the insulating substrate with the theoretical curve based on a negative feedback effect at an inlaid disk tip[29] (Figure 2-12). The theoretical curve based on the hindered diffusion of $FcTMA^+$ to the tip is sensitive to *RG*.[30] A good fit of the experimental curve with the theoretical curve required r_g = 0.92 μm (i.e., *RG* = 1.8) as determined by SEM in addition to $D_w = 5.4 \times 10^{-6}$ cm^2/s and a = 0.51 μm.

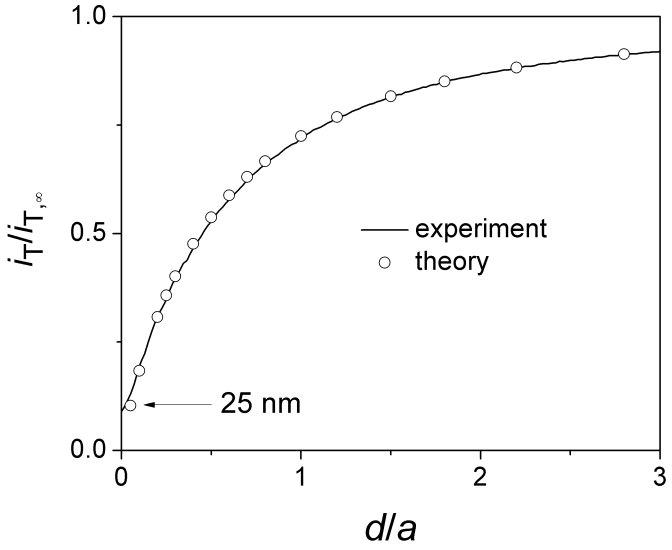

Figure 2-12. Normalized SECM approach curve at the SiO_2-coated Si wafer in the hypotonic MIB solution of 0.3 mM $FcTMA^+$. Tip potential, 0.55 V against an Ag/AgCl reference electrode. Tip approach rate, 0.30 μm/s. The theoretical curve was calculated for *RG* = 1.8.[29]

2.5.5 Finite Element Simulation. In this work, the three-dimensional SECM diffusion problem was solved using COMSOL Multiphysics finite element package (version 3.5a, COMSOL, Burlington, MA). The finite element simulation employed normalized parameters as defined elsewhere[31] (see the attached exmple of the simulation). For instance, the normalized NE permeability was defined as

$$K = \frac{k_{\mathrm{NE}} a}{D_{\mathrm{w}}} \tag{3}$$

In Cartesian coordinates, the origin of the coordinate axes was set at the center of the NE exposed from the square opening. The *z*-axis was defined along the length of the tip (Figure 2-13A). Actual simulations were carried out in a quarter of the entire domain because of symmetry planes at $x = 0$ and $y = 0$ (Figure 2-13B). The diffusion of $FcTMA^+$ in the outer solution and nucleus was defined by

$$\frac{\partial c_{\mathrm{w}}(x,y,z)}{\partial t} = D_{\mathrm{w}}\left[\frac{\partial^2 c_{\mathrm{w}}(x,y,z)}{\partial x^2} + \frac{\partial^2 c_{\mathrm{w}}(x,y,z)}{\partial y^2} + \frac{\partial^2 c_{\mathrm{w}}(x,y,z)}{\partial z^2}\right] \tag{4}$$

$$\frac{\partial c_{\mathrm{n}}(x,y,z)}{\partial t} = D_{\mathrm{w}}\left[\frac{\partial^2 c_{\mathrm{n}}(x,y,z)}{\partial x^2} + \frac{\partial^2 c_{\mathrm{n}}(x,y,z)}{\partial y^2} + \frac{\partial^2 c_{\mathrm{n}}(x,y,z)}{\partial z^2}\right] \tag{5}$$

where $c_{\mathrm{w}}(x, y, z)$ and $c_{\mathrm{n}}(x, y, z)$ are the concentrations of $FcTMA^+$ in the respective sides of the NE. The diffusion coefficient, D_{w}, and bulk concentraion, c^*, of $FcTMA^+$ are identical at both sides of the NE. The tip reaction was limited by the diffusion of $FcTMA^+$, which was depleted in the adjacent aqueous solution to induce its transport through the NPCs (Figure 2). The boundary condition at the NE was given by

$$D_{\mathrm{w}}\left[\frac{\partial c_{\mathrm{w}}(x,y,z)}{\partial z}\right]_{z=0} = D_{\mathrm{w}}\left[\frac{\partial c_{\mathrm{n}}(x,y,z)}{\partial z}\right]_{z=0} = k_{\mathrm{NE}}\left[c_{\mathrm{w}}(x,y,0) - c_{\mathrm{n}}(x,y,0)\right] \tag{6}$$

On the other hand, the Si_3N_4 membrane and the glass sheath of the tip were impermeable to $FcTMA^+$ to give zero flux across these boundaries. Boundary conditions at simulation space limits were given by the bulk concentration of $FcTMA^+$. The simulation space was large enough to give an error of less than 2% as estimated by comparing the simulated negative feedback current with the theoretical one in Figure 5B.

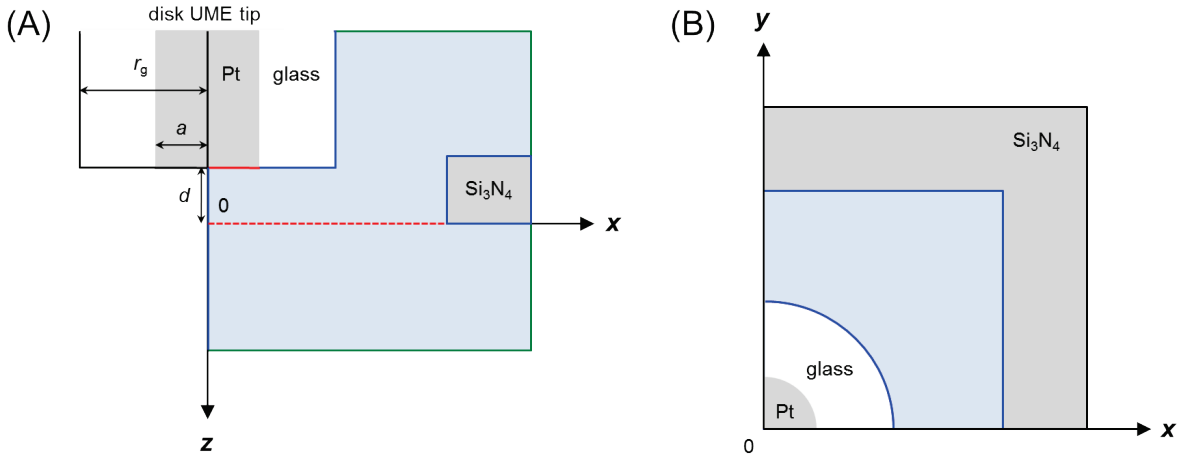

Figure 2-13. Cross sections of the SECM geometry at (A) *xz* and (B) *xy* planes. In part (A), 4 types of boundary conditions are defined in the simulation space (light blue). The boundary condition at the NE (red dotted line) is given by eq 6. The boundary condition at the tip (red solid line) is the diffusion-limited oxidation of $FcTMA^+$. There is no normal flux across the symmetry planes and impermeable surfaces (blue lines). Simulation space limits are shown by green lines.

2.5.6 Dependence of the NE Permeability on the Diffusion Coefficient of $FcTMA^+$ in the NPC Nanopore. Eq 3 was modified to implement the diffusion coefficient of $FcTMA^+$ in the NPC nanopore, D_{NPC}, when $D_w \neq D_{NPC}$ (Table 1). As reported elsewhere,[31] eq 3 was obtained from the following equation

$$k_{NE} = \frac{k_1 k_2}{k_1 + 2k_2} \tag{7}$$

where k_1 is based on the diffusion of $FcTMA^+$ between the orifice of the nanopore and the adjacent solution, i.e., steps (i) and (iii) in Figure 6A, and k_2 is based on the diffusion of $FcTMA^+$ through the nanopore, i.e., step (ii). When nanopores are randomly distributed, effective medium theories based on Brownian dynamics simulations give[32]

$$k_1 = 4 D_w N r \tag{8}$$

Assuming the planar diffusion of $FcTMA^+$ through the NPCs, we defined k_2 as

$$k_2 = \frac{\pi r^2 N D_{NPC}}{l} \tag{9}$$

The combination of eq 7 with eq 8 and eq 9 gives

$$k_{NE} = \frac{2 N D_w r}{2 l D_w / \pi r D_{NPC} + 1} \tag{10}$$

This equation was used to evaluate k_{NE} values in the third and fourth rows of Table 1, where $D_w = 3D_{NPC}$. Eq 10 with $D_w = D_{NPC}$ is equivalent to eq 3.

ACKNOWLEDGEMENTS

This work was supported by the National Institutes of Health (GM073439) and the National Science Foundation (CHE-1213452).

References

(1) (a) Terry, L. J.; Shows, E. B.; Wente, S. R. *Science* **2007**, *318*, 1412. (b) Strambio-De-Castillia, C.; Niepel, M.; Rout, M. P. *Nat. Rev. Mol. Cell Biol.* **2010**, *11*, 490.

(2) Pack, D. W.; Hoffman, A. S.; Pun, S.; Stayton, P. S. *Nat. Rev. Drug Discovery* **2005**, *4*, 581.

(3) (a) Jovanovic-Talisman, T.; Tetenbaum-Novatt, J.; McKenney, A. S.; Zilman, A.; Peters, R.; Rout, M. P.; Chait, B. T. *Nature* **2009**, *457*, 1023. (b) Kowalczyk, S. W.; Kapinos, L.; Blosser, T. R.; Magalhaes, T.; van Nies, P.; Lim, R. Y. H.; Dekker, C. *Nat. Nanotech.* **2011**, *6*, 433.

(4) Hoelz, A.; Debler, E. W.; Blobel, G. *Ann. Rev. Biochem.* **2011**, *80*, 613.

(5) Frenkiel-Krispin, D.; Maco, B.; Aebi, U.; Medalia, O. *J. Mol. Biol.* **2010**, *395*, 578.

(6) Görlich, D.; Kutay, U. *Annu. Rev. Cell. Dev. Biol.* **1999**, *15*, 607.

(7) (a) Kramer, A.; Ludwig, Y.; Shahin, V.; Oberleithner, H. *J. Biol. Chem.* **2007**, *282*, 31437. (b) Naim, B.; Brumfeld, V.; Kapon, R.; Kiss, V.; Nevo, R.; Reich, Z. *J. Biol. Chem.* **2007**, *282*, 3881. (c) Mohr, D.; Frey, S.; Fischer, T.; Guttler, T.; Görlich, D. *Embo J.* **2009**, *28*, 2541. (d) Herrmann, M.; Neuberth, N.; Wissler, J.; Perez, J.; Gradl, D.; Naber, A. *Nano Lett.* **2009**, *9*, 3330. (e) Fiserova, J.; Richards, S. A.; Wente, S. R.; Goldberg, M. W. *J. Cell Sci.* **2010**, *123*, 2773. (f) Ma, J.; Goryaynov, A.; Sarma, A.; Yang, W. *Proc. Natl. Acad. Sci. U.S.A.* **2012**, *109*, 7326.

(8) (a) Yamada, J.; Phillips, J. L.; Patel, S.; Goldfien, G.; Calestagne-Morelli, A.; Huang, H.; Reza, R.; Acheson, J.; Krishnan, V. V.; Newsam, S.; Gopinathan, A.; Lau, E. Y.; Colvin, M. E.; Uversky, V. N.; Rexach, M. F. *Mol. Cell. Proteomics* **2010**, *9*, 2205. (b) Macara, I. G. *Microbiol. Mol. Biol. Rev.* **2001**, *65*, 570. (c) Peters, R. *Traffic* **2005**, *6*, 421. (d) Frey, S.; Richter, R. P.; Görlich, D. *Science* **2006**, *314*, 815.

(9) (a) Amemiya, S.; Guo, J.; Xiong, H.; Gross, D. A. *Anal. Bioanal. Chem.* **2006**, *386*, 458. (b) Amemiya, S.; Bard, A. J.; Fan, F.-R. F.; Mirkin, M. V.; Unwin, P. R. *Ann. Rev. Anal. Chem.* **2008**,

1, 95. (c) *Scanning Electrochemical Microscopy*; 2nd ed.; Bard, A. J.; Mirkin, M. V., Eds.; CRC Press: Boca Raton, FL, 2012.

(10) (a) Akey, C. W.; Goldfarb, D. S. *J. Cell Biol.* **1989**, *109*, 971. (b) Loschberger, A.; van de Linde, S.; Dabauvalle, M. C.; Rieger, B.; Heilemann, M.; Krohne, G.; Sauer, M. *J. Cell Sci.* **2012**, *125*, 570. (c) Liashkovich, I.; Meyring, A.; Oberleithner, H.; Shahin, V. *J. Controlled Release* **2012**, *160*, 601.

(11) (a) Berg, H. C. *Random Walks in Biology*; Princeton University Press: Princeton, NJ, 1993. (b) Makhnovskii, Y. A.; Berezhkovskii, A. M.; Zitserman, V. Y. *J. Chem. Phys.* **2005**, *122*, 236102. (c) Kim, E.; Xiong, H.; Striemer, C. C.; Fang, D. Z.; Fauchet, P. M.; McGrath, J. L.; Amemiya, S. *J. Am. Chem. Soc.* **2008**, *130*, 4230. (d) Ishimatsu, R.; Kim, J.; Jing, P.; Striemer, C. C.; Fang, D. Z.; Fauchet, P. M.; McGrath, J. L.; Amemiya, S. *Anal. Chem.* **2010**, *82*, 7127.

(12) (a) Mirkin, M. V.; Richards, T. C.; Bard, A. J. *J. Phys. Chem.* **1993**, *87*, 7672. (b) Sun, P.; Mirkin, M. V. *Anal. Chem.* **2006**, *78*, 6526. (c) Velmurugan, J.; Sun, P.; Mirkin, M. V. *The J. Phys. Chem. C* **2008**, *113*, 459. (d) Shen, M.; Bard, A. J. *J. Am. Chem. Soc.* **2011**, *133*, 15737. (e) Nioradze, N.; Kim, J.; Amemiya, S. *Anal. Chem.* **2011**, *83*, 828. (f) Sun, P.; Zhang, Z. Q.; Gao, Z.; Shao, Y. H. *Angew. Chem., Int. Ed.* **2002**, *41*, 3445. (g) Li, F.; Chen, Y.; Sun, P.; Zhang, M. Q.; Gao, Z.; Zhan, D. P.; Shao, Y. H. *J. Phys. Chem. B* **2004**, *108*, 3295. (h) Sun, P.; Laforge, F. O.; Abeyweera, T. P.; Rotenberg, S. A.; Carpino, J.; Mirkin, M. V. *Proc. Natl. Acad. Sci. U.S.A.* **2008**, *105*, 443.

(13) Guo, J.; Amemiya, S. *Anal. Chem.* **2005**, *77*, 2147.

(14) (a) Yamada, H.; Matsue, T.; Uchida, I. *Biochem. Biophys. Res. Commun.* **1991**, *180*, 1330. (b) Barker, A. L.; Macpherson, J. V.; Slevin, C. J.; Unwin, P. R. *J. Phys. Chem. B* **1998**, *102*, 1586.

(15) (a) Keminer, O.; Siebrasse, J.; Zerf, K.; Peters, R. *Proc. Natl. Acad. Sci. U.S.A.* **1999**, *96*, 11842. (b) Moore-Nichols, D.; Arnott, A.; Dunn, R. C. *Biophys. J.* **2002**, *83*, 1421.

(16) Liu, X. S.; Liu, X. J. *Methods Mol. Biol. (Totowa, NJ, U.S.)* **2005**, 322, 31.

(17) Cornut, R.; Lefrou, C. *J. Electroanal. Chem.* **2007**, *604*, 91.

(18) (a) Tsionsky, M.; Zhou, J.; Amemiya, S.; Fan, F.-R. F.; Bard, A. J.; Dryfe, R. A. W. *Anal. Chem.* **1999**, *71*, 4300. (b) Amemiya, S.; Bard, A. J. *Anal. Chem.* **2000**, *72*, 4940.

(19) Wang, H.; Clapham, D. E. *Biophys. J.* **1999**, *77*, 241.

(20) Schwefel, D.; Maierhofer, C.; Beck, J. G.; Seeberger, S.; Diederichs, K.; Moller, H. M.; Welte, W.; Wittmann, V. *J. Am. Chem. Soc.* **2010**, *132*, 8704.

(21) Singh, P. S.; Chan, H.-S. M.; Kang, S.; Lemay, S. G. *J. Am. Chem. Soc.* **2011**, *133*, 18289.

(22) Zhang, F.; Skoda, M. W. A.; Jacobs, R. M. J.; Martin, R. A.; Martin, C. M.; Schreiber, F. *J. Phys. Chem. B* **2006**, *111*, 251.

(23) Falces, J.; Arregi, I.; Konarev, P. V.; Urbaneja, M. a. A.; Svergun, D. I.; Taneva, S. G.; Bañuelos, S. *Biochemistry* **2010**, *49*, 9756.

(24) Solmaz, S. R.; Chauhan, R.; Blobel, G.; Melcak, I. *Cell* **2011**, *147*, 590.

(25) Chatel, G.; Desai, S. H.; Mattheyses, A. L.; Powers, M. A.; Fahrenkrog, B. *J. Struct. Biol.* **2012**, *177*, 81.

(26) (a) Miyamoto, Y.; Saiwaki, T.; Yamashita, J.; Yasuda, Y.; Kotera, I.; Shibata, S.; Shigeta, M.; Hiraoka, Y.; Haraguchi, T.; Yoneda, Y. *J. Cell Biol.* **2004**, *165*, 617. (b) Kose, S.; Imamoto, N.; Tachibana, T.; Shimamoto, T.; Yoneda, Y. *J. Cell Biol.* **1997**, *139*, 841.

(27) Nioradze, N.; Kim, J.; Amemiya, S. *Anal. Chem.* **2011**, *83*, 828.

(28) Sun, P.; Mirkin, M. V. *Anal. Chem.* **2006**, *78*, 6526.

(29) Cornut, R.; Lefrou, C. *J. Electroanal. Chem.* **2007**, *604*, 91.

(30) Shao, Y.; Mirkin, M. V. *J. Phys. Chem. B* **1998**, *102*, 9915.

(31) Ishimatsu, R.; Kim, J.; Jing, P.; Striemer, C. C.; Fang, D. Z.; Fauchet, P. M.; McGrath, J. L.; Amemiya, S. *Anal. Chem.* **2010**, *82*, 7127.

(32) Makhnovskii, Y. A.; Berezhkovskii, A. M.; Zitserman, V. Y. *J. Chem. Phys.* **2005**, *122*, 236102.

3. Scanning Electrochemical Microscopy of Individual Single-Walled Carbon Nanotube

This work has been published as J. Kim, H. Xiong, M. Hofmann, J. Kong, and S. Amemiya, Scanning Electrochemical Microscopy of Individual Single-Walled Carbon Nanotube, *Anal. Chem.*, **2010,** *82,* 1605-1607.

3.1 Introduction

Here we report on novel application of scanning electrochemical microscopy (SECM) to enable spatially resolved electrochemical characterization of individual single-walled carbon nanotube (SWNT). The feedback imaging mode of SECM was employed to detect a pristine SWNT (~1.8 nm in diameter and ~2 mm in length) grown horizontally on a SiO_2 surface by chemical vapor deposition. The resulting image demonstrates that the individual nanotube under an unbiased condition is highly active for the redox reaction of ferrocenylmethyltrimethylammonium used as a mediator. Micrometer-scale resolution of the image is determined by the diameter of a disk-shaped SECM probe rather than by the nanotube diameter as assessed using 1.5 and 10 μm-diameter probes. Interestingly, the long SWNT is readily detectable using the larger probe although the active SWNT covers only ~0.05 % of the insulating surface just under the tip. This high sensitivity of the SECM feedback method is ascribed to efficient mass transport and facile electron transfer at the individual SWNT.

Electrochemistry of carbon nanotubes is a large and growing field that is both fundamentally and practically important.[1, 2] Unique physical and chemical properties of carbon nanotubes render them attractive electrode materials for electroanalysis and electrocatalysis. Most electrochemical studies of carbon nanotubes, however, have been carried out with an

ensemble of nanotubes with various structural and electronic properties, thereby limiting our knowledge about fundamental electrochemistry of carbon nanotubes. To overcome this limitation, electrodes based on individual single-walled carbon nanotubes (SWNTs) were fabricated to voltammetrically reveal their high activity for redox reaction.[3] Moreover, ex-situ SEM and AFM observation of metallic nanoparticles electrodeposited on a SWNT demonstrated preferential nucleation sites (or defects).[4, 5] Single molecule fluorescence microscopy was also employed for in-situ monitoring of adsorption and electrolysis of fluorescent redox molecules at discrete, nanometer-sized reactive sites on a SWNT.[6] These non-electrochemical microscopes, however, are applicable only to limited types of redox reactions although their superb spatial resolution is highly attractive.

Recently, we proposed a principle of scanning electrochemical microscopy (SECM)[7, 8] for spatially resolved electrochemical characterization of individual SWNTs (Figure 3-1).[9] In this SECM feedback method, a disk-shaped ultramicroelectrode is employed as a probe to electrolyze redox mediators at a diffusion-limited rate. When the tip is held less than a tip diameter away from the SWNT, the tip-generated species effectively diffuses to and reacts at the local surface of the SWNT just under the tip. Original mediators thus regenerated by the SWNT are detected at the tip with enhancing its amperometric current response. Consequently, the tip current enhancement based on the feedback effect serves as a measure of the rate of electron transfer at the nanotube surface. Importantly, significant feedback effect is expected even using a tip with the diameter that is much larger than the diameter of an active nanotube, because of the efficient mass transport at the nanotube.[9] Moreover, an electronically isolated SWNT is expected to give a quasi-steady-state feedback response when the nanotube is much longer than the tip diameter.[10, 11] The unbiased SWNT is not charged up by continuous mediator regeneration (step i in Figure

3-1), which is coupled with electron transport through the nanotube (step ii) and then with electrolysis of original mediators at the exterior sidewall beyond the outer tip diameter (step iii) to maintain charge balance in the nanotube. In fact, SECM was successfully applied to the study of externally unbiased carbon nanotube films as grown on insulating surfaces.[12, 13] No SECM study of an individual carbon nanotube, however, has been reported.

Here we report on proof-of-concept experiments to demonstrate SECM-based detection of an individual SWNT. To facilitate the experiments, we synthesized very long SWNTs horizontally aligned on a SiO_2-covered Si wafer by chemical vapor deposition as reported elsewhere.[14] The density of the SWNTs was lowered by employing a lower concentration of Fe nanoparticle catalyst. The long SWNTs are widely separated from the adjacent nanotubes as shown in an SEM image (Figure 3-2), where the arrow indicates the region of the SWNT investigated by SECM. Noticeably, each bright line in the SEM image corresponds to individual SWNT with diameters of ~1.3–2.0 nm as determined by AFM while the line is much thicker than the nanotube diameter because of charging effect on the surrounding SiO_2 surface.[14]

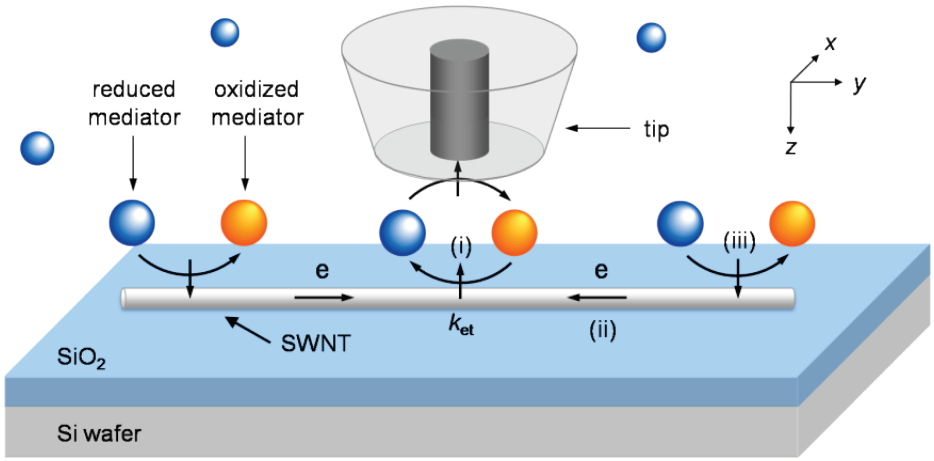

Figure 3-1. Scheme of an SECM feedback experiment with a disk ultramicroelectrode probe positioned above an individual SWNT as grown on an insulating substrate.

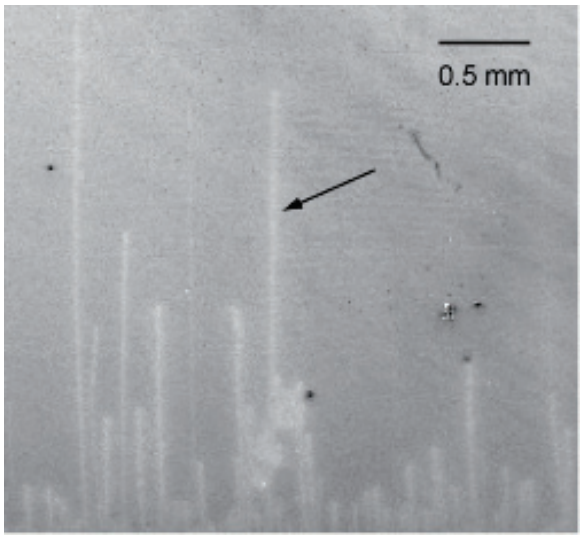

Figure 3-2. An SEM image of long SWNTs grown on a SiO_2/Si wafer at low density. The arrow indicates the region of the SWNT investigated in this work.

3.2. Results and Discussion

3.2.1 Detection of individual SWNT by feedback imaging mode of SECM

The feedback imaging mode of SECM was employed to detect the individual SWNT on the substrate immersed in an aqueous solution of 0.3 mM ferrocenylmethyltrimethylammonium ($FcTMA^+$) hexafluorophosphate and 0.1 M KNO_3 (see Supporting Information for details). Initially, a 10 μm-diameter Pt disk probe was biased at 0.35 V (vs Ag/AgCl) and positioned far from the substrate to obtain diffusion-limited tip current of $i_{T,\infty}$ = 430 pA for oxidation of $FcTMA^+$ as given by

$$i_{T,\infty} = 4nFDCa \quad (1)$$

where n is the number of electrons in the tip reaction (n = 1 for $FcTMA^+/FcTMA^{2+}$ couple), F is the Faraday constant, D and c are the diffusion coefficient and concentration of $FcTMA^+$ in the bulk aqueous solution, respectively, and a is the tip radius. Then, the tip was approached toward the SiO_2 surface (z-direction) until the tip current decreased to 225 pA (52 % of $i_{T,\infty}$) due to hindered diffusion of $FcTMA^+$ to the tip. This tip current corresponds to the tip–substrate distance, d, of 5.2 μm (d/a = 1.04) according to SECM theory.[15] Finally, the tip was held at the constant height and scanned over an individual SWNT in x- and y-directions to obtain a 40 μm × 40 μm image (Figure 3-3).

The SECM image clearly demonstrates the enhancement of tip current along the length of the SWNT (Figure 3-3). The enhanced tip current indicates that the tip-generated species,

$FcTMA^{2+}$, was reduced by the SWNT to regenerate $FcTMA^{+}$, thereby yielding the feedback effect. Importantly, only ~0.05 % of the substrate surface just under the 10 μm-diameter tip is covered by the SWNT with an effective local area of $A_{SWNT} = \sim 4\pi ra$ ($2r$ = 1.8 nm).[9] This extremely high sensitivity of SECM feedback detection is due to fast mass transport[9] and facile electron transfer at the SWNT (see below). Moreover, quasi-steady-state feedback responses that are independent of probe scan rate were obtained from the unbiased SWNT, which is much longer than the tip diameter to effectively mediate $FcTMA^{+}$ oxidation at the exterior sidewall (Figure 3-1).[10] The feedback effect from the SWNT is not limited by electron transport through the nanotube. The tip feedback current above a SWNT varies linearly with the mediator concentration from 0.3 mM (Figure 3-4a) to 1 mM (data not shown) so that the tip current normalized with respect to $i_{T,\infty}$ (eq 1) is independent of the concentration.

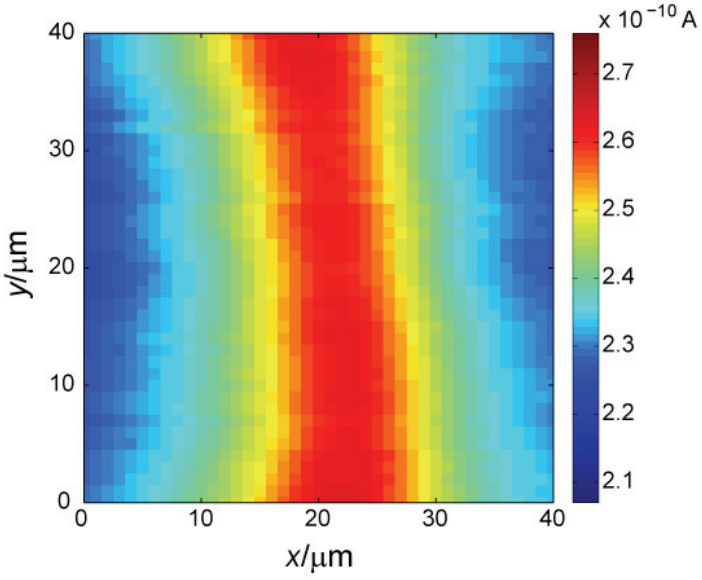

Figure 3-3. An SECM image of an individual SWNT as obtained using a 10 μm-diameter disk Pt probe at the tip–substrate distance of 5.2 μm. Probe scan rate, 15 μm/s.

3.2.2 Line scans over the length of an individual SWNT

The same SWNT was detected with higher spatial resolution using a smaller probe (1.5 μm in diameter). Similar SECM line scans were obtained along the length of the SWNT at four different positions separated every 10 μm (Figure 3-4a). This result corresponds to uniform reactivity of the nanotube at micrometer resolution determined by the tip diameter.[9] The half widths of the peaks are comparable to the tip diameter of 1.5 μm, indicating that a significant feedback effect is obtained from the SNWT when the nanotube is positioned under the edge of the disk probe (Figure 3-4b). The peak widths are much smaller than the corresponding peak widths as obtained with the 10 μm-diameter probe (Figure 3-3). Moreover, the line scan experiments allow us to determine the location of the SWNT with high precision, because the tip current reaches the maximum value when the center of the tip is positioned above the SWNT. With the 1.5 μm-diameter probe, the position of a SWNT was able to be determined with precision of ±100 nm (see Figure S1).

(a)

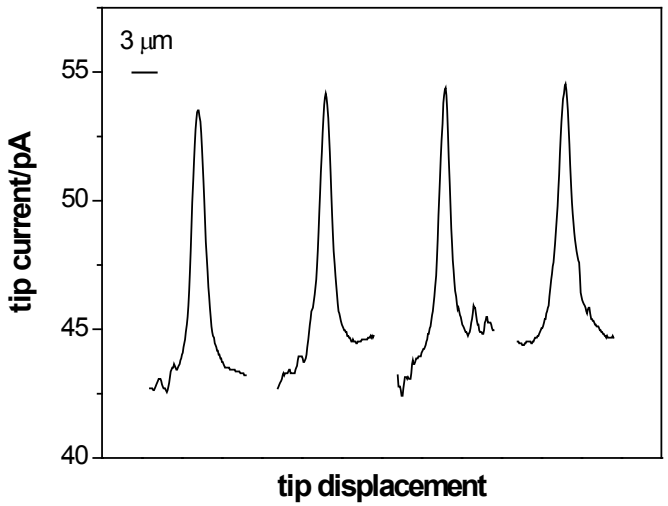

(b)

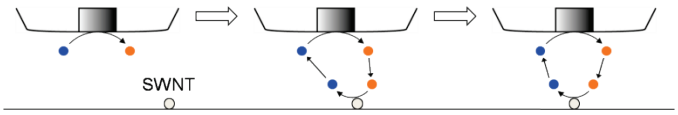

Figure 3-4. (a) SECM line scans of an individual SWNT at different positions along its length as obtained using a 1.5 μm-diameter disk Pt probe at the tip–substrate distance of 0.525 μm. Probe scan rate, 0.75 μm/s. (b) Scheme of an SECM line scan over an individual SWNT that is positioned (from left) far from, under the edge, and under the center of a disk SECM probe.

3.2.3 High electroactivity of the SWNT side wall

The significant feedback effect from a SWNT with a small effective area under the tip implies that mediator regeneration by the nanotube is very fast. In fact, a large rate constant for heterogeneous electron transfer at the SWNT is estimated from the peak currents in the line scan data. In an SECM line scan, the difference in the tip current above the SWNT and the SiO_2 surface (~ 10 pA in Figure 3-4a) corresponds to the feedback current based on mediator regeneration at the SWNT, i_{SWNT}.[9, 10] Assuming that (1) the open circuit potential of the long SWNT exposed to a $FcTMA^+$ solution is negative enough to result in electrochemically irreversible reduction of $FcTMA^{2+}$ at the sidewall under the tip[10, 16] and (2) the entire length of the SWNT on the insulating substrate is uniformly active and also uniformly accessible to redox molecules (see Supporting Information for numerical simulations of the accessibility), i_{SWNT} is approximated to

$$i_{SWNT} = nFA_{SWNT}k_{et}c_{SWNT} \quad (2)$$

where k_{et} is a rate constant for $FcTMA^{2+}$ reduction, and c_{SWNT} is the concentration of $FcTMA^{2+}$ at the nanotube surface under the tip. Since reduction of $FcTMA^{2+}$ at the nanotube results in $c_{SWNT} < c$ (= 0.3 mM), $k_{et} > 4.1$ cm/s is estimated from eq 2 with $2r = 1.8$ nm and $2a = 1.5$ μm. This large rate constant is not unexpected. An extremely large standard rate constant of $k^0 = 4 \pm 2$ cm/s was reported for the same redox couple at individual SWNTs, which were lithographically integrated into an electrode format and characterized voltammetrically.[3] Also, $k^0 > 3$ cm/s for this redox couple was estimated using a ultramicroelectrode based on a 2D network of SWNTs.[17] Moreover, the k_{et} value at the unbiased SWNT is larger than the corresponding k^0 value because the open circuit potential of the nanotube is more negative than the standard potential.

3.3 Conclusions

In summary, we demonstrated that SECM is a powerful electrochemical method that enables spatially resolved characterization of an individual SWNT as grown on an insulating substrate. High sensitivity of this SECM-based method not only allows for detection of a molecular wide SWNT using a micrometer-sized probe but also indicates that a pristine individual SWNT is highly active for electron transfer.

3.4 Supporting Information

3.4.1 Chemicals. Ferrocenylmethyltrimethylammonium hexafluorophosphate, $FcTMAPF_6$, was prepared by the metathesis of ferrocenylmethyltrimethylammonium iodide (Strem Chemical, Newburyport, MA) and ammonium hexafluorophosphate (Strem Chemical). A 0.1 KNO_3 solution containing 0.3 mM $FcTMAPF_6$ was prepared with 18.3 MΩ·cm deionized water (Nanopure, Barnstead, Dubuque, IA).

3.4.2 SECM Measurements. SECM experiments were conducted by employing a commercial SECM instrument with closed-loop piezoelectric motors (CHI 910B, CH Instruments, Austin, TX, USA) to control the position of a Pt disk probe at nanometer scale. A 1.5 μm-diameter probe with RG = 2 was fabricated by milling the tip of a glass-insulated Pt wire using a focused ion beam technique (SMI3050SE FIB-SEM, Seiko Instruments, Chiba, Japan), which will be described in the details of a future paper. A 10 μm-diameter probe with RG = 10 was purchased from CH Instruments. The inner and outer tip radii of the respective probes were checked by SEM and optical microscopy and then determined from current approach curves at a glass substrate.[18, 19] A 1 mm-diameter AgCl-coated Ag wire served as a reference/counter electrode. A SWNT sample was placed in a two-electrode cell such that the longest axis of the SWNTs is parallel to the *y*-direction of the piezoelectric motor (Figure 3-1).

3.4.3Accessibility of the Sidewall of an Individual SWNT. Here we demonstrate that uniform accessibility of the SWNT sidewall is a good approximation in eq 2 when mediator regeneration at the sidewall is kinetically limited. Specifically, we assess distribution of diffusional flux of mediator molecules at the sidewall of an individual SWNT using an approximate model proposed by Macpherson and co-workers[S3] (Figure 3-5). In this model, an axis of symmetry through the center of a cylindrical SWNT is assumed to reduce the problem to 2D diffusion. The width of the gap between the SECM tip and an insulating substrate with a SWNT is comparable to the tip radius, *a*, which is much larger than the

nanotube radius, r (a > 1000r in Figure 3-5). Diffusion of a tip-generated species, $FcTMA^{2+}$, in the gap reaches a steady state as defined by

$$D\left[\frac{\partial^2 c(x,z)}{\partial x^2}+\frac{\partial^2 c(x,z)}{\partial z^2}\right]=0 \qquad (3)$$

where $c(x, z)$ is the concentration of $FcTMA^{2+}$ (see Figure 2-1 for definition of x- and z-axes). The boundary condition at the SWNT sidewall is given by

$$J(\theta)=k_{et}c(\theta) \qquad 0\le\theta\le\pi/2 \qquad (4)$$

with

$$\tan\theta=\frac{x}{z+r} \qquad (5)$$

where $J(\theta)$ and $c(\theta)$ are normal flux and concentration of $FcTMA^{2+}$ at the sidewall, respectively. The original model was modified such that the mediator concentration at the simulation space limit is equal to the mediator concentration at the tip surface. This limit is so far from the SWNT that the corresponding boundary condition is determined by the tip reaction (see Figure 3-5b in ref. 21 for validation of this assumption). The other boundary conditions are given in Figure 18.

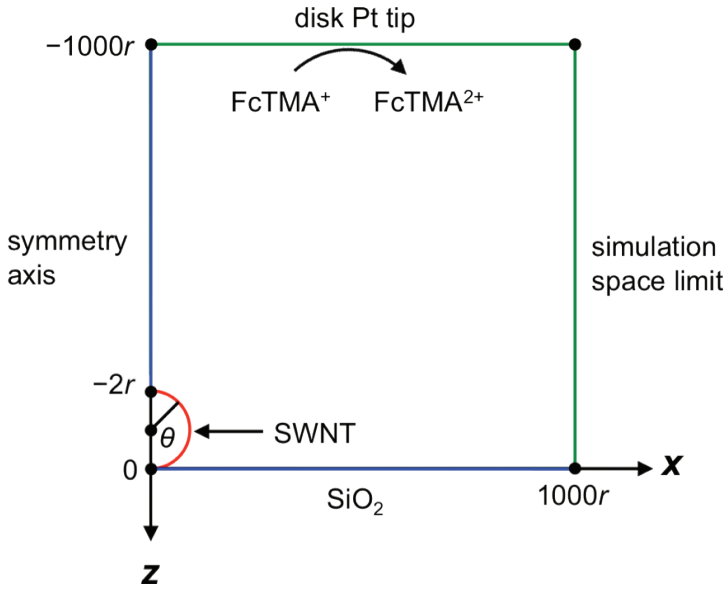

Figure 3-5. Geometry of the SECM diffusion problem in the Cartesian coordinate. There is no normal flux at blue lines while mediator concentration is equal to a bulk concentration at the green lines.

The two-dimensional diffusion problem was solved using Comsol Multiphysics 3.5a (COMSOL, Inc., Burlington, MA) to calculate distribution of the normal flux of mediator molecules at the sidewall. Dimensionless parameters were used in the attached simulation file, where an electron transfer rate constant is given in the dimensionless form as

$$K = \frac{k_{et} r}{D} \qquad (6)$$

Figure 3-6 shows normalized flux, $J(\theta)/J(\theta = \pi)$, thus simulated for K = 10, 1, and 0.1. The respective K values correspond to k_{et} = 1250, 125, and 12.5 cm/s in eq S4 with $2r$ = 1.8 nm and $D = 1.0 \times 10^{-5}$ cm^2/s.

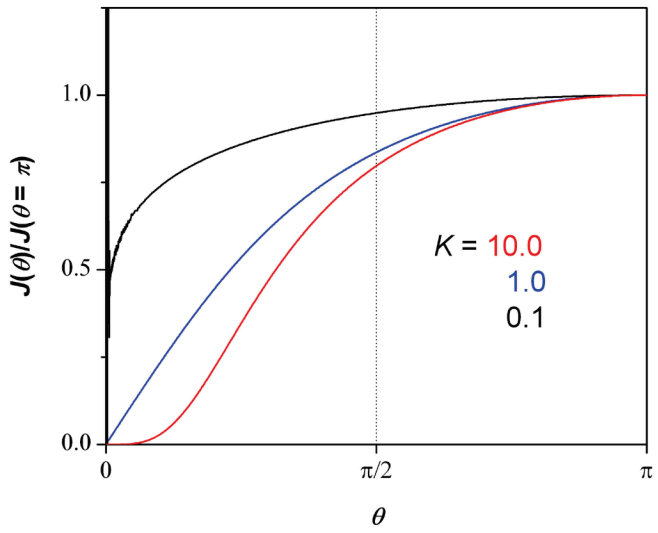

Figure 3-6. Simulated flux at the sidewall of an individual SWNT in the normalized form.

When electron transfer is diffusion limited (K = 10) or close to diffusion limitation (K = 1), mediator regeneration occurs non-uniformly at the sidewall. In these cases, original mediators are efficiently regenerated at the top half of the sidewall that is exposed to the solution, thereby yielding $J(\theta \geq \pi/2)/J(\theta = \pi) > 0.70$. At the same time, much smaller flux is obtained at the bottom half of the sidewall ($\theta < \pi/2$), where access of redox molecules is blocked by the underlying insulating substrate. On the other hand, flux distribution is much more uniform with $K = 0.1$. $J(\theta)/J(\theta = \pi) > 0.50$ is achieved even at very small θ of 0.01π. This apparently uniform accessibility is due to slow mediator regeneration at the top half of the sidewall. The tip-generated species that are not consumed immediately at the top half can access to the bottom half. Overall, eq 2 is a good approximation when mediator regeneration at the SWNT is kinetically limited. In this case, eq 2 is obtained from eq 4 using $c(\theta) \approx c_{SWNT}$ and $J(\theta) = i_{SWNT}/nFA$. The extremely large k_{et} value of ~1,000 cm/s required for a diffusion limitation suggests that mediator regeneration at the SWNT is kinetically limited.

ACKNOWLEDGEMENTS

This work was supported by grants from the National Institutes of Health (GM073439), and the Petersen Institute of NanoScience and Engineering at the University of Pittsburgh. The authors thank the Department of Materials Science and Engineering for the provision of access to the SEM instrumentation.

References

(1) McCreery, R. L. *Chem. Rev.* **2008**, *108*, 2646–2687.

(2) Dumitrescu, I.; Unwin, P. R.; Macpherson, J. V. *Chem. Commun.* **2009**, 6886–6901.

(3) Heller, I.; Kong, J.; Heering, H. A.; Williams, K. A.; Lemay, S. G.; Dekker, C. *Nano Lett.* **2005**, *5*, 137–142.

(4) Fan, Y. W.; Goldsmith, B. R.; Collins, P. G. *Nat. Mater.* **2005**, *4*, 906–911.

(5) Goldsmith, B. R.; Coroneus, J. G.; Khalap, V. R.; Kane, A. A.; Weiss, G. A.; Collins, P. G. *Science* **2007**, *315*, 77–81.

(6) Xu, W.; Shen, H.; Kim, Y. J.; Zhou, X.; Liu, G.; Park, J.; Chen, P. *Nano Lett*. **2009**, *9*, 3968–3973.

(7) Bard, A. J.; Mirkin, M. V., Eds. *Scanning Electrochemical Microscopy*; Marcel Dekker: New York, 2001.

(8) Amemiya, S.; Bard, A. J.; Fan, F.-R. F.; Mirkin, M. V.; Unwin, P. R. *Ann. Rev. Anal. Chem.* **2008**, *1*, 95–131.

(9) Xiong, H.; Gross, D. A.; Guo, J.; Amemiya, S. *Anal. Chem.* **2006**, *78*, 1946–1957.

(10) Xiong, H.; Kim, J.; Kim, E.; Amemiya, S. *J. Electroanal. Chem.* **2009**, *629*, 78–86.

(11) Kim, E.; Kim, J.; Amemiya, S. *Anal. Chem.* **2009**, *81*, 4788–4791.

(12) Wilson, N. R.; Guille, M.; Dumitrescu, I.; Fernandez, V. R.; Rudd, N. C.; Williams, C. G.; Unwin, P. R.; Macpherson, J. V. *Anal. Chem.* **2006**, 7006–7015.

(13) Fabre, B.; Hauquier, F.; Herrier, C.; Pastorin, G.; Wu, W.; Bianco, A.; Prato, M.; Hapiot, P.; Zigah, D.; Prasciolu, M.; Vaccari, L. *Langmuir* **2008**, *24*, 6595–6602.

(14) Reina, A.; Hofmann, M.; Zhu, D.; Kong, J. *J. Phys. Chem. C* **2007**, *111*, 7292–7297.

(15) Shao, Y.; Mirkin, M. V. *J. Phys. Chem. B* **1998**, *102*, 9915–9921.

(16) Xiong, H.; Guo, J.; Amemiya, S. *Anal. Chem.* **2007**, *79*, 2735–2744.

(17) Dumitrescu, I.; Unwin, P. R.; Wilson, N. R.; Macpherson, J. V. *Anal. Chem.* **2008**, *80*, 3598–3605.

(18) Shao, Y.; Mirkin, M. V. *J. Phys. Chem. B* **1998**, *102*, 9915–9921.

(19) Amemiya, S.; Bard, A. J. *Anal. Chem.* **2000**, *72*, 4940–4948.

(20) Wilson, N. R.; Guille, M.; Dumitrescu, I.; Fernandez, V. R.; Rudd, N. C.; Williams, C. G.; Unwin, P. R.; Macpherson, J. V. *Anal. Chem.* **2006**, *78*, 7006–7015.

(21) Xiong, H.; Gross, D. A.; Guo, J.; Amemiya, S. *Anal. Chem.* **2006**, *78*, 1946–1957.

4. Quantitative Imaging of Ion Transport at Single Nanopores by High-Resolution Scanning Electrochemical Microscopy

This work has been published as M. Shen, R. Ishimatsu, J. Kim, S. Amemiya, Quantitative Imaging of Ion Transport at Single Nanopores by High-Resolution Scanning Electrochemical Microscopy, *J. Am. Chem. Soc.*, **2012**,134, 9856-9859.

4.1 Introduction

Here, we report on the unprecedentedly high-resolution imaging of ion transport at single nanopores by scanning electrochemical microscopy (SECM). The quantitative SECM image of single nanopores allows for the determination of their structural properties including their density, shape, and sizes, which is essential for the understanding of the permeability of the whole nanoporous membrane. The nanoscale spatial resolution of SECM was demonstrated by scanning a 15 nm-radius nanopipet tip at ~5 nm distance from a highly porous silicon membrane to obtain the peak current response controlled by the diffusional transport of tetrabutylammonium from a nanopore to the pipet-supported nanoscale liquid/liquid interface. A 240 nm × 500 nm image resolved 15 nanopores, which corresponds to a high effective density of 88 pores/μm^2. The finite element simulation of the SECM image was performed to overcome the limit in spatial resolution set by the tip size, thereby yielding major and minor axes of 21–66 nm for ellipse-shaped nanopores in addition to a pore length of 30 nm. These structural parameters

are consistent with those determined by TEM, which confirms the reliability of quantitative SECM imaging on the nanoscale.

The development and application of nanoporous membranes for nanofiltration,[1] biomedical devices,[2] nanofluidics[3] and biomimetic membrane transport[4] require the quantitative understanding of membrane permeability at single nanopore levels. In fact, it has been demonstrated both theoretically and experimentally that the permeability of the whole nanoporous membrane depends on the convolution of several structural properties of nanopores including their density, shape, and dimensions, i.e., diameter and length for cylindrical nanopores.[5] Here, we apply scanning electrochemical microscopy[6] (SECM) to quantitatively and separately determine these key structural parameters from the high-resolution image of ion transport at single nanopores. Noticeably, the nanoscale spatial resolution of SECM achieved in this study is the highest reported so far excpt in one study,[7] where rather unusual experimental conditions were employed without quantitative image analysis.

The unprecedentedly high spatial resolution of SECM is required for imaging the single nanopores of a highly porous silicon membrane[8] with ~10^2 pores/μm^2 (Figure 4-1A). This pore density is 10^2–10^6 times higher than that of the nanopore membranes (mainly track-etched polymer membranes) that were used for the electrochemical imaging of single pores by SECM,[9] scanning ion-conductance microscopy (SICM),[10] SECM-SICM,[11] and SECM-AFM.[12] Single-nanopore imaging has not been reported for this emerging class of highly permeable silicon membranes with high pore density and molecular thickness (30 nm in this study), which found important applications in the efficient separation of macromolecules[8a-c] and nanoparticles,[8d] and also in the facilitation of tissue engineering and cell culture.[8e] Importantly, the ultrathin and highly porous silicon nanopore membrane is robust enough to be self-standing in the aqueous

solution as demonstrated in our SECM studies of several thousands of silicon nanopores using micrometer-sized tips.[5b,5c]

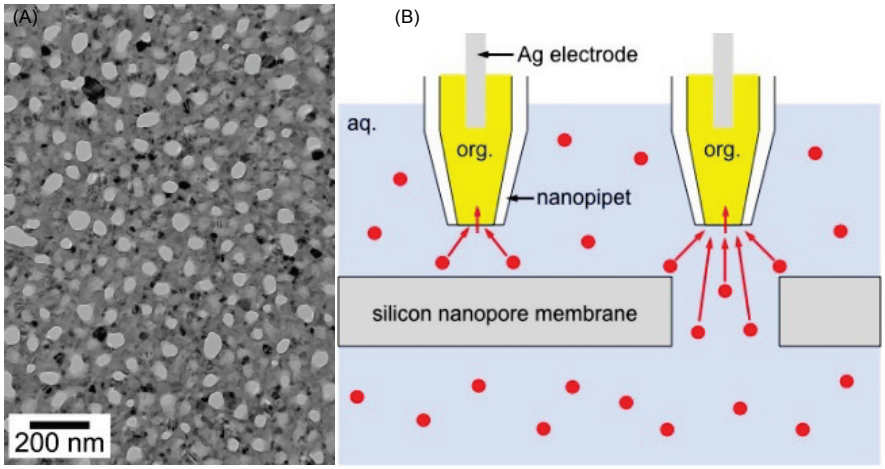

Figure 4-1. (A) TEM image of a silicon nanopore membrane and (B) scheme of SECM imaging with a nanopipet-supported ITIES tip over the impermeable (left) and nanoporous (right) regions of the membrane.

In this work, a nanoscale resolution is achieved by scanning a small SECM tip with 15 nm in radius at exceptionally short distances of 5–7 nm from a silicon nanopore membrane. In the nanoscale SECM imaging, the current response at the nanotip is based on diffusion-controlled ion transfer at the interface between two immiscible electrolyte solutions (ITIES), which is supported at the tip of the glass nanopipet filled with an organic electrolyte solution[13] (Figure 4-1B). The ionic tip current is suppressed when the tip is positioned within a tip diameter from the impermeable surface of the silicon membrane, which hinders ion diffusion to the nanoscale ITIES tip, i.e., negative feedback effect.[6] On the other hand, the tip current increases as the tip is laterally scanned over a nanopore, where ions in or behind the nanopore can diffuse to the ITIES

tip. The image contrast based on the difference in the tip current over impermeable and nanoporous regions is enhanced at a shorter tip–membrane distance. We maintain extremely short distances of 5–7 nm in the constant-height mode of SECM[6] without any distance control during ~10 min-long imaging simply by suppressing the thermal expansion and contraction of an SECM stage in the recently developed isothermal chamber with a temperaure stability of 0.2 mK/min.[13]

4.2 Results and Discussion

4.2.1 The Characterization of Nanopipet Supported ITIES tip

A nanopipet-based SECM tip was prepared as reported elsewhere[13] and characterized by ion-transfer voltammetry and SEM to determine the inner and outr radii (a and r_g, respectively) of the disk-shaped tip, which are required for the quantitative analysis of an SECM image. A nanopipet was filled with the 1,2-dichloroethane solution of organic supporting electrolytes and immersed in the aqueous solution of tetrabuthylammonium (TBA) to voltammetrically drive TBA transfer across the tip-supported nanoscale ITIES (Figure 3-2A). The sigmoidal steady-state voltammogram reaches to a limiting current, $i_{T,\infty}$, of 61 pA, which corresponds to a = 15 nm with a typical RG value of 1.5 as determined from

$$i_{T,\infty} = 4xnFDc^{*}a \qquad (1)$$

where x is a function of RG,[14] n is the number of transferred charges (= +1) in the tip reaction, and D (= 8.8 × 10^{-6} cm^2/s) and c^* are the diffusion coefficient and concentration of the transferred ion in the bulk solution. These inner and outer radii agree well with those of a typical nanopipet as estimated by SEM (Figure 4-2B).

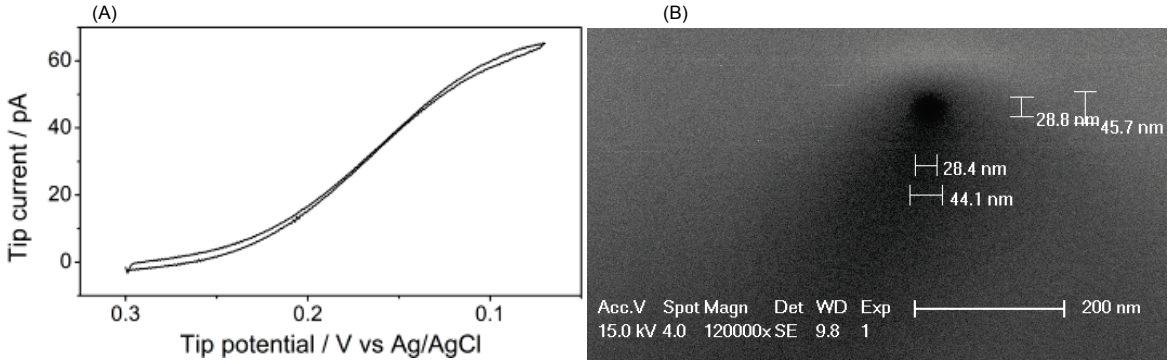

Figure 4-2. (A) Cyclic voltammetry of 10 mM TBA in 0.3 M KCl at 50 mV/s. (B) SEM image of the tip opening of a typical nanopipet.

The nanopipet-supported ITIES tip thus characterized was employed for the conatsnt-height imaging of a silicon nanopore membrane to resolve 15 nanopores as high-current regions in the 240 nm × 500 nm image (Figure 4-3A). In this image, 7 pores (**4**, **6**, **7**, **10**, **11**, **12**, and **14**) are completely observed while the other 8 pores are only half seen. Effectively, there are 11 pores in the image to yield a high density of 88 pores/μm^2 as expected from the TEM image (Figure 4-1A). In this analysis, we assumed that pores **6** and **7** are independent to give two peaks with different heights, indicating that pore **6** is larger than pore **7**. We, however, can not exclude the

possibility that these two pores are connected to each other at the overlapping region of their images. In fact, the area that is covered by a nanopore in the SECM image is elongated, which is consistent with the distorted shapes of nanopores in the TEM image of the nanopore membrane (Figure 4-1A). On the other hand, the apparent area of a nanopore in the image is larger than its real size approximately by the tip diameter, which limits spatial resolution. This limitation can be overcome by employing numerical simulation to more accurately determine pore sizes (see below).

4.2.2 SECM imaging of highly porous nanocrystalline silicon membrane in a constant height mode

The whole procedure for SECM imaging in Figure 4-3A is illustrated in Figure 4-3B using the corresponding time profile of the current response at the nanopipet-supported ITIES tip, which also confirms short and stable tip–membrane distances. Prior to imaging, the tip was brought in close proximity to the nanopore membrane until the tip current decreased to 70 % of $i_{T,\infty}$ at ~100s. In this example, the tip approached to a nanopore as seen at (x, y) = (0, 0) in the SECM image (Figure 4-3A). While the tip stayed over the pore for ~80 s, the nearly constant tip current indicates a stable distance between tip and pore. Then, the tip was scaned from x = 0 nm to x =240 nm with a step size of 4 nm, which was repeated from y = 0 nm to y = 500 nm with an interval of 5 nm. During the 240 nm × 500 nm scan, the height of a peak current response varied not only with the size of a pore under the tip but also with a separation between tip and pore, thereby yielding a family of peaks with various heights as assigned to each nanopore in Figure 4-3B. In contrast, the very stable and reproducible current responses that are suppressed by the

negative feedback effect from the impermeable membrane surface were obserbed between peaks, indicating that the tip–membrane distance was nearly constant during imaging. Negative feedback tip currents, i_T, of 30–35 pA in Figure 4-3B correspond to tip–membrane distances, d, of 5–7 nm in the approximate equation as given by[13]

$$d / a = \left(2.35 \times 10^{-2}\right) \exp\left(6.99 i_T / i_{T,\infty}\right) - \left(3.5 \times 10^{-5}\right) \exp\left(13.3 \sqrt{i_T / i_{T,\infty}}\right) \qquad (2)$$

where RG = 1.5 was employed. Eventually, imaging was completed at 818 s when the tip was stopped near pore **15**. Then, the tip drifted laterally toward the pore, which is seen as a higher tip current at 850–940 s. Finally, the tip current recovered to the initial $i_{T,\infty}$ value when the tip was withdrawn to 1.5 μm away from the substrate, indicating the good stability of the tip current.

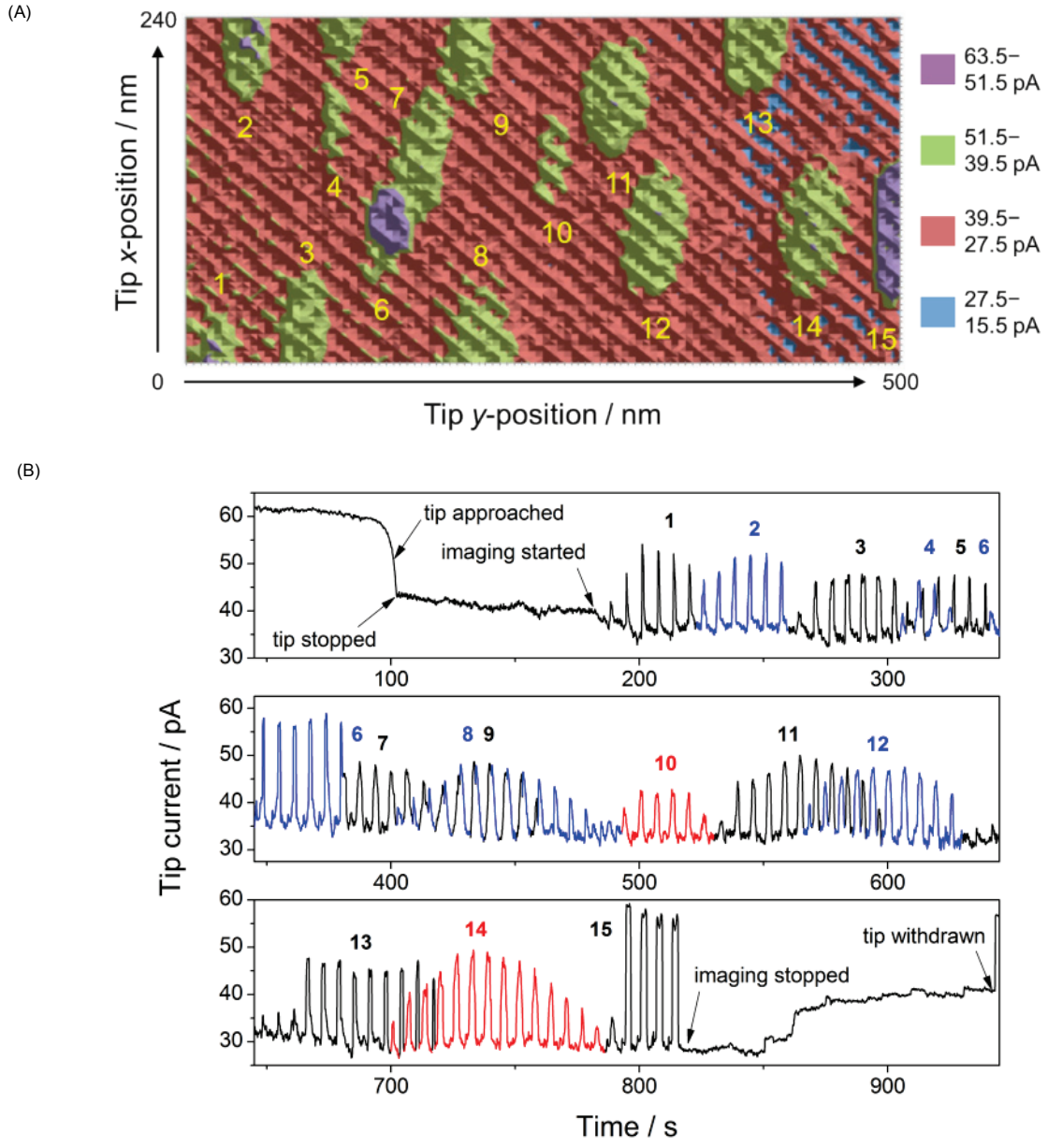

Figure 4-3. (A) SECM image of a silicon nanopore membrane and (B) current versus time profile during the whole imaging procedure.

4.2.3 Quantitative analysis of SECM image by Finite Element Simulation.

We examined SECM line scans over nanopores **10** and **14** (red lines in Figure 4-3B) to determine their actual sizes without the limitation of spatial resolution by employing the finite element simulation of ion diffusion around the tip and the nanopore (see Supporting Information). For simplicity, the cross section of a pore perpendicular to its length was assumed to be an ellipse, thereby yielding major and minor axes and length as structural parameters. Panels A and B of Figure 4-4 show very good fits of simulation results with experimental results of pores **10** and **14**, respectively, where each peak current response in a x line scan was plotted against the x position of the center of the tip with respect to the center of the nanopore, i.e., Δx, while the relative y position was given by Δy (see also Figure 4-6 for these definitions). The simulation results show that pore **10** corresponds to an ellipse with 42 nm- and 21 nm-long major and minor axes in the x, y-directions, respectively, while ellipse-shaped pore **14** gives 66 nm- and 36 nm-long axes for the respective directions. The area of average-sized pore **14** is 1.87×10^3 nm^2 so that an effective pore density of 88 pores/μm^2 (see above) corresponds to a porosity of 16.4 %. This high porosity is consistent with a porosity of ~15 % as estimated from the TEM image (Figure 4-1A), thereby supporting the reliability of these structural parameters determined by high-resolution SECM.

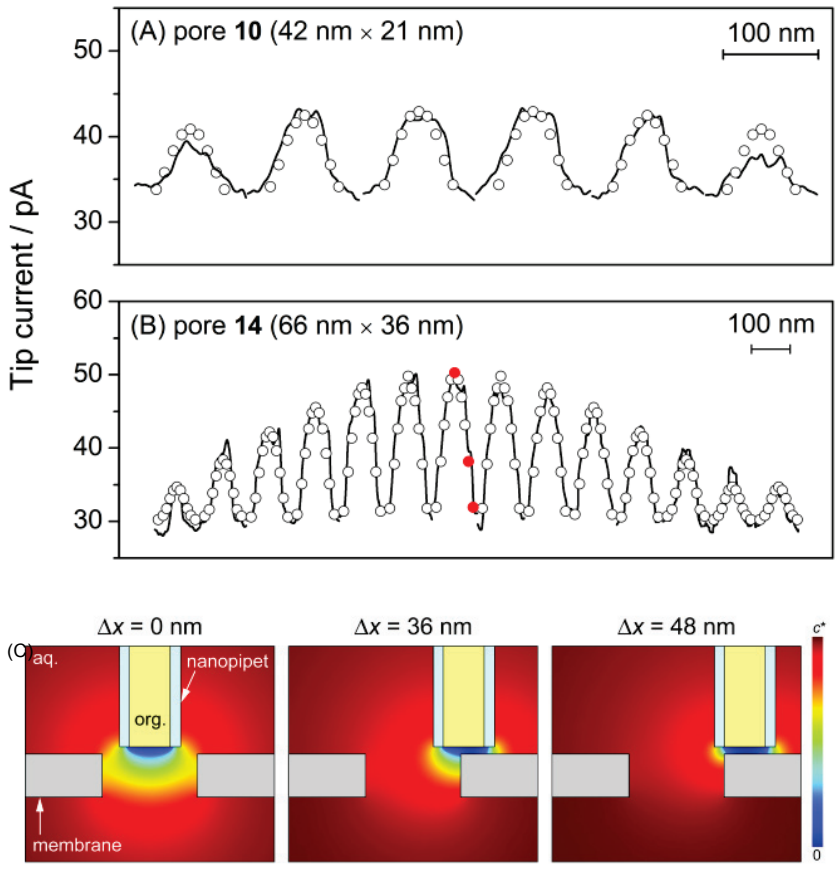

Figure 4-4. Simulated tip current (open and closed circles) over pores (A) 10 and (B) 14 at Δx = (A and B) 0, ±9, ±18, ±27, ±36, and (B) ±48 nm as fitted with experimental line scans (solid lines). The tip position in the *y*-direction was changed at every 5 nm from Δy = (A) –30 and (B) –12.5 nm from the leftmost peak. The tip positions indicated by closed red circles in (B) were used to calculate sliced concentration profiles in (C).

The numerical simulation of line scans in Figurs 4-4A and B clearly show that the actual major axes of ellipse-shaped nanopores **10** and **14** are smaller than the width of a peak at its base (~72 and ~96 nm, respectiely), where the difference is very close to the tip diameter. This limitation in spatial resolution set by the tip size is obvious in the simulated spatial distribution of the

concentration of the transfrred ion (Figure 4-4C for pore **14**). The simulation result shows that the tip current is controlled by negative feedback effect when the whole tip surface is positioned above the impermeable region of the membrane (e.g., Δx = 48 nm in Figure 4-4C). Subsequently, the edge of the base of a peak current response is further from the real periphery of a nanopore (Δx = 33 nm) by a tip radius of 15 nm, thereby broadening the base of the current peak by tip diameter in comparison to the real pore size. In fact, ion diffusion from the nanopore to the pore-side of the tip is still significant when the center of the tip is positioned just outside of the pore periphery (Δx = 36 nm). At this tip position, the correponding tip current decreases only to the half of the peak current that is obtained when the tip center is positioned above the pore center (Δx = 0 nm). Noticeably, the diffusion layer at the tip at Δx = 0 develops through the nanopore so that the resulting tip current is sensitive to the pore length (Figure 4-7), which can be determined from the high-resolution SECM image of a single nanopore.

4.3 Conclusions

In sumamry, nanoscale SECM was successfully applied to enable the unprecedentedly high-resolution imaging of single nanopores in a highly porous silicon membrane. The high resolution is due to a small tip radius of 15 nm and short and stable tip–membrane distances of 5–7 nm. The resulting image can be quantitatively analyzed to determine the structural properties of a nanopore without the limitation of spatial resolution set by the tip size, which is comparable to the pore sizes. The smallest pore size of ~21 nm thus determined is ~5 times smaller than that of the smallest nanopore[12b] imaged so far by SECM, SICM, or their combined techniques, where pore sizes were determined not by quantitative image analysis but by SEM. The highest

resolution of SECM under usual experimental conditions was achieved in this study by employing the simple constant-height mode without feedback distance control not only because the nanopore membrane surface was flat but also because the SECM stage was isolated from ambient environment using an isothermal chamber to suppress thermal drift.[13] The further application of this simple, quantitative, and high-resolutsion SECM approach to the imaging of biological nanopores[15] is envisoned.

4.4 Supporting Information

4.4.1 Chemicals. Tetradodecylammonium (TDDA) bromide, tetrabutylammonium chloride (TBACl), 1,2-dichloroethane, potassium chloride, and *N*-dimethyltrimethyl silylamine were purchased from Sigma-Aldrich (Saint Louis, MO). Potassium tetrakis(pentafluorophenyl)borate (TFAB) was obtained from Boulder Scientific Company (Mead, CO). Isopropyl alcohol from J. T. Baker (Phillipsburg, NJ). All reagents were used as received. The TFAB salt of TDDA was prepared by metathesis.[16] 10 mM TBACl was dissolved in 18.3 MΩ cm deionized water (Nanopure, Barnstead, Dubuque, IA) with 0.3 M KCl. The resulting solution was passed through a 0.2 μm filter (Fisher Scientific, Hanover Park, IL) before its use for SECM imaging.

4.4.2 SEM of Nanopipets. A nanopipet was pulled [17] as reported elsewhere and coated with a thin Pd film by a high-resolution sputter coater (Cressington 208HR, Ted Pella, Redding, CA) at a working distance of 4 cm with 20 mA for 5 s. The orifice of a Pd-coated nanopipet was observed by field-emission SEM (model XL-30, Philips Electron Optics, Eindhoven, Netherlands) under 15 kV electron beam.

4.4.3 Membrane Characterization and Pretreatment. A pnc-Si membrane (US100-P30Q33, TEMwindows, West Henrietta, NY) was characterized and cleaned as follow. The distribution of pore

diameter was determined from the TEM image of a nanomembrane (Figure 1A). The pore diameter is the average of major and minor axes obtained by fitting every pore as an ellipse as reported elsewhere.[18] For cleaning, the membrane was soaked in a piranha solution (1:1 volume ratio sulfuric acid: hydrogen peroxide) for 4–6 min, in water for 4–11 min, and then in isopropyl alcohol for 3 min. The cleaned membrane was placed into the electrochemical cell filled with water, which was replaced with 24 ml of 10 mM TBACl in 0.3 M KCl. The position of the membrane was fixed by screwing two glass slides from opposite sides onto the membrane.

4.4.4 SECM Imaging. The setup of our SECM system is detailed elsewhere.[17] Briefly, a home-built SECM stage was used for tip positioning while the potentiostat of CHI 900 (CH Instruments, Austin, TX) was used for recording the tip current in a two electrode cell with Ag/AgCl and Pt electrodes in outer aqueous and inner organic phases, respectively. The *x*, *y*, and *z*-positions of a nanopipet tip were roughly controlled using the micrometers (SM-25 for *z*-axis and AJS100-1 for *x*, *y*-axes, Newport, Irvine, CA) of the SECM stage (M-462, Newport), which is also equipped with piezoelectric positioners with closed-loop capacitive sensors for nanoscale tip positioning. Specifically, a *z*-axis positioner, P-621.ZCD, was controlled by E-665CR while two E-625.CR controllers were employed for *x*, *y*-axis positioners, P-620.2CD, where all positioners and controllers are from PI (Auburn, MA). A Labview program was written to control the positioners in the drift compensation mode, which eliminates drift in the digital-analog converters on the main board of the controllers. The microscope stage was accommodated in an isothermal chamber,[17] which was placed in a faraday cage on a vibration isolation table (63-533, TMC, Peabody, MA).

As far as we imaged the small area of a pnc-Si membrane using a sharp tip with small *RG*, there was no significant change in the tip–substrate distance or the tip–substrate contact, which can be caused by their imperfect alignment. As schematically shown in Figure 4-5A, we were able to achieve a sufficiently parallel alignment between the substrate surface and the tip surface simply using a bubble level because (i) dimensions of 280 nm × 500 nm for the whole SECM image in Figure 3A are only ~8 and ~15 times larger than an inner tip diameter of 34 nm and (ii) the sharp tip has a small *RG* value of 1.4. Noticeably, the parallel alignment required for constant-height imaging in this work is very similar to the parallel alignment required for perpendicularly approaching a typical SECM nanotip with a large *RG* value of ~10 near the substrate surface without contact (Figure 4-5B), which was also achieved using a bubble level.[19]

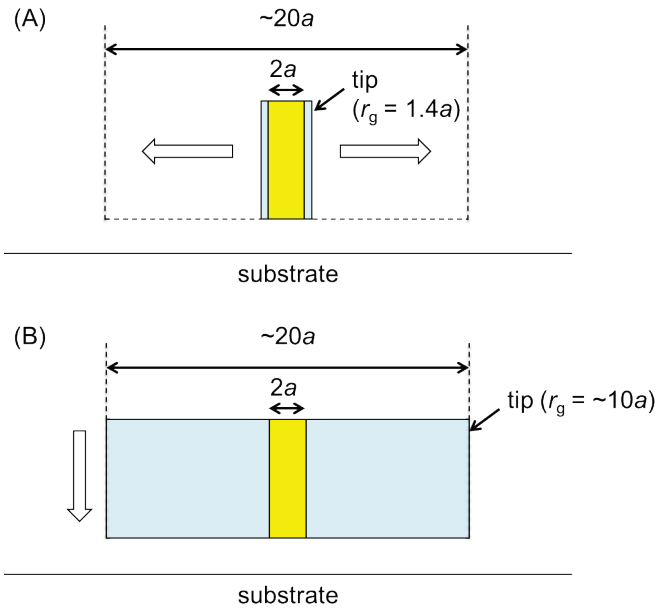

Figure 4-5. Parallel alignment between the tip surface and the substrate surface required for (A) imaging a small area using a sharp tip with *RG* = 1.4 and (B) positioning a typical tip with *RG* = ~10 near the substrate surface.

Prior to imaging, the tip was brought in close proximity to a nanopore membrane at (x, y) = (0, 0) using the feedback mode of SECM, and held at a constant height from the membrane surface. Then, the tip was scanned in x-direction with a step size of 4 nm in 70 steps, thereby resulting in a travel distance of 280 nm (Figure 4-6). After each line scan, the x-position of the tip was returned to 0 nm and its y position was shifted by 5 nm, which was followed by the next line scan from x = 0 nm to x = 280 nm. The line scan in x-direction was repeated from y = 0 nm to y = 500 nm at every 5 nm for 100 steps. Overall, it took ~12 minutes (Figure 3B) to obtain the 280 nm × 500 nm image with 71 × 101 data points.

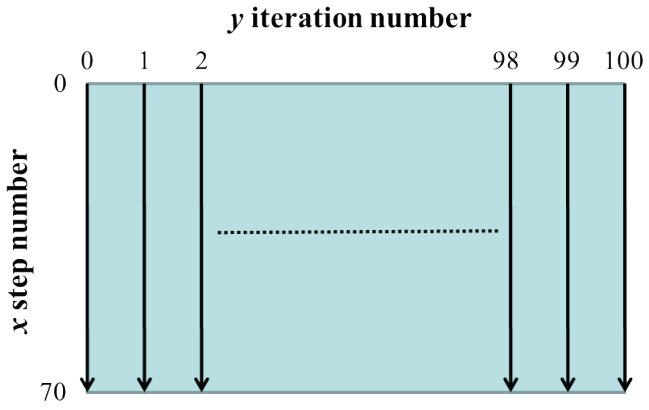

Figure 4-6. Scheme of lateral scanning directions.

4.4.5 Finite Element Simulation. The simulation report generated by COMSOL Multiphysics finite element package (version 3.5a, COMSOL, Inc., Burlington, MA) is attached. In this simulation, an SECM diffusion problem with a disk-shaped tip over a nanopore as an elliptic cylinder is defined in Cartesian coordinates (Figure 4-7). The origin of the coordinate axes is set at the center of the upper orifice of the nanopore. Initially, the solution phase contains a target ion at a bulk concentration of c^*. The diffusion of the target ion in the solution phase is defined by

$$\frac{\partial c}{\partial t} = D\left(\frac{\partial^2 c}{\partial x^2} + \frac{\partial^2 c}{\partial y^2} + \frac{\partial^2 c}{\partial z^2}\right) \tag{3}$$

where c is the ion concentration at (x, y, z). Ion diffusion in the inner organic solution does not affect the tip current, which is limited by the diffusion of the traget ion in the outer aqueous solution. Accordingly, the zero ion concentration is used as the electrode surface boundary condition (red lines in Figure 4-7). The membrane surface and pore wall are impermeable to an ion, which corresponds to zero flux perpendicluar to these boundaries (black bold lines). Boundary conditions at simulation space limits are given by the bulk concentration of the ion, c^* (blue lines). The simulation space is large enough to affect the simulated tip current less than 1.5 %.

Specifically, eq 3 was solved using the approximate size of a nanopore, which is smaller by the tip diameter than the corresponding size in an SECM image (see main text). Then, pore size in the simulation was adjusted until experimental line scans in the image fit with simulation results (Figure 4A).

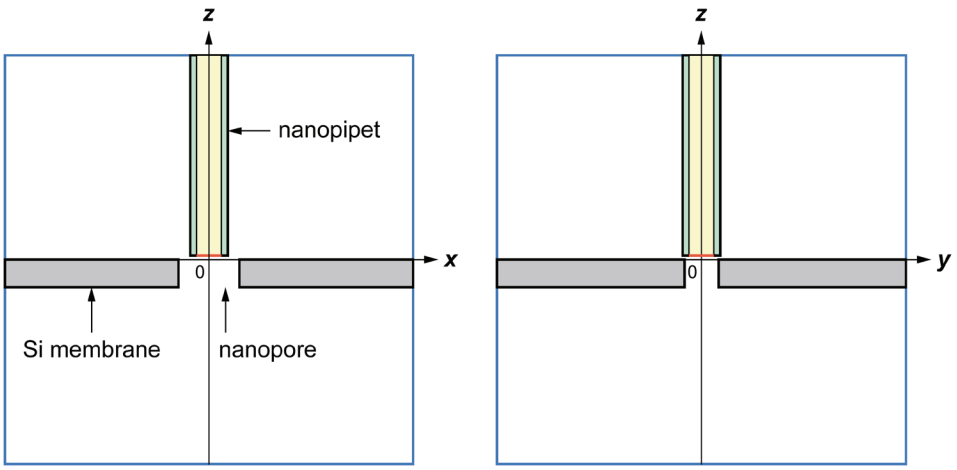

Figure 4-7. Scheme of cross sections of simulation space at $y = 0$ (left) and $x = 0$ (right).

4.4.6 Effect of Pore Depth on Tip Current. The x-line scans over pore **7** at $\Delta y = 0$ were simulated using different pore depths (Figure 4-8) to confirm its unique depth of 30 nm.

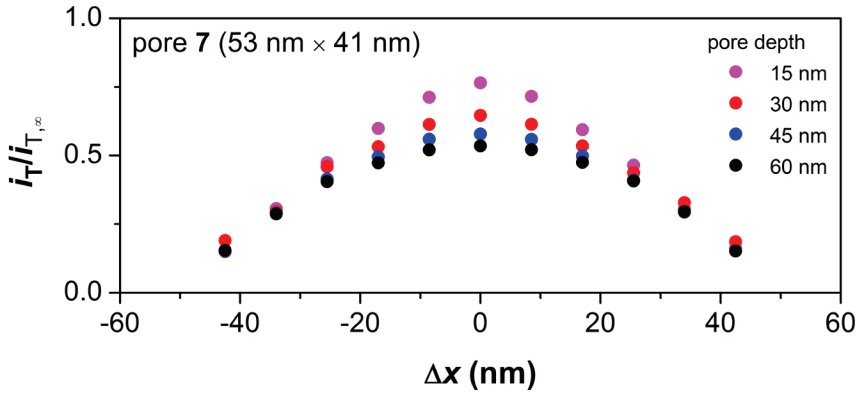

Figure 4-8. Effect of pore depth on simulated current responses in x-line scans over pore **7** at $\Delta y = 0$ nm. See the legend of Figure 4 for other parameters.

ACKNOWLEDGMENTS

This work was supported by grants from the National Institutes of Health (GM073439). We thank Dr. Christopher C. Striemer and Mr. Charles Chan, SiMPore, for the TEM images of silicon nanopore membranes and their analysis.

References

(1) (a) Vandezande, P.; Gevers, L. E. M.; Vankelecom, I. F. J. *Chem. Soc. Rev.* **2008**, *37*, 365. (b) Shannon, M. A.; Bohn, P. W.; Elimelech, M.; Georgiadis, J. G.; Marinas, B. J.; Mayes, A. M. *Nature* **2008**, *452*, 301. (c) Peng, X. S.; Jin, J.; Nakamura, Y.; Ohno, T.; Ichinose, I. *Nat. Nanotechnol.* **2009**, *4*, 353. (d) Karan, S.; Samitsu, S.; Peng, X.; Kurashima, K.; Ichinose, I. *Science* **2012**, *335*, 444.

(2) (a) Kooman, J. P.; van der Sande, F. M.; Leunissen, K. M. L. *Blood Purification* **2007**, *25*, 377. (b) Fissell, W. H.; Dubnisheva, A.; Eldridge, A. N.; Fleischman, A. J.; Zydney, A. L.; Roy, S. *J. Membr. Sci.* **2009**, *326*, 58. (c) Perin, L.; Da Sacco, S.; De Filippo, R. E. *Adv. Drug Deliv. Rev.* **2011**, *63*, 379.

(3) (a) van den Berg, A.; Wessling, M. *Nature* **2007**, *445*, 726. (b) Schoch, R. B.; Han, J. Y.; Renaud, P. *Rev. Mod. Phys.* **2008**, *80*, 839. (c) Li, Y.-Q.; Zheng, Y.-B.; Zare, R. N. *ACS Nano* **2012**, *6*, 993.

(4) (a) Jovanovic-Talisman, T.; Tetenbaum-Novatt, J.; McKenney, A. S.; Zilman, A.; Peters, R.; Rout, M. P.; Chait, B. T. *Nature* **2009**, *457*, 1023. (b) Kowalczyk, S. W.; Kapinos, L.; Blosser, T. R.; Magalhaes, T.; van Nies, P.; Lim, R. Y. H.; Dekker, C. *Nat. Nanotechnol.* **2011**, *6*, 433.

(5) (a) Berg, H. C. *Random Walks in Biology*; Princeton University Press: Princeton, NJ, 1993. (b) Kim, E.; Xiong, H.; Striemer, C. C.; Fang, D. Z.; Fauchet, P. M.; McGrath, J. L.; Amemiya, S. *J. Am. Chem. Soc.* **2008**, *130*, 4230. (c) Ishimatsu, R.; Kim, J.; Jing, P.;

Striemer, C. C.; Fang, D. Z.; Fauchet, P. M.; McGrath, J. L.; Amemiya, S. *Anal. Chem.* **2010**, *82*, 7127.

(6) (a) *Scanning Electrochemical Microscopy*; Bard, A. J.; Mirkin, M. V., Eds.; Marcel Dekker: New York, 2001. (b) Amemiya, S.; Bard, A. J.; Fan, F.-R. F.; Mirkin, M. V.; Unwin, P. R. *Ann. Rev. Anal. Chem.* **2008**, *1*, 95.

(7) Fan, F.-R. F.; Bard, A. J. *Proc. Natl. Acad. Soci. U.S.A.* **1999**, *96*, 14222.

(8) (a) Striemer, C. C.; Gaborski, T. R.; McGrath, J. L.; Fauchet, P. M. *Nature* **2007**, *445*, 749. (b) Fang, D. Z.; Striemer, C. C.; Gaborski, T. R.; McGrath, J. L.; Fauchet, P. M. *Nano Lett.* **2010**, *10*, 3904. (c) Snyder, J. L.; Clark, A.; Fang, D. Z.; Gaborski, T. R.; Striemer, C. C.; Fauchet, P. M.; McGrath, J. L. *J. Membrane Sci.* **2011**, *369*, 119. (d) Gaborski, T. R.; Snyder, J. L.; Striemer, C. C.; Fang, D. Z.; Hoffman, M.; Fauchet, P. M.; McGrath, J. L. *ACS Nano* **2010**, *4*, 6973. (e) Agrawal, A. A.; Nehilla, B. J.; Reisig, K. V.; Gaborski, T. R.; Fang, D. Z.; Striemer, C. C.; Fauchet, P. M.; McGrath, J. L. *Biomaterials* **2010**, *31*, 5408.

(9) (a) Bath, B. D.; White, H. S.; Scott, E. R. In Scanning Electrochemical Microscopy; Bard, A. J., Mirkin, M. V., Eds.; Marcel Dekker: New York, 2001, p 343. (b) Uitto, O. D.; White, H. S. *Anal. Chem.* **2001**, *73*, 533. (c) Uitto, O. D.; White, H. S.; Aoki, K. *Anal. Chem.* **2002**, *74*, 4577. (d) Lee, S.; Zhang, Y.; White, H. S.; Harrell, C. C.; Martin, C. R. *Anal. Chem.* **2004**, *76*, 6108. (e) Ervin, E. N.; White, H. S.; Baker, L. A. *Anal. Chem.* **2005**, *77*, 5564. (f) Ervin, E. N.; White, H. S.; Baker, L. A.; Martin, C. R. *Anal. Chem.* **2006**, *78*, 6535. (g) White, R. J.; White, H. S. *Anal. Chem.* **2007**, *79*, 6334. (h) McKelvey, K.; Snowden, M. E.; Peruffo, M.; Unwin, P. R. *Anal. Chem.* **2011**, *83*, 6447.

(10) (a) Proksch, R.; Lal, R.; Hansma, P. K.; Morse, D.; Stucky, G. *Biophys. J.* **1996**, *71*, 2155. (b) Böcker, M.; Muschter, S.; Schmitt, E. K.; Steinem, C.; Schäffer, T. E. *Langmuir* **2009**, *25*, 3022. (c) Chen, C.-C.; Derylo, M. A.; Baker, L. A. *Anal. Chem.* **2009**, *81*, 4742. (d) Chen, C.-C.; Baker, L. A. *Analyst* **2011**, *136*. (e) Chen, C.-C.; Zhou, Y.; Baker, L. A. *ACS Nano* **2011**, *5*, 8404. (f) Zhou, Y.; Chen, C.-C.; Baker, L. A. *Anal. Chem.* **2012**, *84*, ASAP.

(11) Takahashi, Y.; Shevchuk, A. I.; Novak, P.; Zhang, Y.; Ebejer, N.; Macpherson, J. V.; Unwin, P. R.; Pollard, A. J.; Roy, D.; Clifford, C. A.; Shiku, H.; Matsue, T.; Klenerman, D.; Korchev, Y. E. *Angew. Chem. Int. Ed.* **2011**, *50*, 9638.

(12) (a) Macpherson, J. V.; Unwin, P. R. *Anal. Chem.* **2000**, *72*, 276. (b) Macpherson, J. V.; Jones, C. E.; Barker, A. L.; Unwin, P. R. *Anal. Chem.* **2002**, *74*, 1841. (c) Gardner, C. E.; Unwin, P. R.; Macpherson, J. V. *Electrochem. Comm.* **2005**, *7*, 612.

(13) Kim, J.; Shen, M.; Nioradze, N.; Amemiya, S. *Anal. Chem.* submitted.

(14) Lefrou, C. *J. Electroanal. Chem.* **2006**, 592, 103.

(15) Guo, J.; Amemiya, S. *Anal. Chem.* **2005**, *77*, 2147.

(16) Guo, J.; Amemiya, S. *Anal. Chem.* **2006**, *78*, 6893.

(17) Kim, J.; Shen, M.; Nioradze, N.; Amemiya, S. *Anal. Chem.* **2012**, *84*, 3489.

(18) Kim, E.; Xiong, H.; Striemer, C. C.; Fang, D. Z.; Fauchet, P. M.; McGrath, J. L.; Amemiya, S. *J. Am. Chem. Soc.* **2008**, *130*, 4230.

(19) Sun, P.; Mirkin, M. V. *Anal. Chem.* **2006**, *78*, 6526.

B. Development of Nanoscale Scanning Electrochemical Microscopy

5. Stabilizing Nanometer Scale Tip-to-Substrate Gaps in Scanning Electrochemical Microscopy Using Isothermal Chamber for Thermal Drift Suppression

This work has been published as J. Kim, M. Shen, N. Nioradze, S. Amemiya, Stabilizing Nanometer Scale Tip-to-Substrate Gaps in Scanning Electrochemical Microscopy Using an Isothermal Chamber for Thermal Drift Suppression, *Anal. Chem.*, **2012**, 84, 3489-3492.

5.1 Introduction

The control of a nanometer-wide gap between tip and substrate is critical for nanoscale applications of scanning electrochemical microscopy (SECM). Here we demonstrate that the stability of the nanogap in ambient conditions is significantly compromised by the thermal expansion and contraction of components of an SECM stage upon a temperature change and can be dramatically improved by suppressing the thermal drift in a newly developed isothermal chamber. Air temperature in the chamber changes only at ~0.2 mK/min to remarkably and reproducibly slow down the drift of tip–substrate distance to ~0.4 nm/min in contrast to 5–150 nm/min without the chamber. Eventually, the stability of the nanogap in the chamber is limited by its fluctuation with a standard deviation of ± 0.9 nm, which is mainly ascribed to the instability of a piezoelectric positioner. The sub-nanometer scale drift and fluctuation are

measured by forming a ~20 nm-wide gap under the 12 nm-radius nanopipet tip based on ion transfer at the liquid/liquid interface. The isothermal chamber is useful for SECM and, potentially, for other scanning probe microscopes, where thermal-drift errors in vertical and lateral probe positioning are unavoidable by the feedback-control of the probe–substrate distance.

Scanning electrochemical microscopy (SECM)[1,2] serves as a powerful nanoelectrochemical method with high spatial/time resolutions and superb sensitivity when a gap between tip and substrate is narrowed to nanometer scale. A nanoscale tip–substrate distance is required for operating a nanometer-sized SECM tip in the feedback mode to enable the imaging of substrate reactivity and/or topography with nanometer resolutions[3-6] and the kinetic measurements of rapid charge-transfer reactions at metal nanotips[7,8] or at liquid/liquid interfaces[9,10] under high mass transport conditions. Also, nanoscale SECM allows for the positive-feedback detection of a single electroactive molecule, which repeatedly undergoes electron-transfer reactions at the nanotip held at a few nanometers from a conductive substrate.[11-14] On the other hand, a micrometer-sized tip can be also used to form a nanogap over a much larger substrate as demonstrated in the kinetic study of rapid electron-transfer reactions.[15-17] In addition to a higher mass transport condition, the advantage of the nanogap against a conventional micrometer-wide gap is that a transient electron-transfer reaction at a macroscopic substrate can be investigated in the wide range of substrate potentials under quasi-steady states in either feedback or substrate generation/tip collection mode.[16,18] Moreover, an extremely short-lived intermediate can be generated and detected by forming a nanogap between two micrometer-sized electrodes with a thin insulating sheath.[19]

Here, we report on the novel approach based on an isothermal chamber to dramatically and reproducibly slow down the thermal drift of nanometer scale tip–substrate gaps to sub-

nanometer-per-minute levels, which are required for facilitating the aforementioned nanoscale applications of SECM or enabling them at a smaller scale. In fact, this work is the first to demonstrate that the minute-long stability of the nanogaps is limited to nanometer or sub-micrometer levels by the thermal expansion and contraction of components of an SECM stage as driven by a temperature change. In a previous SECM study, such a change in tip–substrate distance was ascribed to the drift of a piezoelectric positioner.[20] Importantly, the thermal drift has been recognized as the origin of vertical and lateral image distortions and unstable nanomanipulation in other scanning probe microscopy techniques even when the probe–substrate distance is feedback-controlled.[21,22] Currently, these problems due to thermal drift is unavoidable, unless a cryostat or fast scanning is employed, and is only correctable,[23] thereby augmenting the significance of our approach for the reduction of thermal-drift errors in tip positioning to sub-nanometer levels.

5.2 Results and Discussion

5.2.1 The significant drift of tip-substrate distance in the ambient environment

The significant drift of tip–substrate distance in the ambient environment of our laboratory was confirmed without the isothermal chamber when a tip was positioned at a feedback distance of <1 μm from a substrate and the feedback tip current was measured without any lateral tip scan, which minimizes the effect of substrate tilt on the tip current. For instance, Figure 5-1a shows the time profile of a current response at a 0.44 μm-radius Pt tip with a 0.22 μm-thick glass sheath as fabricated elsewhere[16] when the tip was brought to and positioned at 0.11 μm from the surface of a SiO_2/Si wafer. The width of a tip–substrate gap, *d*, as well as inner

and outer tip radii (a and r_g, respectively) were determined from the good fit of the tip current, i_T, with the theoretical negative feedback current as given by[24]

$$\frac{i_T}{i_{T,\infty}} = \frac{\frac{2.08}{RG^{0.358}}\left(L - \frac{0.145}{RG}\right) + 1.585}{\frac{2.08\left(L + 0.0023RG\right)}{RG^{0.358}} + 1.57 + \frac{\ln RG}{L} + \frac{2}{\pi RG}\ln\left(1 + \frac{\pi RG}{2L}\right)} \quad (1)$$

With

$$i_{T,\infty} = 4xnFDc^{*}a \quad (2)$$

where $RG = r_g/a$, $L = d/a$, $i_{T,\infty}$ is the diffusion-limited tip current in the bulk solution, x is a function of RG, n is the number of transferred charges in the tip reaction, and D and c^* are the diffusion coefficient and concentration of the original mediator in the bulk solution. Noticeably, a tip approach rate of 83.3 nm/s was used to convert the tip–substrate distance in eq 1 to time in Figure 5-1a. As soon as the tip approach was stopped, the tip current gradually increased to nearly completely recover to $i_{T,\infty}$ within ~10 minutes, where negative feedback effect became almost negligible. This result indicates that the tip–substrate gap became wider without moving a z-axis piezoelectric positioner. Quantitatively, the tip–substrate distance increased at ~100 nm/min in <10 minutes (Figure 5-1b) as calculated from the tip current using the following approximate equation for the inverse function of eq 1 where $RG = 1.5$ was employed.

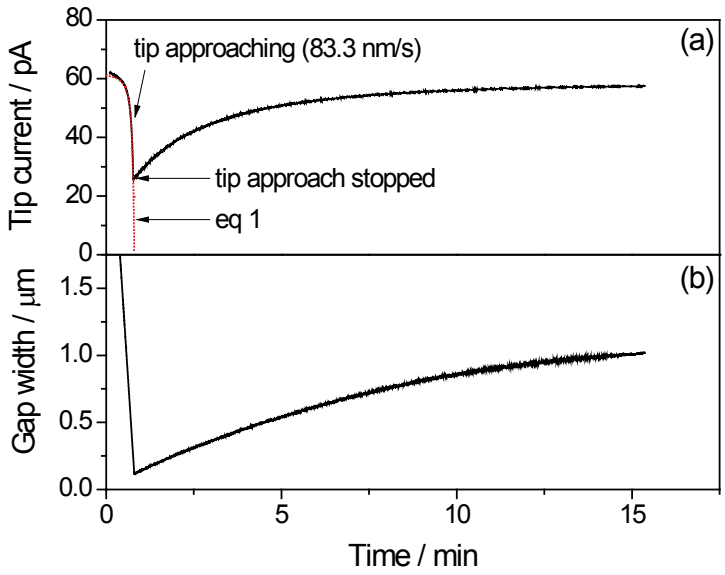

Figure 5-1. Time profile of (a) the tip current based on the oxidation of 0.5 mM ferrocenemethanol in 0.2 M NaCl without an isothermal chamber and (b) the corresponding width of the tip–substrate gap calculated using eq 3.

$$L = \left(2.35 \times 10^{-2}\right) \exp\left(6.99 i_T / i_{T,\infty}\right) - \left(3.5 \times 10^{-5}\right) \exp\left(13.3 \sqrt{i_T / i_{T,\infty}}\right) \qquad (3)$$

We repeatedly monitored the time profile of feedback tip current as the measure of tip–substrate distance without vertical or lateral tip scan on different days to find that the gap becomes either wider or narrower at drift rates in the wide range of 5–150 nm/min. Such drift

rates were obtained using the 0.5 μm-radius tip of either Pt or interface between two immiscible electrolyte solutions (ITIES) at the tip of a micropipet.[25] A total drift of up to 1 μm is too large to be ascribed to the hysteresis or creep of a piezoelectric positioner with a capacitive position sensor, which was operated in the closed-loop mode using an amplifier/servo controller. Similar drift rates were also obtained using an inchworm motor without closed-loop control (see Supporting Information). Overall, these results are consistent with our finding that the drift of tip–substrate distance is predominantly thermal (see below).

5.2.2 Suppression of thermal drift in the isothermal chamber

To suppress thermal drift, we developed an isothermal chamber (Figure 5-2) with a temperature stability of ~0.2 mK/min, which is comparable to that of <250 mK for 24 hours, i.e., <0.17 mK/min, in the laboratory where the closed-loop piezoelectric positioner is calibrated by its manufacturer at the sub-nanometer scale.[26] In addition, a ~10 cm-height SECM stage with a typical coefficient of linear thermal expansion in the order of 10^{-5} K^{-1} is expected to expand or contract only by 0.2 nm for a temperature change of 0.2 mK.[23] Specifically, we thermally isolated an SECM stage from the ambient environment using the box of the vacuum insulated panels (VIPs) based on a porous solid with pore sizes ranging from 10–100 nm, which are ~5–8 times thermally more resistive than polystylene and polyurethane foams with the same thickness.[27] Additionally, the SECM stage was surrounded by extruded aluminum heat sinks to quickly absorb excess heat from air in the chamber, which was heated by an operator and an illumination during the setup of SECM tip and cell. Also, the opening of the SECM solution cell was sealed with a rubber cap only with a small hole for the insertion of an SECM tip (Figure S-1a), thereby reducing cooling due to solvent evaporation. Finally, the chamber was closed with a

VIP (Figure 5-5b) and then tightly sandwiched between aluminum plates (Figure 5-5c) to squeeze any gap between VIPs.

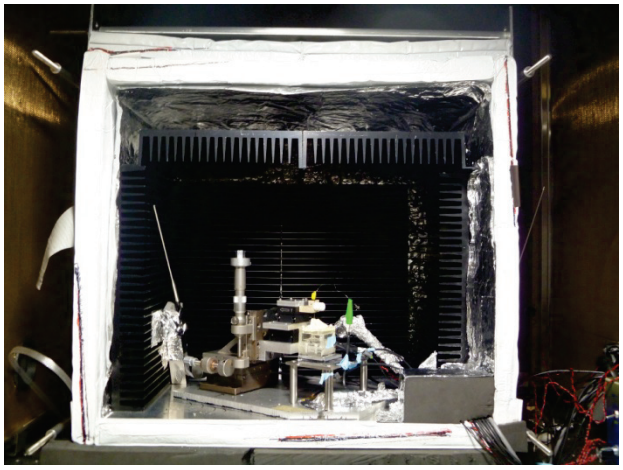

Figure 5-2. Image of an SECM stage in the isothermal chamber based on the box of VIPs (white) and extruded aluminum heat sinks (black). A thermometer is seen at the left-hand side of the stage while the neoprene foam (gray) is located at the right bottom corner. See Figure S-1a for details of the SECM stage and the capped cell.

The stable air temperature in the chamber was determined using a thermometer with a high resolution of 0.1 mK. Upon the closure of the chamber, the temperature typically increased, reached to a plateau within 10 minutes, and decreased only at ~0.2 mK/min for an hour (Figure 5-3). This decrease in the chamber temperature is likely due to the slow exchange of air between inside and outside of the chamber through gaps between VIPs and also through the holes for cables drilled in the neoprene foam (Figures 5-2 and 5-5a). On the other hand, the increase in the temperature upon the closure of the chamber is likely due to the self-heating of the thermometer,[28] which is noticeable when air convection is suppressed in the closed chamber. The

thermometer self-heating, however, was so local and weak that the stability of tip–substrate distance was unaffected by turning on or off the thermometer. Importantly, the achievement of the stable chamber temperature also requires the reduction of heating by an operator and the quick removal of the excess heat. Some care was taken (see Supporting Information for details) to minimize the temperature rise to 0.3 ºC during the setting up of SECM tip and cell (Figure 5-3). After the operator completed the setup and left the chamber, the temperature more quickly decreased because the excess heat in the chamber was absorbed by the aluminum heat sinks.

The sub-nanometer stability of a tip–substrate nanogap in the isothermal chamber was demonstrated using a nanopipet-supported ITIES tip[29] (see Supporting Information for nanopipet fabrication and SECM measurements). In Figure 5-4a, an $i_{T,\infty}$ value of 52 pA is based on the transfer of tetraethylammonium across the ITIES formed at the tip of a 1,2-dichloroethane-filled nanopipet, thereby yielding a tip radius of 12 nm in eq 2 with a typical *RG* value of ~1.5. The tip inner and outer radii were also confirmed by the good fit of eq 1 with the nanopipet approach curve at the insulating surface, where a tip approach rate of 10.0 nm/s was used to convert the tip–substrate distance in eq 1 to time in Figure 5-4a. After the tip was stopped at 22.3 nm from the SiO_2/Si wafer surface, the tip current decreased only by ~3 pA for 10 minutes, which is larger than the decrease of $i_{T,\infty}$ at the tip far away from a substrate (typically a decrease of ~1.5 pA at a 12 nm-radius tip for 10 minutes). The tip current in Figure 5-4a was converted to the tip–substrate distance using eq 3 (Figure 5-4b) to estimate a decrease of 4.6 nm in the distance. A drift rate of –0.44 nm/min was obtained from the linear fit of the distance versus time plot (red line in Figure 5-4b). Remarkably, this drift rate is 11–340 times lower than that without the chamber and is comparable to or better than that of 0.6–6 nm/min as reported for electrochemical scanning tunneling microscopy/spectroscopy.[30] Noticeably, the sub-nanometer scale drift of a

tip–substrate gap requires the operation of the piezoelectric positioner in the drift compensation mode,[31] which eliminates the drift of digital-analog converters on the main board of the controller.

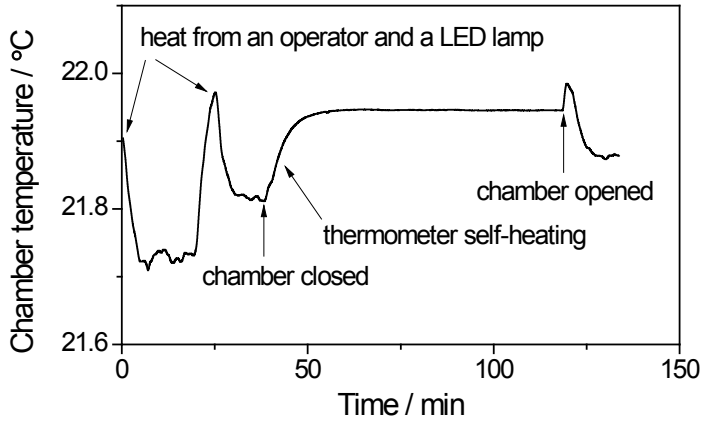

Figure 5-3. Time profile of air temperature in the isothermal chamber.

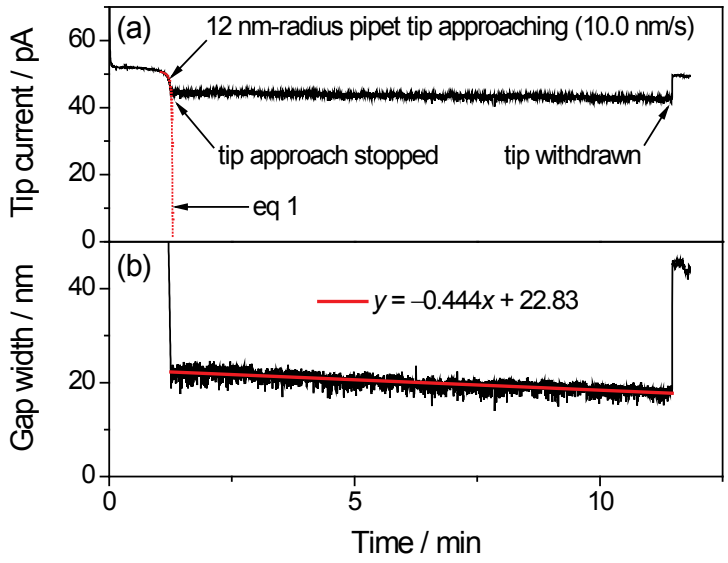

Figure 5-4. Time profile of (a) the tip current based on the transfer of 10 mM tetraethylammonium in 0.3 M KCl and (b) the corresponding tip–substrate gap width calculated using eq 3. Chamber temperature drifted at –0.2 mK/min during the current measurement.

Eventually, the stability of a tip–substrate gap in the isothermal chamber is limited by the sub-nanometer scale fluctuation of the gap, which results in noisier tip current at feedback distances than in the bulk solution (Figure 5-4a). The corresponding distance fluctuation with respect to the best linear fit in Figure 5-4b gives a standard deviation of ±0.9 nm. This fluctuation is mainly ascribed to the instability of the piezoelectric positioner, where the capacitive sensor gave relative piezo positions with a standard deviation of ± 0.4 nm (Figure 5-6). Such piezo fluctuation is negligible in comparison to typical tip–substrate distances of 0.1–1 μm at a 0.5 μm-radius tip,[16] which is seen as smooth feedback current without a chamber in Figure 1. Subsequently, the feedback current at the 0.5 μm-radius tip of Pt or micropipet-supported ITIES in the isothermal chamber showed negligible drift and fluctuation (data not shown).

5.3 Conclusions

The sub-nanometer scale stability of tip–substrate nanogaps with a drift rate of ~0.4 nm/min and a fluctuation of ~0.9 nm was achieved using the newly developed isothermal chamber with a temperature drift rate of only ~0.2 mK/min. This achievement is highly significant for facilitating nanoscale SECM measurements or enabling them at the smaller scale. In contrast, the thermal drift of the gap width without the chamber is much more significant and strongly depends on ambient conditions to vary in the wide range of 5–150 nm/min. This finding explains why the holding of a tip at a constant feedback distance of <1 μm for >1 min in imaging[32,33] and voltammetry[16] is sometimes very difficult in ambient conditions without the chamber. Thermal drift is much less problematic in approach curve measurements even with a <10 nm-radius tip,[34] which travels the whole feedback distance within seconds. Noticeably, the

thermal drift effect may be very different in other laboratories and with different SECM instruments and can be assessed simply by monitoring the feedback tip current without tip movement.

Our approach based on the isothermal chamber is robust and general because this approach is effective to tips and substrates with various sizes and materials.[1,2] The thermal drift of a tip–substrate gap in this chamber will be further suppressible by better designing an SECM stage including its dimensions and compositions while a more stable piezoelectric positioning system is required for the reduction of gap fluctuation. Noticeably, maintaining a constant tip–substrate distance using a distance-dependent feedback signal cannot avoid lateral and topographic distortions of an image due to thermal drift.[21,22] Our isothermal chamber will be useful for the reduction of thermal drift in various scanning probe microscopic techniques and also for such isothermal measurements as the long-term measurement of the temperature-sensitive resonance frequency of a quartz crystal microbalance.[35]

5.4 Supporting Information

5.4.1 Experimental Section

5.4.1.1 Chemicals. Tetradodecylammonium (TDDA) bromide, tetraethylammonium chloride (TEACl), potassium chloride, and *N*-dimethyltrimethyl silylamine were from sigma-aldrich. Potassium tetrakis(pentafluorophenyl)borate (TFAB) was from Boulder Scientific Company (Mead, CO). All reagents were used as received. The TFAB salt of TDDA was prepared by metathesis.[36] 10 mM TEACl was dissolved in 18.3 MΩ cm deionized water (Nanopure, Barnstead, Dubuque, IA) containing 0.3M KCl. The aqueous solution was filtered with a 0.2 μm filter (Fisher Scientific, Hanover Park, IL).

5.4.1.2 Nanopipet Fabrication. A quartz capillary (O.D. 1 mm, I.D. 0.7 mm, 10 cm long, Sutter Instrument, Novato, CA) was air blow cleaned before pulling and was pulled in a puller (Model P-2000,

Sutter Instrument) by running the line of a program with parameters of Heat 710, Filament 4, Velocity 30, Del120, Pul, 182. The pulled capillary was checked under microscope optical microscope (BX-41, Olympus America Inc., Melville, NY) to select the pipets with fainted tapered end of 1.2 ± 0.2 μm (magnification 50×), which corresponds to a real tip diameter of 20–30 nm as determined by field-emission SEM (model XL-30, Philips Electron Optics, Eindhoven, Netherlands) and also electrochemically (see the main text). The nanopipets were dried for >1 hour under vacuum in Mini-Vacuum Desiccator (Bel-Art Products, Pequannock, NJ) and then silanized by introducing 50 μL *N*-dimethyltrimethyl silylamine (Selectophore™ grade, Sigma-Aldrich, Saint Louis, MO) into the desiccator. Silanization was performed in the sealed desiccator for 50 ± 10 min, which was adjusted depending on the temperature and humidity of the atmosphere. After silanization, a vacuum was applied to the desiccator for ~1min to remove extra silanization agent, then nitrogen gas was introduced to the desiccator before it is opened to take away the silanized pipets. Thus prepared nanopipets were filled with 4 μL 1,2-dichloroethane containing 0.1 M tetradodecylammonium tetrakis(pentafluorophenyl)borate. It takes 2 minutes to fill with the DCE solution to a region of 250 μm from the tip of a well silanized nanopipet by gently tapping the outer pipet wall using a tweezers while a region of >1 mm from the tip of an inadequately silanized nanopipet was filled within 30 s. An electrochemically etched Pt wire (50 μm diameter, Goodfellow, Oakdale, PA) was inserted into the nanopipets as an organic reference/counter electrode. A modeling clay (Sargent Art, Inc., Hazleton, PA) was used to fix the position of the Pt wire. Thus prepared nanopipet electrode was used immediately for SECM experiments.

5.4.1.3 SECM Measurements. A home-built SECM stage (see the main text) was employed for tip positioning while the amperometric tip current was measured using the potentiostat of CHI 900 (CH Instruments, Austin, TX). The microscope stage was placed on a vibration isolation table with a faraday cage (model 63-533, TMC, Peabody, MA).

5.4.1.4 Isothermal Chamber. Here we show images of a capped SECM cell (Figure 5-5a) and the isothermal chamber closed with a VIP and then with a stainless steel plate (panels b and c, respectively).

(a)

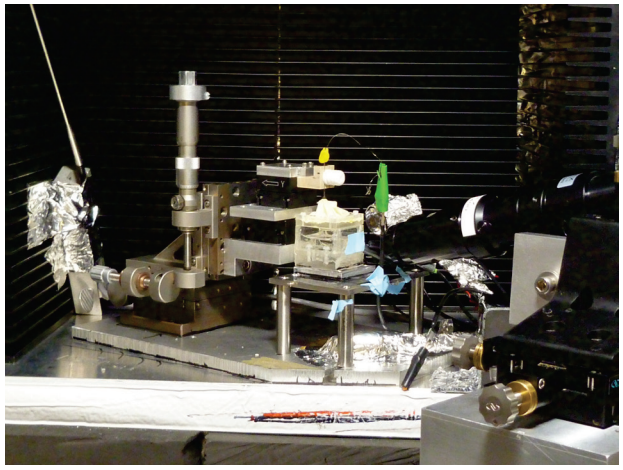

(b)

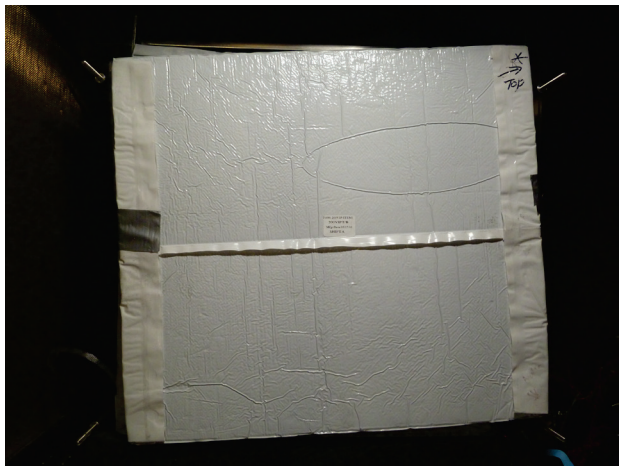

(c)

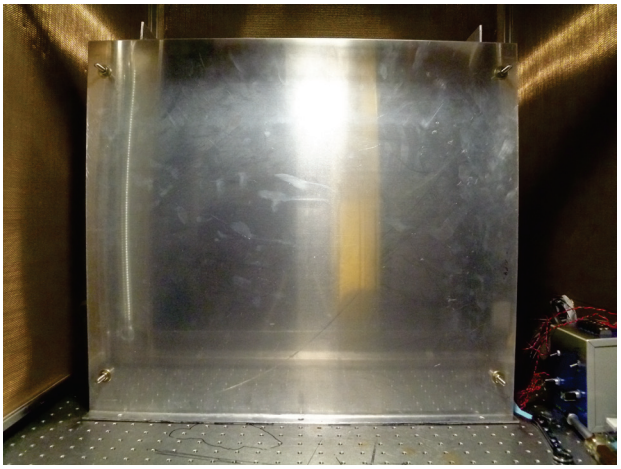

Figure 5-5. Images of (a) SECM stage, tip, and cell, and the isothermal chamber closed with (b) a VIP and (c) a stainless steel plate.

5.4.1.5 Relative Position of Piezoelectric Positioner. The position signal from the capacitive sensor of the piezoelectric positioner was plotted in Figure 5-6 to demonstrate the fluctuation of piezo position during the measurement of feedback tip current in Figure 4. The relative piezo position is defined against the position where the tip approach was stopped. The standard deviation of the relative piezo position was 0.4 nm. The maximum and minimum position changes were +1.4 and –1.7 nm.

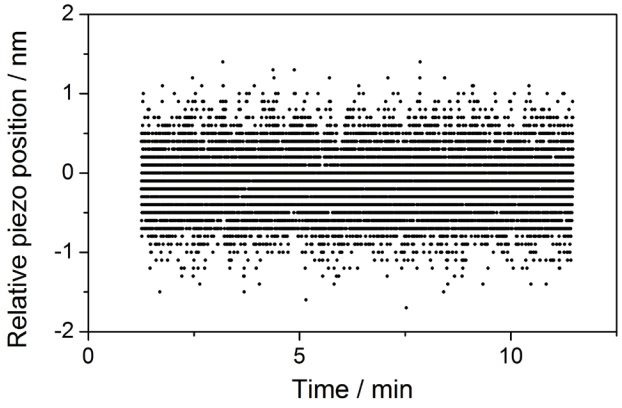

Figure 5-6. Plot of piezo position read from the capacitive sensor of the positioner. The zero position corresponds to the position where the tip approach was stopped.

ACKNOWLEDGEMENTS

This work was supported by grants from the National Institutes of Health (GM073439). We thank Prof. Patrick R. Unwin, Department of Chemistry, University of Warwick, for his valuable comments on thermal drift.

References

(1) *Scanning Electrochemical Microscopy*; Bard, A. J.; Mirkin, M. V., Eds.; Marcel Dekker: New York, 2001.

(2) Amemiya, S.; Bard, A. J.; Fan, F.-R. F.; Mirkin, M. V.; Unwin, P. R. *Ann. Rev. Anal. Chem.* **2008**, *1*, 95.

(3) Fan, F.-R. F.; Bard, A. J. *Proc. Natl. Acad. Sci. U.S.A.* **1999**, *96*, 14222.

(4) Sun, P.; Laforge, F. O.; Abeyweera, T. P.; Rotenberg, S. A.; Carpino, J.; Mirkin, M. V. *Proc. Natl. Acad. Sci. U.S.A.* **2008**, *105*, 443.

(5) Laforge, F. O.; Velmurugan, J.; Wang, Y.; Mirkin, M. V. *Anal. Chem.* **2009**, *81*, 3143.

(6) Takahashi, Y.; Shevchuk, A. I.; Novak, P.; Zhang, Y.; Ebejer, N.; Macpherson, J. V.; Unwin, P. R.; Pollard, A. J.; Roy, D.; Clifford, C. A.; Shiku, H.; Matsue, T.; Klenerman, D.; Korchev, Y. E. *Angew. Chem., Int. Ed.* **2011**, *50*, 9638.

(7) Sun, P.; Mirkin, M. V. *Anal. Chem.* **2006**, *78*, 6526.

(8) Velmurugan, J.; Sun, P.; Mirkin, M. V. *J. Phys. Chem. C* **2008**, *113*, 459.

(9) Sun, P.; Zhang, Z. Q.; Gao, Z.; Shao, Y. H. *Angew. Chem., Int. Ed.* **2002**, *41*, 3445.

(10) Li, F.; Chen, Y.; Sun, P.; Zhang, M. Q.; Gao, Z.; Zhan, D. P.; Shao, Y. H. *J. Phys. Chem. B* **2004**, *108*, 3295.

(11) Fan, F.-R. F.; Bard, A. J. *Science* **1995**, *267*, 871.

(12) Bard, A. J.; Fan, F.-R. F. *Acc. Chem. Res.* **1996**, *29*, 572.

(13) Fan, F.-R. F.; Kwak, J.; Bard, A. J. *J. Am. Chem. Soc.* **1996**, *118*, 9669.

(14) Sun, P.; Mirkin, M. V. *J. Am. Chem. Soc.* **2008**, *130*, 8241.

(15) Mirkin, M. V.; Richards, T. C.; Bard, A. J. *J. Phys. Chem.* **1993**, *87*, 7672.

(16) Nioradze, N.; Kim, J.; Amemiya, S. *Anal. Chem.* **2011**, *83*, 828.

(17) Shen, M.; Bard, A. J. *J. Am. Chem. Soc.* **2011**, *133*, 15737.

(18) Amemiya, S.; Nioradze, N.; Santhosh, P.; Deible, M. J. *Anal. Chem.* **2011**, *83*, 5928.

(19) Bi, S.; Liu, B.; Fan, F.-R. F.; Bard, A. J. *J. Am. Chem. Soc.* **2005**, *127*, 3690.

(20) O'Mullane, A. P.; Macpherson, J. V.; Unwin, P. R.; Cervera-Montesinos, J.; Manzanares, J. A.; Frehill, F.; Vos, J. G. *J. Phys. Chem. B* **2004**, *108*, 7219.

(21) Moheimani, S. O. R. *Rev. Sci. Instrum.* **2008**, *79*, 071101.

(22) Marinello, F.; Balcon, M.; Schiavuta, P.; Carmignato, S.; Savio, E. *Meas. Sci. Technol.* **2011**, *22*, 094016.

(23) Rahe, P.; Bechstein, R.; Kuhnle, A. *J. Vac. Sci. Technol., B* **2010**, *28*, C4E31.

(24) Lefrou, C. *J. Electroanal. Chem.* **2006**, *592*, 103.

(25) Ishimatsu, R.; Kim, J.; Jing, P.; Striemer, C. C.; Fang, D. Z.; Fauchet, P. M.; McGrath, J. L.; Amemiya, S. *Anal. Chem.* **2010**, *82*, 7127.

(26) http://www.physikinstrumente.com/en/products/nanopositioning/test_calibration.php (accessed Feburary 24, 2012).

(27) http://www.nanopore.com/vip.html (accessed Feburary 24, 2012).

(28) Nicholas, J. V.; White, D. R. *Traceable Temperatures: An Introduction to Temperature Measurement and Calibration*; 2nd ed.; Wiley and Sons, 2001, pp 223.

(29) Wang, Y.; Velmurugan, J.; Mirkin, M. V.; Rodgers, P. J.; Kim, J.; Amemiya, S. *Anal. Chem.* **2010**, *82*, 77.

(30) Hugelmann, P.; Schindler, W. *J. Phys. Chem. B* **2005**, *109*, 6262.

(31) *PZ116E User Manual: E-816 Computer Interface and Command Interpreter Submodule for Piezo Controller*; Physik Instrumente: Karlsruhe, Germany.

(32) Xiong, H.; Gross, D. A.; Guo, J.; Amemiya, S. *Anal. Chem.* **2006**, *78*, 1946.

(33) Kim, J.; Xiong, H.; Hofmann, M.; Kong, J.; Amemiya, S. *Anal. Chem.* **2010**, *82*, 1605.

(34) Elsamadisi, P.; Wang, Y.; Velmurugan, J.; Mirkin, M. V. *Anal. Chem.* **2011**, *83*, 671.

(35) Cimpoca, G. V.; Radulescu, C.; Popescu, I. V.; Dulama, I. D.; Ionita, I.; Cimpoca, M.; Cernica, I.; Gavrila, R. *AIP Conf. Proc.* **2010**, *1203*, 160.

(36) Guo, J.; Amemiya, S. *Anal. Chem.* **2006**, *78*, 6893.

6. Scanning Electrochemical Microscopy of One-Dimensional Nanostructure: Effects of Nanostructure Dimensions on the Tip Feedback Current under Unbiased Conditions

This work has been published as H. Xiong, J. Kim, E. Kim, and S. Amemiya, Scanning Electrochemical Microscopy of One-Dimensional Nanostructure: Effects of Nanostructure Dimensions on the Tip Feedback Current under Unbiased Conditions, *J. Electroanal. Chem.*, **2009**, *629*, 78-86.

6.1 Introduction

Scanning electrochemical microscopy (SECM) is developed as a powerful approach to electrochemical characterization of individual one-dimensional (1D) nanostructures under unbiased conditions. 1D nanostructures comprise anisotropic materials with both nanoscale and macroscale dimensions such as nanowires, nanotubes, nanobelts, and nanobands. Finite element simulations demonstrate that the feedback current at a disk-shaped ultramicroelectrode tip positioned above an unbiased nanoband, as prepared or placed on an insulating substrate, is sensitive to finite dimensions of the band, i.e., micrometer length, nanometer width, and nanometer height from the insulating surface. The electron-transfer rate of a redox mediator at the nanoband surface depends not only on the intrinsic rate but also on the open-circuit potential of the nanoband, which is determined by the dimensions of the nanoband as well as the tip inner and outer radii, and tip–substrate distance. The theoretical predictions are confirmed experimentally by employing Au nanobands as fabricated on a SiO_2 surface by electron-beam lithography, thereby yielding well defined dimensions of 100 or 500 nm in width, 47 nm in

height, and 50 μm in length. A 100 nm-wide nanoband can be detected by SECM imaging with ~2 μm-diameter tips although the tip feedback current is compromised by finite ET kinetics for $Ru(NH_3)_6^{3+}$ at the nanoband surface.

Significant progress in synthesis and fabrication of one-dimensional (1D) nanostructures has been made over the past decade [1]. 1D nanostructures comprise anisotropic nanomaterials with both nanoscale and micro- to macro-scale dimensions, such as nanowires, nanotubes, nanobelts, and nanobands. A representative example is a carbon nanotube, which has been extensively studied since its report in 1991 [2]. More recently, various approaches have been developed to prepare 1D nanomaterials with controlled shapes and dimensions from metals, semiconductors, and organic materials to manipulate their physical and chemical properties. On one hand, metallic and semi-conductive 1D nanostructures can be single crystals, where electronic transport is not governed by impurity or grain boundary scattering [3]. On the other hand, the composition of a 1D nanostructure can be altered along its long axis in a controlled manner [4].

Conductive and semi-conductive 1D nanostructures serve as novel electrode materials with fundamental and practical importance. Traditionally, such electrodes with both nanoscale and macroscale dimensions have been explored in electroanalytical chemistry [5] because of unique mass transfer properties of the high-aspect-ratio electrodes [6-9]. The anisotropic nanoelectrodes give a large and easily measurable faradic current, which varies with the macroscopic dimension. Non-faradic current, which depends on the total surface area, is suppressed at the nanoelectrodes, thereby lowering a voltammetric detection limit as demonstrated by employing nanoband electrodes based on the exposed edge of a ultrathin metal

film sandwiched between insulating phases [10] as well as carbon-nanotube-network electrodes [11]. A large local flux governed by the nanometer dimension allows for the study of nanoscale mass-transfer processes [12] and fast heterogeneous electron transfer (ET) kinetics [13]. Moreover, a larger interfacial capacity and the cathodic shift of the potential of zero charge were predicted theoretically for monoatomic nanowires, which differ from bulk electrodes in the double layer structure and work function [14]. Also, ET kinetics at a single-walled carbon nanotube was predicted to depend on the diameter and atomic structure of the tube, which control its electronic structure [15].

Recently [16], we proposed the "local" feedback mode of scanning electrochemical microscopy (SECM) [17, 18] to quantitatively probe an ET process at individual 1D nanostructures as prepared or placed on an insulating surface. In this feedback mode, a disk-shaped ultramicroelectrode tip is positioned above a conductive 1D nanostructure to electrolyze redox mediator molecules at the tip (Figure 6-1). Tip-generated species reacts at the surface of the nanostructure directly under the tip to regenerate the original mediators. The mediator regeneration occurs without an external circuit connected to the nanostructure, which mediates efficient transport of electrons to (or from) the original mediators at the exterior surface exposed to the bulk solution. An open circuit potential of such an unbiased nanostructure can be large enough to drive the mediator regeneration to a diffusion limitation when the largest dimension of the nanostructure is much larger than the tip diameter. The large diffusion-limited flux of the regenerated mediators from the nanostructure surface to the tip significantly enhances the tip current. It was predicted theoretically that a nanoband with a width that is much smaller than the smallest SECM tips ($\geq$30 nm in diameter [19]) is detectable in the local feedback mode even by employing a micrometer-sized tip when the diffusion limitation is achieved. On the other hand,

the largest dimension of typical 1D nanostructures reported so far is finite in comparison to a micrometer-sized tip so that a diffusion-limited condition is not necessarily expected, thereby compromising the tip feedback current.

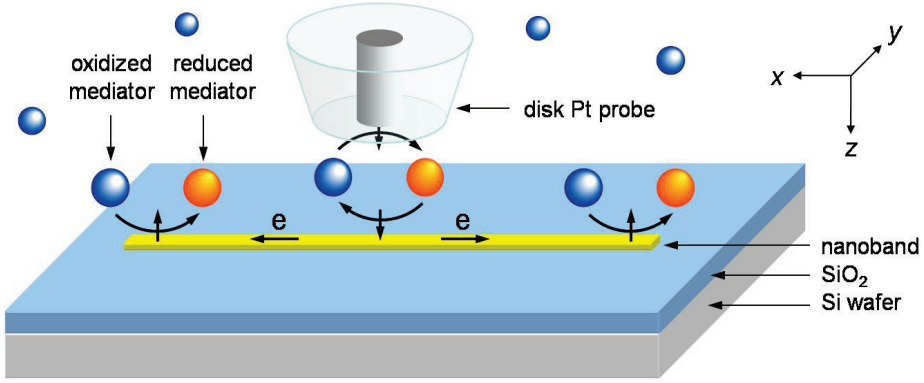

Figure 6-1. Scheme of an SECM feedback experiment with a disk ultramicroelectrode probe above a conductive 1D nanostructure (nanoband) on an insulating substrate.

Here we investigate the tip feedback current with 1D nanostructures with finite dimensions by considering as models nanometer-wide bands with a micrometer length and a nanometer height. A numerical model developed for unbiased disk substrates [20] is extended to predict the dependence of tip feedback current on nanoband dimensions and finite ET kinetics as well as SECM geometries including tip inner and outer radii and tip–substrate distance. While a variety of unbiased substrates were studied experimentally by SECM [17, 18], theories for the unbiased conditions were developed only for infinitely large substrates or finite disk-shaped

substrates [20-22]. The theoretical predictions are assessed experimentally by investigating 50 μm-long Au nanobands with 100 or 500 nm in width and 47 nm in height as fabricated on the SiO_2 surface by electron-beam lithography. $Ru(NH_3)_6^{3+}$ is employed as a facile redox mediator to find rather slow ET kinetics at the Au nanobands. We ascribe the slow ET rates to the passivation of the nanoband surface with Cr oxide that originates from the underlying Cr adhesion layer [23, 24].

6.2 Theory

6.2.1. Model

A three-dimensional SECM diffusion problem with a finitely long nanoband positioned under a disk probe is defined in the Cartesian coordinate [16] (Figure 6-2). The origin of the coordinate axes is set at the center of the disk tip with the radius, a. A band electrode is faced in parallel to the probe surface such that the band center is just under the origin. The distance between the tip and band surfaces are given by d. The nanometer width and height, and micrometer length of the band are defined as w, h, and l, respectively. Actual simulations are carried out in the quarter of the whole domain with x, $y > 0$. The outer substrate radius corresponds to $50a$ and limits the simulation space in the x and y directions. The simulation space behind the tip is defined by $20a$. This value is large enough to accurately simulate the back diffusion of a mediator at a probe, even with RG ($= r_g/a$) < 10 [25], where r_g is the outer radius of the insulating sheath at the tip. Initially, the solution phase contains only one redox-active mediator, O.

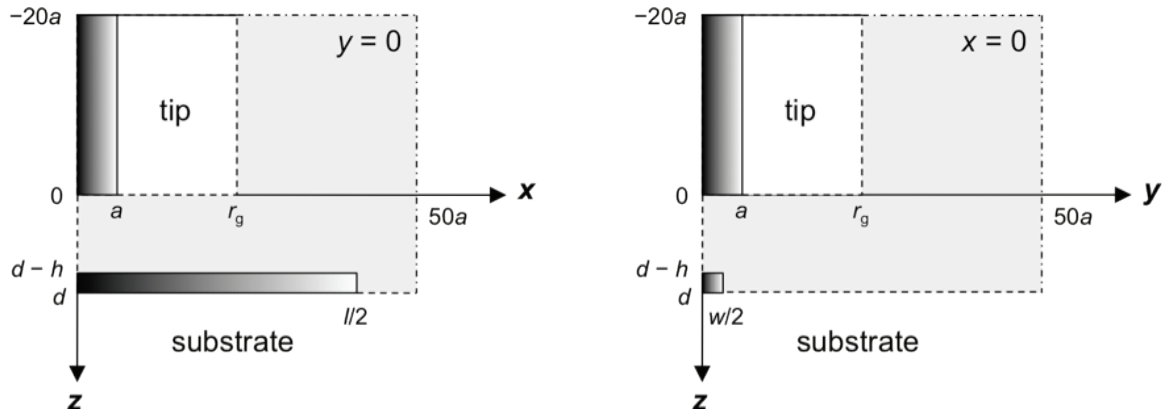

Figure 6-2. Geometry of the SECM diffusion problem in the Cartesian coordinate as represented by cross sections at $y = 0$ (left) and $x = 0$ (right). There is no normal flux at dashed lines while dash-dot lines represent simulation space limits.

Amperometric tip current is based on a diffusion-limited reduction of O to R at the tip (O + ne → R). When the tip is positioned in the bulk solution, a steady-state diffusion-limited current at the tip, $i_{T,\infty}$, is given by

$$i_{T,\infty} = 4xnFDc_0a \qquad (1)$$

where x is the function of RG [26], n is the number of electrons transferred per redox molecule, F is Faraday's constant, D and c_0 are the diffusion coefficient and concentration of the redox mediator in the bulk solution. On the other hand, the SECM diffusion problem was solved numerically to obtain the tip current, i_T, at the tip–substrate distance, d, as given by

$$i_T = 2\pi nFD\int_0^a x\left[\frac{\partial c}{\partial z}\right]_{y,z=0} dx \qquad (2)$$

The solution of the diffusion problem with an unbiased nanoband was considered to be accurate when the open circuit potential of the nanoband, E, was chosen such that the substrate current, i_s, is less than 1% of $i_{T,\infty}$ to satisfy the zero-current condition at the unbiased nanoband [20]. The substrate current is given by

$$i_S = nFD\oint\left[\frac{\partial c}{\partial z}\right]_{z=d-h} dS \tag{3}$$

The plots of the tip current and the corresponding open-circuit potential versus the tip–substrate distance give current and potential approach curves, respectively.

A three-dimensional SECM diffusion problem is defined by

$$D\left[\frac{\partial^2 c(x,y,z)}{\partial x^2} + \frac{\partial^2 c(x,y,z)}{\partial y^2} + \frac{\partial^2 c(x,y,z)}{\partial z^2}\right] = 0 \tag{4}$$

where $c(x, y, z)$ is a steady-state concentration of O. A steady state was assumed in eq 4 although only a quasi-steady state is expected with a long nanoband (see 6.3.3). The diffusion coefficients of O and R are assumed to be the mean value so that mathematical treatment is restricted to the concentration of O.

A boundary condition on the nanoband surface depends on the rate of mediator regeneration. When mediator regeneration occurs at a diffusion-limited rate, the boundary condition is given by

$$c(x, y, d) = c_0 \qquad |x| \le l/2, y \le w/2 \tag{5}$$

A substrate boundary condition for reversible mediator regeneration is given by Nernst equation as

$$E = E^{0'} - \frac{RT}{nF}\ln\frac{c_0 - c(x,y,d)}{c(x,y,d)} \qquad |x| \le l/2, y \le w/2 \tag{6}$$

where $E^{0'}$ is the formal potential. The nanoband is assumed to be conductive enough to maintain the uniform potential, E, within the phase. When the mediator regeneration is kinetically limited, only one-step, one-electron transfer processes (n = 1) are considered

$$\mathrm{O} + \mathrm{e} \underset{}{\overset{k_{f,s}}{\rightleftharpoons}} \mathrm{R} \tag{7}$$

$k_{b,s}$

where $k_{f,s}$ and $k_{b,s}$ are the first-order heterogeneous rate constants. The rate constants are given by the Butler-Volmer relations as

$$k_{f,s} = k^0 \exp[-\alpha F(E - E^{0'})/RT] \tag{8}$$

$$k_{b,s} = k^0 \exp[(1-\alpha) F(E - E^{0'})/RT] \tag{9}$$

where k^0 is the standard rate constant, and α is the transfer coefficient. The corresponding substrate surface boundary condition is given by

$$D\left[\frac{\partial c(x,y,z)}{\partial z}\right]_{z=d} = -k_{f,s} c(x,y,d) + k_{b,s}[c_0 - c(x,y,d)] \qquad |x| \le l/2, y \le w/2 \tag{10}$$

The boundary condition at the tip surface is given by

$$c(x, y, 0) = 0 \qquad x^2 + y^2 \le a^2 \tag{11}$$

The other boundary conditions are given in Figure 6-2.

This steady state SECM diffusion problem was solved using COMSOL Multiphysics version 3.4 (COMSOL, Inc., Burlington, MA), which applies the finite element method. With the large space required for incorporating long nanobands ($l/2a \le 40$), the band width was limited to $w/2a \ge 0.015$ for successful simulations under given conditions. Thus, $w/2a = 0.015$ was employed in this theory section. Calculation at each tip position took < 2 min on a PC equipped with an Intel Core2 Quad CPU at 2.4 GHz and 4.0 GB RAM with Windows XP Professional.

6.2.2. Diffusion-limited feedback at inlaid nanobands with various lengths

SECM approach curves were simulated for nanobands with various lengths under a diffusion-limited condition at the nanoband surface (eq 5). The application of an external bias to a finitely long nanoband ($l/2a \leq 40$) is required for diffusion-limited mediator regeneration (see 6.2.3). A very short nanoband is detectable under the diffusion-limited condition, where mediator regeneration is most efficient to maximize the tip feedback current. Moreover, mediator regeneration at the biased nanoband is coupled with electron transport to an external circuit, thereby eliminating the need of an exterior nanoband surface for electrolysis of the original mediators (Figure 6-1). The approach curve simulated under the diffusion-limited condition becomes only slightly negative as $l/2a$ decreases from 40 to 1.5 (Figure 6-3a), which is long enough to efficiently collect the tip-generated species for mediator regeneration. As a band becomes shorter than $l/2a = 1.5$, an approach curve becomes more negative. A nanoband with $l/2a = 0.1$, however, is still distinguishable from an insulating surface.

The simulation results demonstrate that a nanoband with a very small surface area is detectable by SECM under the diffusion-limited condition. Bands with $w/2a = 0.015$ and $l/2a = 0.1$–1.5 possesses total surface areas of only 0.0048–0.072 % with respect to the tip area. In contrast, SECM allows for the identification of a biased disk substrate with the radius that is at least 10 % of the tip radius, corresponding to a total substrate area of >1 % with respect to the tip area [27]. A nanoband with a much smaller area is detectable, because the local feedback effect weakly depends on the width of a band when the width is much narrower than the tip diameter ($w << 2a$) [16].

(a)

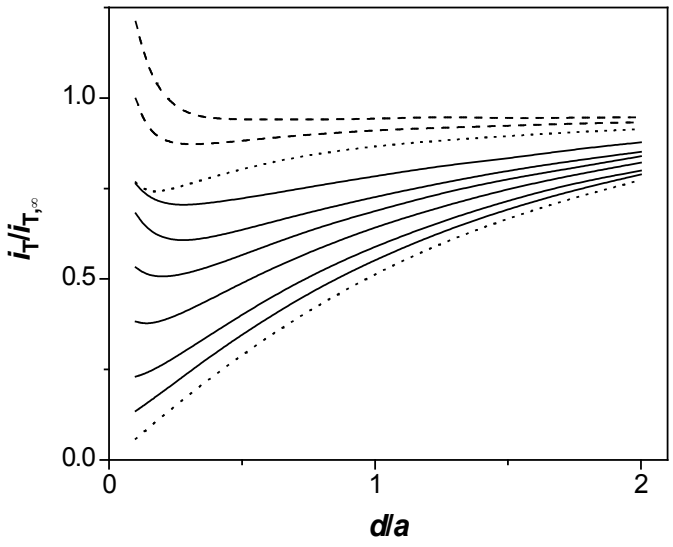

(b)

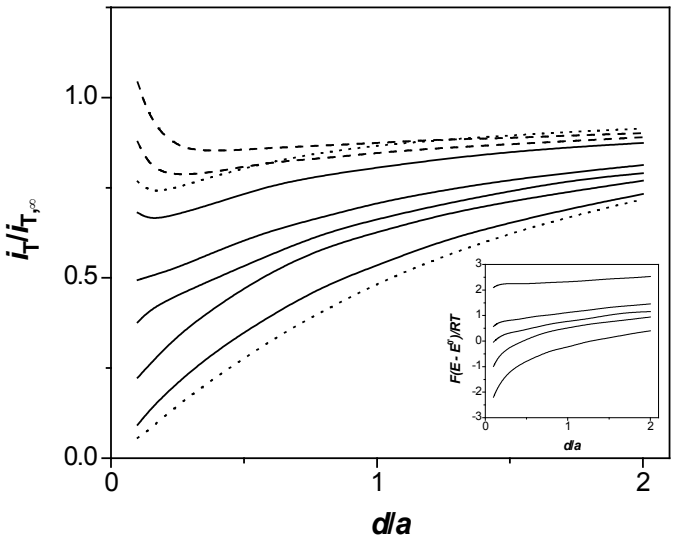

Figure 6-3. Effects of band length and height on steady-state current approach curves for (a) diffusion-limited and (b) reversible ET at nanobands with $w/2a$ = 0.015 under biased and unbiased conditions,

respectively, as simulated for a disk probe with RG = 10. The solid lines are for inlaid nanobands with $l/2a$ = (a) 1.5, 1, 0.75, 0.5, 0.25, 0.1 and (b) 40, 15, 12, 10, 5 from the top. The dashed lines are for raised nanobands with $l/2a$ = 40 and h/w = 2 and 1 from the top. The upper dotted lines represent a diffusion-limited curve at a nanoband with $w/2a$ = 0.015 and $l/2a$ = 40. The lower dotted lines represent an approach curve at an insulating substrate. The inset in (b) shows corresponding potential approach curves at the inlaid nanobands with $l/2a$ = 40, 15, 12, 10, 5 from the top.

6.2.3. Reversible feedback at inlaid nanobands with various lengths

Effects of band length on the tip current were examined for reversible ET at unbiased nanobands as defined by the Nernst equation (eq 6). In comparison to the biased, diffusion-limited case, a much longer nanoband is required for SECM detection under an unbiased condition. The large exterior surface of an unbiased nanoband must be exposed to the bulk solution for mediator electrolysis, which is coupled with mediator regeneration at the nanoband surface under the tip (Figure 6-1). Simulated approach curves demonstrate that an unbiased nanoband with $l/2a$ = 40 is not long enough to drive mediator regeneration to a diffusion limitation (Figure 6-3b). An approach curve becomes more negative with a shorter nanoband in the range of $5 < l/2a < 40$. An approach curve is very negative with a nanoband with $l/2a$ = 5, which is ~50 times longer than the shortest nanoband that is detectable by SECM under a diffusion-limited condition.

A shorter nanoband under an unbiased condition possesses a smaller overpotential for mediator regeneration as given by $E - E^{0'}$ (the inset of Figure 6-3b), thereby yielding a smaller tip feedback current. The open circuit potential of an unbiased nanoband is set such that the total influx of electrons into the nanoband by mediator regeneration (or electrolysis) balances with the total efflux of electrons from the nanoband by mediator electrolysis (or regeneration). A nanoband with $l/2a > 1$ is long enough to

efficiently collect the tip-generated species. The smaller exterior surface of a shorter nanoband, however, is exposed to the bulk solution for mediator electrolysis, thereby resulting in a smaller overpotential for mediator regeneration.

Notably, an unbiased nanoband with a much smaller area is detectable by SECM in comparison to an unbiased disk. Only ~1 % of the substrate surface just under a tip is covered by a nanoband with $w/2a = 0.015$. In contrast, an unbiased disk substrate must be larger than the disk tip for detecting a feedback effect, thereby corresponding to a relative substrate area of >100 % [20]. The larger feedback effect at an unbiased nanoband is ascribed to weak width dependence of the flux based on hemicylindrical diffusion of the original and tip-generated redox species at the nanoband [16]. Moreover, a substrate with a higher aspect ratio exposes a larger exterior surface to the bulk solution for mediator electrolysis.

6.2.4. Tip current dependence on band height

The finite element simulation also demonstrates that the tip feedback current is larger with a higher nanoband, which possesses a larger surface area that is available for both regeneration and electrolysis of a redox mediator. The feedback effect is more enhanced for diffusion-limited ET than for reversible ET when $h/2w$ varies from 0 to 2 (Figure 6-3a and b). Interestingly, the approach curves at the raised nanobands become positive at short distances. A hemicylindrical diffusion layer at a raised nanoband interacts significantly with the tip surface (Figure 6-4a) so that the thinning of the diffusion layer at a shorter tip–nanoband distance results in the positive current change. Significant effects of the band height on kinetically limited feedback current are also demonstrated experimentally (see 6.3.2 and 6.3.3).

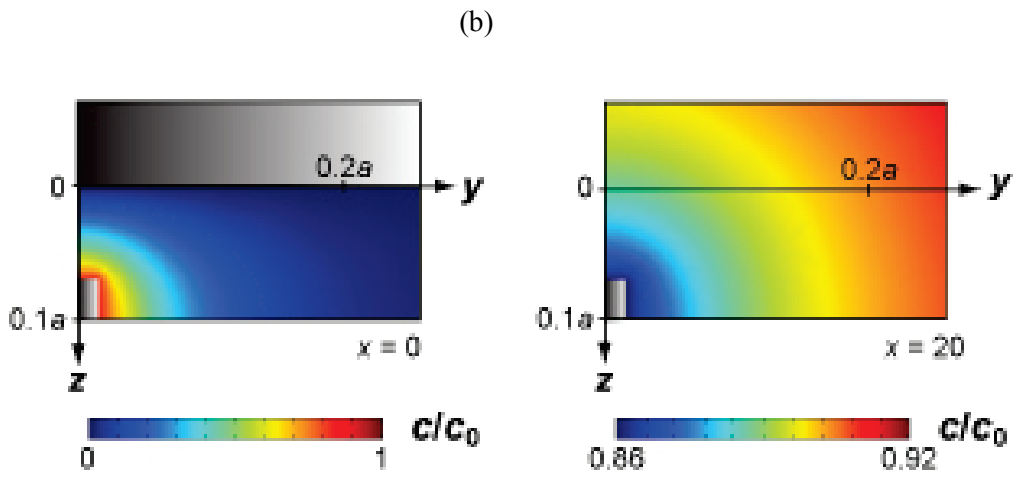

Figure 6-4. Simulated concentration profiles of a reversible redox mediator at x = (a) 0 and (b) 20 simulated for an unbiased raised nanoband with $w/2a$ = 0.015, $l/2a$ = 40, and h/w = 2. The distance between the tip and insulating substrate is 0.1a. The tip RG is 10. The mediator concentration at the nanoband surface is 0.86c_0.

6.2.5. Quasi-steady-state diffusion at unbiased nanobands

Steady-state diffusion without a convection effect as assumed in our model is a good approximation for quasi-steady-state hemicylindrical diffusion at a long nanoband [6-9] under the SECM configuration. The hemicylindrical diffusion layer with the thickness that is controlled by the band width and height is developed not only at the region of the nanoband surface under the tip (Figure 6-4a) but also at the region exposed to the bulk solution (Figures 6-4b). A mediator concentration at the exposed surface, however, recovers quickly from 86 % of the bulk concentration to 92 % within the small region depicted in Figure 6-4b and then gradually to 99 % at 15 normalized distances from the surface. This concentration profile is not significantly affected by the simulation space limits. This result predicts that a quasi-steady-state concentration profile is maintained at long times without a convection effect, which is significant in

the outside of the 99% contour with a micrometer-sized tip. A true steady state at a long nanoband under an SECM probe requires biased conditions, where no mediator electrolysis at the long exposed surface occurs.

6.2.6. Kinetically limited feedback current

The SECM tip current depends on heterogeneous ET kinetics at an unbiased nanoband with a finite length, which is not long enough to drive mediator regeneration to a diffusion limitation. Here we employ inlaid nanobands to evaluate this kinetic effect, which is also addressed experimentally for raised nanobands (see 6.3.2 and 6.3.3). Simulations were carried out for unbiased inlaid nanobands with $w/2a$ = 0.015 and $l/2a$ = 40 to investigate the kinetic effect for quasi-reversible ET as defined by Butler-Volmer relations [28] (eqs 8 and 9). An intrinsic ET rate in the simulations was defined in the normalized form, K, as given by

$$K = \frac{k^0 a}{D} \tag{12}$$

As K becomes smaller from 100 to 1, the corresponding approach curve becomes more negative to change from a reversible curve to a purely negative curve despite the large overpotential of the relatively long nanoband with $l/2a$ = 40 (the inset of Figure 6-5). A similar trend was also observed with a shorter unbiased nanoband with $l/2a$ = 12 (data not shown).

It should be noted that a reversible response at an unbiased nanoband requires $K > 100$, which is much larger than the K value of ~10 required for a reversible response at an unbiased disk substrate [20]. A K value represents the ratio of a k^0 value with respect to a steady-state mass transfer coefficient at the tip in a bulk solution, i.e., ~D/a, which increases to ~D/d with a large conductive substrate under the tip ($d < a$) [29]. These mass transfer coefficients, however, are much smaller than the corresponding steady-state mass transfer coefficient at a nanoband under an SECM tip. The mass transfer coefficient based on

hemicylindrical diffusion at the nanoband is inversely proportional to the band width and logarithmically depends on the tip–substrate distance and tip diameter when the band width is much smaller than the tip diameter ($w << 2a$) [16]. The faster mass transfer at a nanoband results in a kinetic limitation with a larger K value.

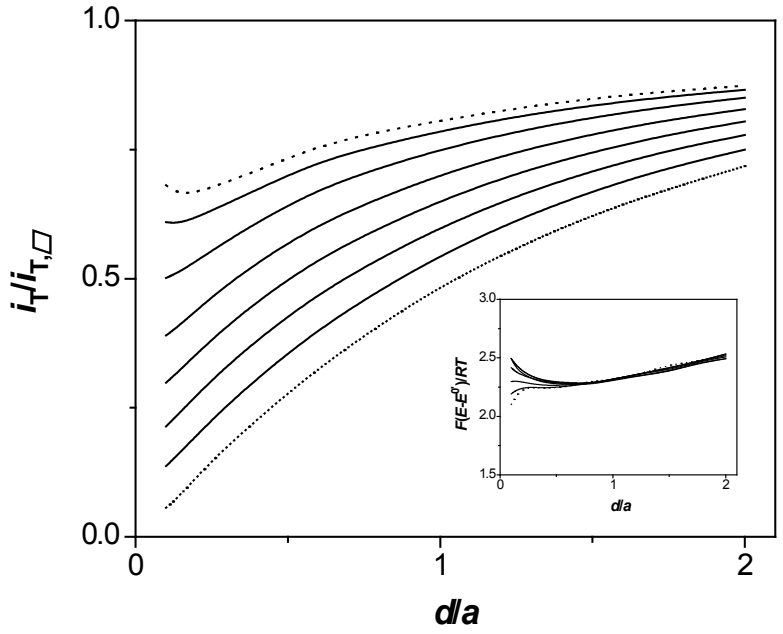

Figure 6-5. Effects of ET kinetics on steady-state current approach curves at an unbiased inlaid nanoband with $w/2a$ = 0.015 and $l/2a$ = 40 as simulated for a disk probe with RG = 10. The solid lines are for K = 100, 25, 10, 5, 2.5, 1 from the top. The upper dotted line represents a reversible curve at the nanoband. The lower dotted line represents an approach curve at an insulating substrate. The solid lines in the inset represent corresponding potential approach curves for K = 100, 25, 10, 5, 2.5, 1 from the bottom, where curves for K = 5, 2.5, 1 overlap. The dotted line is a reversible curve.

6.2.7. Effects of tip RG

The feedback mechanism with an unbiased nanoband is better understood by considering effects of tip RG on the tip feedback current. With a thinner insulating sheath surrounding the tip, a larger exterior surface of a nanoband is exposed to the bulk solution for electrolysis of original mediator molecules (Figure 6-1). More efficient mediator electrolysis enhances mediator regeneration at the nanoband surface under the tip, thereby resulting in a larger tip current. The RG effects were simulated for reversible ET at an inlaid nanoband with $l/2a$ = 10 (Figure 6-6a). The simulation results confirm a larger current at a tip with a smaller outer radius in the range of 1.5 ≤ RG ≤ 20. The simulated fluxes of the original mediators at the nanoband surface support the mechanism of the RG effect (Figure 6-6b). A negative flux based on mediator regeneration is localized under the tip with any RG, indicating that a nanoband with $l/2a$ > 1 is long enough to efficiently collect tip-generated species. A larger negative flux under a tip with smaller RG is balanced by a larger positive flux based on mediator electrolysis, which occurs at a larger exposed surface of the nanoband in the region of ~RG < x/a ≤ 10. Overall, the tip feedback current depends on the band length with respect to the tip outer diameter, i.e., $l/2r_g$.

The RG effect at an unbiased nanoband is moderate in comparison to that at an unbiased disk substrate, which gives a positive approach curve when the tip outer diameter is comparable to or smaller than the substrate diameter [20]. In contrast, a negative approach curve at an unbiased nanoband is limited by the band width when the tip outer diameter is much smaller than the band length, i.e., $w << 2r_g << l$. Moreover, an overpotential at the unbiased nanoband with $w/2a$ = 0.015 and $l/2a$ = 10 becomes larger with smaller RG but is not large enough to drive the mediator regeneration to the diffusion limitation even with RG = 1.5 (the inset of Figure 6-6a). In fact, the significant fraction of the large tip current with RG = 1.5 is ascribed to less hindered diffusion of redox mediator molecules from the bulk solution to the tip [30].

(a)

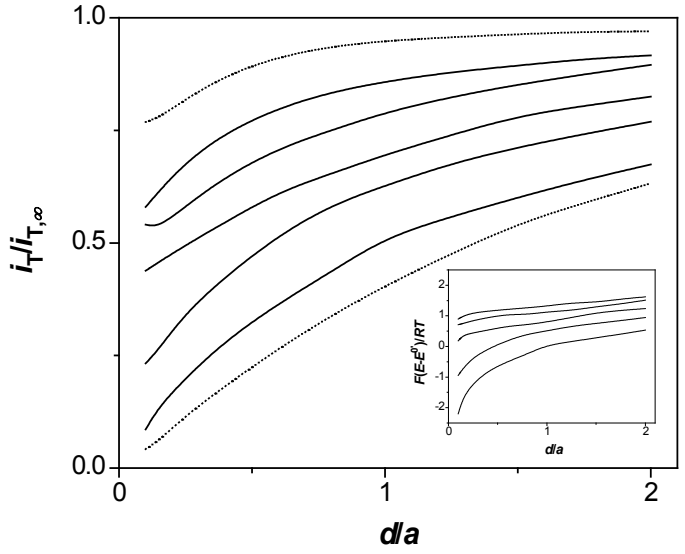

(b)

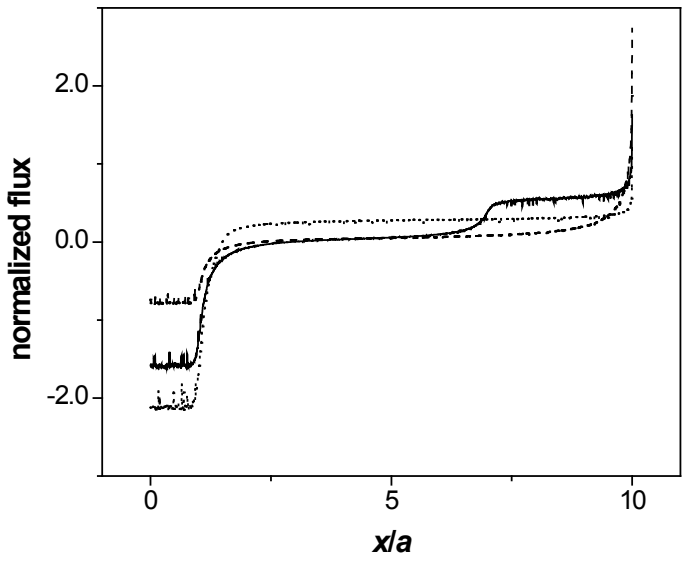

Figure 6-6. (a) RG effects on reversible approach curves at an unbiased inlaid nanoband with $w/2a$ = 0.015 and $l/2a$ = 10 as simulated at a steady state for disk probes with RG = 1.5, 4, 7, 10, 20 from the top

(solid lines). The upper dotted line represents a diffusion-limited curve at the nanoband for the probe with RG = 1.5. The lower dotted line represents an approach curve at an insulating substrate for the probe with RG = 20. The inset shows corresponding potential approach curves for probes with RG = 1.5, 4, 7, 10, 20 from the top. (b) Simulated steady-state fluxes at the surface of the nanoband along the x-axis at $y = 0$ and $z = d$ for probes with RG = 1.5, 7, and 10 (dotted, solid, and dashed lines, respectively).

6.3 Experimental section

6.3.1. Nanoband fabrication by electron-beam lithography

An array of nanobands with 100 or 500 nm in width, 47 nm in height, and 50 μm in length was fabricated on a SiO_2-covered silicon wafer by electron-beam lithography (Scheme 6-1). A 700 nm-thick thermal oxide was grown at 1100 °C under flowing O_2 on an RCA standard cleaned silicon chip (a 380 μm thick wafer polished on both sides, Silicon Quest, Santa Clara, CA). A side of the chip was spin-coated with poly(methylmethacrylate)/poly(methylmethacrylate-co-methacrylic acid) as an electron-beam bilayer resist. An electron-beam tool (model EBPG-5HR, Leica Microsystems, Wetzlar, Germany) was used to expose the resist-coated chip to an electron beam. The exposed parts were dissolved by immersing the sample in the methyl isobutyl ketone:isopropyl alcohol (1:1 v/v) developer. A 5 nm-thick Cr film and then a 47 nm-thick Au film were deposited by electron-gun evaporation (Semicore Equipment, Inc., Livermore, CA, USA). The remaining resist and the metal on top of it were removed using Microposit Remover 1165. The lateral dimensions of the nanobands were characterized by field-emission SEM (model XL-30, Philips Electron Optics, Eindhoven, Netherlands) while the band height was determined by AFM (Dimension 3100, Digital Instrument, Inc., Santa Barbara, CA, USA) in tapping mode.

Scheme 6-1. Nanoband Fabrication

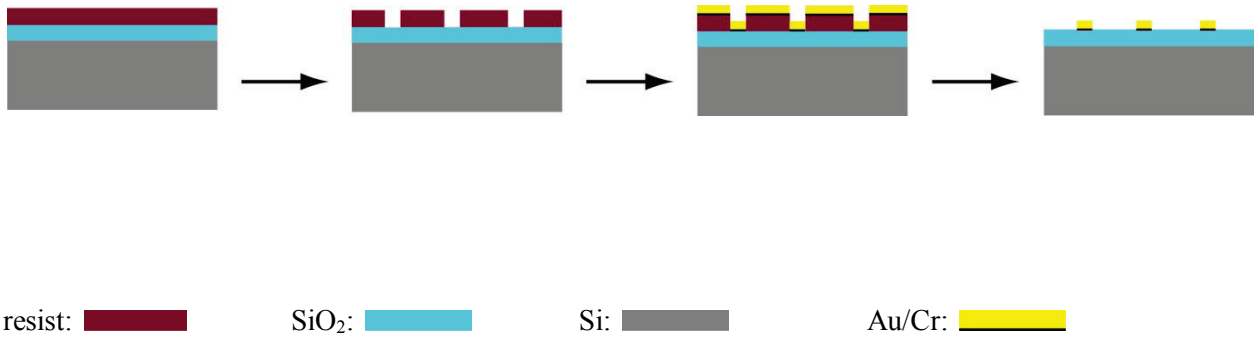

6.3.2. SECM measurements

A commercial SECM instrument with close-loop piezoelectric motors (CHI 910B, CH Instruments, Austin, TX, USA) was used for approach curve and imaging experiments. The instrument was placed on a vibration isolation platform (model 63-533, TMC, Peabody, MA, USA). A two-electrode setup was employed with a 1 mm-diameter AgCl-coated Ag wire (or a Ag wire for experiments with $KClO_4$ as supporting electrolytes) serving as a reference/counter electrode and a 2.2 or 2.8 μm-diameter Pt disk electrode with RG = 10 (CH Instruments) as an SECM probe. The inner and outer tip radii of the Pt probes were determined from current approach curves at an insulating Teflon substrate [25, 31]. The tip radii were also checked by optical microscopy.

The surfaces of the Au nanobands were cleaned before SECM experiments. Specifically, the nanoband array was soaked in acetone for 1 hour, dried with nitrogen, treated for 1 hour in a UV/ozone cleaner [32] (UV-tip Cleaner, BioForce Nanosciences, Ames, IA, USA), soaked in ethanol for 1 hour, and

dried with nitrogen. The pretreatment did not change a dimension of a nanoband as confirmed by SEM and AFM.

The nanoband array was placed in an SECM cell filled with 0.1 or 0.05 M KCl containing 1 or 2 mM $Ru(NH_3)_6Cl_3$ (Strem Chemicals, Newburyport, MA, USA) or 0.05 M $KClO_4$ containing $Ru(NH_3)_6(ClO_4)_3$. The perchlorate salt was prepared as a precipitate from the saturated aqueous solution of $Ru(NH_3)_6Cl_3$ by adding concentrated $HClO_4$. The precipitate was filtered, washed with concentrated $HClO_4$, and recrystallized from 0.05M $HClO_4$ at 0 ºC. The purified salt is free from chloride, because no precipitate was detected after the addition of excess $AgNO_3$ to the aqueous solution of the salt. The aqueous solutions were prepared with 18.3 MΩ·cm deionized water (Nanopure, Barnstead, Dubuque, IA).

An SECM probe was positioned above the center of a nanoband for approach curve measurements. First, the probe was brought vertically to a short distance from the SiO_2 surface by monitoring a decrease of the tip current. Then, the tip center was positioned just above the nanoband during a line scan at a constant height in the *y*-direction, where a peak current was obtained (see 6.4.1). Finally, the tip was scanned laterally in the *x*-direction to find the center of the nanoband. SECM approach curves thus obtained were independent of a rate of the probe scan in the *z*-direction. The apparently steady-state approach curves were analyzed numerically by assuming steady-state diffusion of redox molecules without a convection effect (see 6.2.5).

6.4 Results and discussion

6.4.1 SECM imaging of a 100 nm-wide band

Here we apply SECM to electrochemical characterization of Au nanobands with finite dimensions as models of 1D nanostructures. Figure 6-7 shows SEM images of a Au band with 100 nm in width, 47 nm in height, and 50 μm in length as prepared on a SiO_2-covered Si wafer

by electron-beam lithography. A nanoband in the array format is separated at least by 200 μm from another nanoband. Such a Au nanoband enables us to investigate the dependence of the tip feedback current on the finite dimensions as well as finite ET kinetics, which were not addressable in our previous study of centimeter-long inlaid nanobands under diffusion-limited conditions [16].

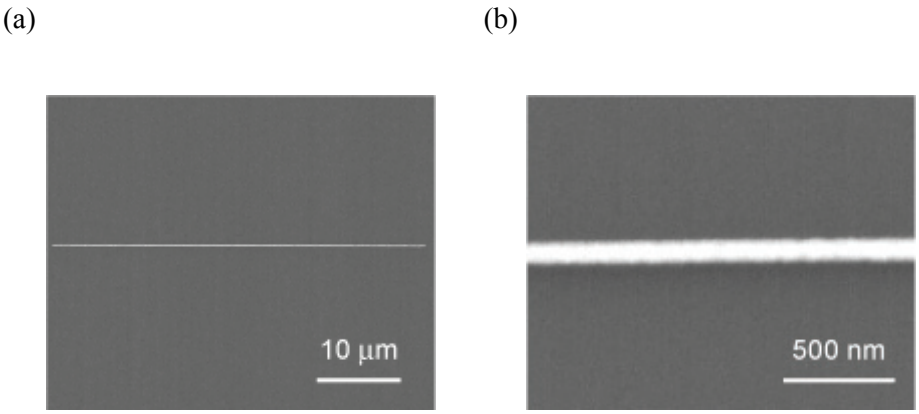

Figure 6-7. Lower (left) and higher (right) resolution SEM images of a Au nanoband with 100 nm in width, 50 μm in length, and 47 nm in height as fabricated on a SiO_2/Si surface by electron-beam lithography.

An SECM image of a 100 nm-wide Au nanoband was obtained by scanning a 2.2 μm-diameter Pt disk probe with RG = 10 at a constant height (Figure 6-8a). The tip current based on $Ru(NH_3)_6^{3+}$ reduction increased above the nanoband during the lateral probe scan. This result indicates that $Ru(NH_3)_6^{2+}$ generated at the tip was oxidized at the nanoband surface to regenerate $Ru(NH_3)_6^{3+}$, which enhanced the tip current. The feedback effect is substantial although only 5.8

% of the substrate surface directly under the tip is covered with the nanoband. The nanoband appears much wider than 100 nm in the image, where a spatial resolution is determined by the tip size. The spatial resolution is high enough to confirm a band length of 50 μm in the image. The variation of the tip current above the nanoband along the *x*-axis is partially due to heterogeneous reactivity or morphology of the nanoband surface. The band height varies with ±4 nm at the center as observed by AFM. More importantly, representative cross sections of the image at *x* = 12, 30, and 48 μm (Figure 6-8b) demonstrate that the variation of the tip current is much smaller above the nanoband than above the surrounding SiO_2 surface. The gradual decrease of the tip current above the SiO_2 surface along the *x*-axis corresponds to the decrease of the tip–substrate distance caused by the tilt of the substrate surface. The substrate tilt results in a sharper peak current in the *y*-direction, because the tip feedback current depends on the distance more weakly above the nanoband than above the insulating surface (see 6.4.2).

(a)

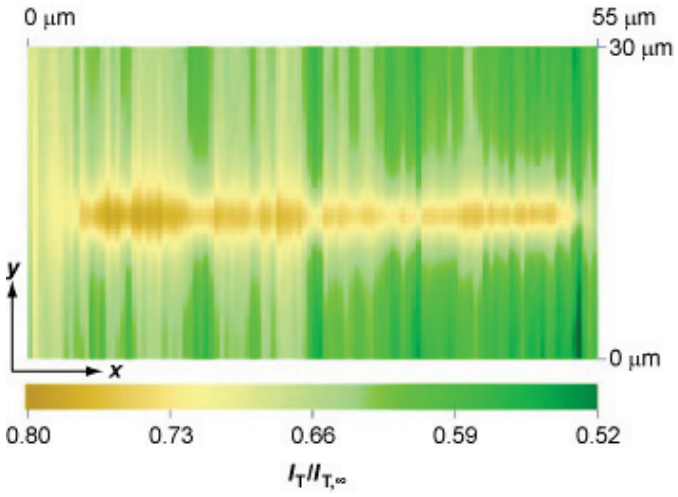

(b)

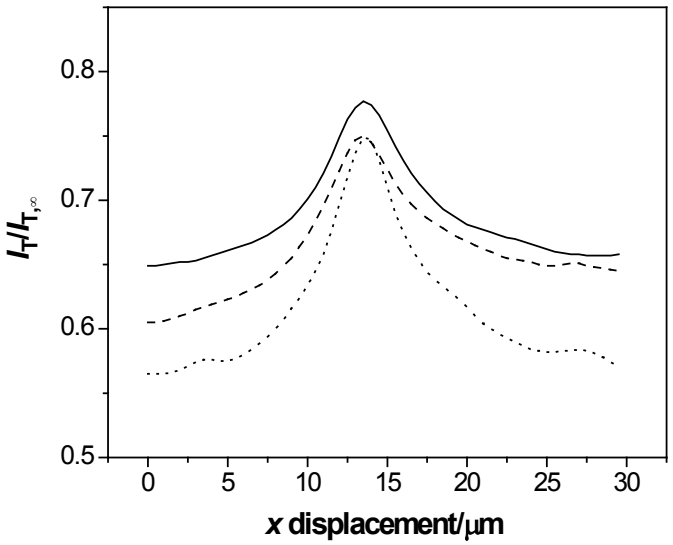

Figure 6-8. (a) An SECM image of a 100 nm-wide Au band as obtained using a 2.2 μm-diameter disk Pt probe with RG = 10 at a constant height. The scan rate was 15 μm/s. The nanoband was immersed in 0.1 M KCl containing 1 mM $Ru(NH_3)_6Cl_3$. (b) SECM line scans at x = 12, 30, and 48 μm in the image (solid, dashed, and dotted lines, respectively).

6.4.2. Approach curve measurement with a 100 nm-wide band

A small feedback effect above the nanoband in the SECM image indicates that the 50 μm-long nanoband, which is 18 times longer than the tip diameter, is not long enough to drive $Ru(NH_3)_6^{3+}$ regeneration at the band surface to a diffusion limitation. The kinetic limitation is quantitatively demonstrated by studying current approach curves, where the tip current, i_T, was measured as a function of the tip–substrate distance, d. An approach curve at a 100 nm-wide band as measured with a 2.8 μm-diameter Pt disk probe with RG = 10 was plotted in the normalized form for

numerical analysis (solid line in Figure 6-9). The tip current decreased monotonically as the tip center was brought vertically toward the band center. The approach curve at the nanoband, however, is less negative than that at the insulating SiO_2 surface (dotted line), confirming mediator regeneration at the nanoband surface. The approach curve at the nanoband is more negative than the curves simulated for diffusion-limited or reversible mediator regeneration at the nanoband with 47 nm in height. This result indicates that the mediator regeneration is kinetically limited at the nanoband. In fact, the experimental approach curve at the nanoband fits well with the quasi-reversible approach curve simulated for the raised nanoband with $K = 3.5$ and $\alpha = 0.5$. The theoretical curve strongly depends on K but not on α, because the overpotential for the mediator regeneration at the nanoband, $E - E^{0'}$, is small during the tip approach (the inset of Figure 6-9) [20]. A larger K value of 17 as obtained by assuming an inlaid nanoband in the simulation is overestimated. This result confirms a significant effect of band height on the tip feedback current for a quasi-reversible substrate reaction.

It should be noted that electronic conduction in the unbiased Au nanoband is not the rate-determining step in the SECM feedback process although the lateral electron transport through the nanoband is required for coupling mediator regeneration at the nanoband surface under the tip with mediator electrolysis at the exterior surface (Figure 6-1). On one hand, Au nanobands are more resistive than bulk Au materials because of a smaller cross-section area (100 or 500 nm × 47 nm for nanobands in this study) and a higher resistivity (6–30 μΩ·cm for Au nanobands with similar nanoscale dimensions and ~2 μΩ·cm for bulk Au materials [33, 34]). On the other hand, current that flows laterally through a nanoband is small in the SECM experiments and is equivalent to the difference of currents at a tip above the nanoband and insulating surfaces [16]. Overall, a flow of sub-nA current along the 50 μm-long Au nanobands with a ~kΩ resistance

results in only a ~μV potential drop. This result justifies a uniform open circuit potential of a nanoband as assumed in our model to obtain theoretical approach curves that fit very well with experimental curves. Moreover, a normalized approach curve with a 100 nm-wide Au band was identical at 1 and 2 mM mediator concentrations (data not shown), where the current flow through the nanoband varies. The concentration-independent feedback effect confirms a negligibly small potential drop in the conductive substrate [35].

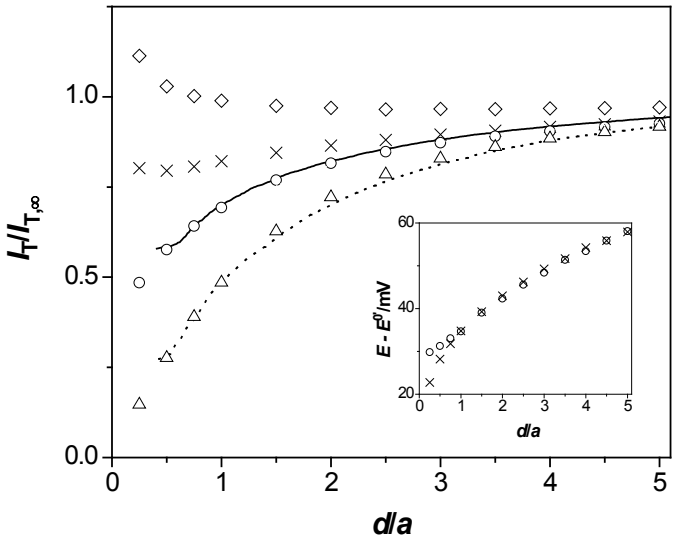

Figure 6-9. Normalized approach curves at a 100 nm-wide Au band (solid line) and a SiO_2 surface (dotted line) as obtained using a 2.8 μm-diameter disk Pt probe with RG = 10 in 0.1 M KCl containing 1 mM $Ru(NH_3)_6Cl_3$. The scan rate was 0.75 μm/s. The symbols represent the curves simulated for quasi-reversible (circles; K = 3.5), reversible (crosses) and diffusion-limited (diamonds) ET at a raised nanoband with $w/2a$ = 0.036, $h/2a$ = 0.017, and $l/2a$ = 18. The triangles represent a purely negative

approach curve at an insulating surface. The inset show corresponding potential approach curves for the quasi-reversible (circles) and reversible (crosses) cases.

6.4.3. Approach curve measurement with a 500 nm-wide band

A 50 μm-long band with 500 nm in width and 47 nm in height was also studied to assess effects of the band width and height on the tip feedback current. An approach curve with the 500 nm-wide band (solid line in Figure 6-10) is more positive than that with the 100 nm-wide band. Moreover, the tip current with the 500 nm-wide band depends more weakly on the band height. A K value of 3.5 is obtained from a good fit with an approach curve simulated with 47 nm in height while a K value of 6 was obtained with an assumption of an inlaid nanoband in the simulation. On the other hand, a change of the height of the 100 nm-wide band from 47 to 0 nm in simulations changed K from 3.5 to 17, indicating that the neglect of the band height causes more significant overestimation of the K value at the narrower nanoband.

The K value of 3.5 as obtained with the 100 and 500-nm wide raised nanobands correspond to k^0 = 0.19 cm/s in eq 4 with the given tip radii and a diffusion coefficient of 7.5×10^{-6} cm^2/s for $Ru(NH_3)_6^{3+}$ in the aqueous electrolyte solutions. These k^0 values are significantly smaller than those of the same redox couple at Au electrodes in 0.1 M $HClO_4$ (1.43 cm/s [36]), 1.0 M KF (1.0 cm/s [37, 38] and 1.7 cm/s [39]), and 1 M H_2SO_4 (0.85–5.5 cm/s [40]). The smaller k^0 values are not due to a double layer effect based on strong adsorption of Cl^- on the Au surface [41] because a similar k^0 value was obtained by using weakly adsorbing ClO_4^- as an electrolyte, i.e., in 0.05 M $KClO_4$ containing 1 mM $Ru(NH_3)_6(ClO_4)_3$ (data not shown). We ascribe the smaller k^0 values to the passivation of the Au nanoband surface with Cr oxide, which is formed at the surface by

rapid diffusion of Cr from the adhesion layer through the thin Au layer [23, 24]. The passive Cr oxide slows down the kinetics of $Ru(NH_3)_6^{3+/2+}$ couple as observed with oxide-covered Cr electrodes, where k^0 decreases from 0.36 to 0.00025 cm/s in 1 M H_2SO_4 as the thickness of the oxide layer increases from 0.5 to 2 nm [40].

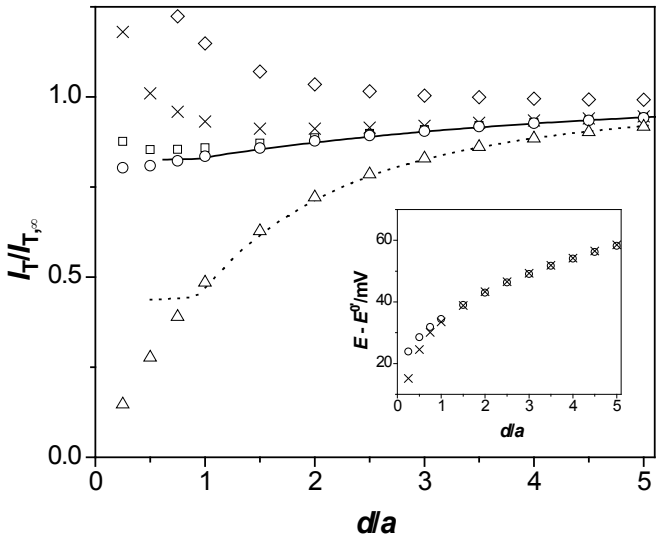

Figure 6-10. Normalized approach curves at a 500 nm-wide Au band (solid line) and a SiO_2 surface (dotted line) as obtained using a 2.8 μm-diameter disk Pt probe with RG = 10 in 0.1 M KCl containing 1 mM $Ru(NH_3)_6Cl_3$. The scan rate was 0.75 μm/s. The symbols represent the simulated curves as defined in the caption of Figure 9 at a raised nanoband with $w/2a$ = 0.18, $h/2a$ = 0.017, and $l/2a$ = 18, or the insulating surface. The circles represent a quasi-reversible response with K = 3.5.

6.5. Conclusions

This work extends the applicability of SECM to electrochemical characterization of 1D nanostructures with finite dimensions. Moreover, SECM measurements under unbiased conditions eliminate the integration of the nanostructures into the electrode format by the multiple lithographic processes, which is required for conventional voltammetric characterization [13, 42]. At the same time, finite ET kinetics at an unbiased 1D nanostructure with finite dimensions compromises the tip feedback current in comparison to a diffusion-limited or a reversible case, thereby requiring a probe that is much smaller than the largest dimension of a 1D nanostructure.

High sensitivity of SECM to dimensions of 1D nanostructures was demonstrated both theoretically and experimentally. A good agreement between simulated and experimental approach curves confirms the well-defined dimensions of the nanobands as fabricated by electron-beam lithography. With the knowledge of the dimensions, the redox activity of individual 1D nanostructures was probed by SECM, thereby revealing rather slow ET kinetics for $Ru(NH_3)_6^{3+/2+}$ couple at the Au nanobands with a Cr adhesion layer.

6.6 Supporting information

6.6.1 COMSOL Multiphysics Simulation. The SECM diffusion problem defined above was solved in a dimensionless form, where dimensionless parameters are defined by:

$$X = x/a \tag{13}$$

$$Y = y/a \tag{14}$$

$$Z = z/a \tag{15}$$

$$L = d/a \tag{16}$$

$$W = w/2a \tag{17}$$

$$H = h/2a \tag{18}$$

$$LL = l/2a \tag{19}$$

$$C(X,Y,Z) = c(x,y,z)/c_0 \tag{20}$$

The steady-state diffusion of O in the solution phase can be expressed in the dimensionless form as

$$\frac{\partial^2 C(X,Y,Z)}{\partial X^2} + \frac{\partial^2 C(X,Y,Z)}{\partial Y^2} + \frac{\partial^2 C(X,Y,Z)}{\partial Z^2} = 0 \tag{21}$$

The boundary conditions on the nanoband surface are given using the dimensionless parameters as

diffusion limitation

$$C(X, Y, L) = 1 \qquad |X| \le LL,\ \mathrm{Y} \le W \tag{22}$$

reversible

$$E = E^{0'} - \frac{RT}{nF}\ln\frac{1 - C(X,Y,L)}{C(X,Y,L)} \qquad |X| \le LL,\ \mathrm{Y} \le W \tag{23}$$

quasi-reversible

$$\left[\frac{\partial C(X,Y,Z)}{\partial Z}\right]_{Z=L} = \frac{K(1+\theta)}{\theta^{\alpha}}\left[\frac{\theta}{\theta+1} - C(X,Y,L)\right]$$

$$|X| \le LL,\ \mathrm{Y} \le W \tag{24}$$

with

$$\theta = \exp\left[\frac{F}{RT}(E - E^{0'})\right] \tag{25}$$

Eq 24 is equivalent to the expression of the flux boundary condition in COMSOL Multiphysics.

Other boundary conditions are:

insulation region around the band electrode

$$\left[\frac{\partial C(X,Y,Z)}{\partial Z}\right]_{Z=L} = 0 \qquad LL < |X| \text{ or } W < Y,\ X^2 + Y^2 < 50^2 \tag{26}$$

disk probe surface

$$C(X, Y, 0) = 0 \qquad X^2 + Y^2 \leq 1 \tag{27}$$

insulation region around the disk electrode

$$\left[\frac{\partial C(X,Y,Z)}{\partial Z}\right]_{Z=0} = 0 \qquad 1 < X^2 + Y^2 < \mathrm{RG}^2 \tag{28}$$

insulation region at the side of the disk electrode

$$\left[\frac{\partial C(X,Y,Z)}{\partial N}\right] = 0 \qquad X^2 + Y^2 = \mathrm{RG}^2,\ -20 \leq Z \leq 0 \tag{29}$$

where N is the surface normal.

simulation space limits

$$C(X, Y, Z) = 1 \qquad X^2 + Y^2 = 50^2,\ -20 \leq Z \leq L \tag{30}$$

$$C(X, Y, Z) = 1 \qquad \mathrm{RG}^2 \leq X^2 + Y^2 \leq 50^2,\ Z = -20 \tag{31}$$

Attached is the example of a simulation for a reversible line scan above a raised band with W = 0.015, H = 0.017, and LL = 50 at L = 1.

ACKNOWLEDGEMENTS

This work was supported by grants from the National Institutes of Health (GM073439), and the Petersen Institute of NanoScience and Engineering (PINSE) at the University of Pittsburgh. H. X. thanks for an Andrew Mellon Predoctoral Fellowship from the University of Pittsburgh. The authors thank the Department of Materials Science and Engineering for the provision of access to the SEM instrumentation, the NanoScale Fabrication and Characterization Facility of the PINSE for focused ion beam milling, the Penn State Nanofabrication Facility, a member of the NSF's National Nanotechnology Infrastructure Network, for electron-beam lithography. The authors also thank Patrick J. Rodgers for careful reading of this manuscript.

References

(1) Y. Xia, P. Yang, Y. Sun, Y. Wu, B. Mayers, B. Gates, Y. Yin, F. Kim, and H. Yan, Adv. Mater. 15 (2003) 353–389.

(2) S. Iijima, Nature 354 (1991) 56–58.

(3) T. R. Kline, M. L. Tian, J. G. Wang, A. Sen, M. W. H. Chan, and T. E. Mallouk, Inorg. Chem. 45 (2006) 7555–7565.

(4) S. J. Hurst, E. K. Payne, L. D. Qin, and C. A. Mirkin, Angew. Chem., Int. Ed. 45 (2006) 2672–2692.

(5) R. W. Murray, Chem. Rev. 108 (2008) 2688–2720.

(6) P. Delahay, in New Instrumental Methods in Electrochemistry, Interscience, New York, 1954, p. 67–70

(7) M. R. Deakin, R. M. Wightman, and C. A. Amatore, J. Electoanal. Chem. 215 (1986) 49–61.

(8) C. A. Amatore, B. Fosset, M. R. Deakin, and R. M. Wightman, J. Electroanal. Chem. 225 (1987) 33–48.

(9) C. Amatore, C. Combellas, F. Kanoufi, C. Sella, A. Thiebault, and L. Thouin, Chem. Eur. J. 6 (2000) 820–835.

(10) K. R. Wehmeyer, M. R. Deakin, and R. M. Wightman, Anal. Chem. 57 (1985) 1913–1916.

(11) P. Bertoncello, J. P. Edgeworth, J. V. Macpherson, and P. R. Unwin, J. Am. Chem. Soc. 129 (2007) 10982–10983.

(12) R. B. Morris, D. J. Franta, and H. S. White, J. Phys. Chem. 91 (1987) 3559–3564.

(13) I. Heller, J. Kong, H. A. Heering, K. A. Williams, S. G. Lemay, and C. Dekker, Nano Lett. 5 (2005) 137–142.

(14) E. P. M. Leiva, C. G. Sanchez, P. Velez, and W. Schmickler, Phys. Rev. B 74 (2006) 035422.

(15) I. Heller, J. Kong, K. A. Williams, C. Dekker, and S. G. Lemay, J. Am. Chem. Soc. 128 (2006) 7353–7359.

(16) H. Xiong, D. A. Gross, J. Guo, and S. Amemiya, Anal. Chem. 78 (2006) 1946–1957.

(17) A. J. Bard and M. V. Mirkin (Eds.), Scanning Electrochemical Microscopy, Marcel Dekker, New York, 2001.

(18) S. Amemiya, A. J. Bard, F.-R. F. Fan, M. V. Mirkin, and P. R. Unwin, Ann. Rev. Anal. Chem. 1 (2008) 95–131.

(19) P. Sun and M. V. Mirkin, Anal. Chem. 78 (2006) 6526–6534.

(20) H. Xiong, J. Guo, and S. Amemiya, Anal. Chem. 79 (2007) 2735–2744.

(21) D. O. Wipf and A. J. Bard, J. Electrochem. Soc. 138 (1991) 469–474.

(22) Y. Selzer, I. Turyan, and D. Mandler, J. Phys. Chem. B 103 (1999) 1509–1517.

(23) P. H. Holloway, Gold Bull. 12 (1979) 99–106.

(24) C. A. Goss, D. H. Charych, and M. Majda, Anal. Chem. 63 (1991) 85–88.

(25) Y. Shao and M. V. Mirkin, J. Phys. Chem. B 102 (1998) 9915–9921.

(26) C. G. Zoski and M. V. Mirkin, Anal. Chem. 74 (2002) 1986–1992.

(27) A. J. Bard, M. V. Mirkin, P. R. Unwin, and D. O. Wipf, J. Phys. Chem. 96 (1992) 1861–1868.

(28) A. J. Bard and L. R. Faulkner, Electrochemical Methods: Fundamentals and Applications, John Wiley & Sons, New York, 2001, p. 94–96.

(29) M. V. Mirkin and A. J. Bard, Anal. Chem. 64 (1992) 2293–2302.

(30) J. Kwak and A. J. Bard, Anal. Chem. 61 (1989) 1221–1227.

(31) S. Amemiya and A. J. Bard, Anal. Chem. 72 (2000) 4940–4948.

(32) J. F. Zhou and D. O. Wipf, J. Electroanal. Chem. 499 (2001) 121–128.

(33) Y. J. Chen, J. H. Hsu, and H. N. Lin, Nanotechnology 16 (2005) 1112–1115.

(34) E. J. Menke, M. A. Thompson, C. Xiang, L. C. Yang, and R. M. Penner, Nat. Mater. 5 (2006) 914–919.

(35) N. R. Wilson, M. Guille, I. Dumitrescu, V. R. Fernandez, N. C. Rudd, C. G. Williams, P. R. Unwin, and J. V. Macpherson, Anal. Chem. 78 (2006) 7006–7015.

(36) M. Muzikar and W. R. Fawcett, Anal. Chem. 76 (2004) 3607–3611.

(37) T. Iwashita, W. Schmickler, and J. W. Schultze, Ber. Bunsenges. Phys. Chem. 89 (1985) 138–142.

(38) W. Schmickler, Interfacial Electrochemistry, Oxford University Press, Oxford, 1996.

(39) J. F. Smalley, L. Geng, A. Chen, S. W. Feldberg, N. S. Lewis, and G. Cali, J. Electroanal. Chem. 549 (2003) 13–24.

(40) T. P. Moffat, H. Yang, F.-R. F. Fan, and A. J. Bard, J. Electrochem. Soc. 139 (1992) 3158–3167.

(41) R. I. Tusseri and D. Posadas, J. Electroanal. Chem. 191 (1985) 387–399.

(42) B. M. Quinn and S. G. Lemay, Adv. Mater. 18 (2006) 855–859.

(43) Beriet, C.; Pletcher, D. *J. Electroanal. Chem.* **1994**, *375*, 213–218.

(44) Birkin, P. R.; Silva-Martinez, S. *Anal. Chem.* **1997**, *69*, 2055–2062.

(45) Gennett, T.; Weaver, M. J. *Anal. Chem.* **1984**, *56*, 1444–1448.

(46) Wipf, D. O.; Kristensen, E. W.; Deakin, M. R.; Wightman, R. M. *Anal. Chem.* **1988**, *60*, 306–310.